THE INFLUENCE OF UNSTEADY STREAKS ON THE STABILITY OF FLAT PLATE BOUNDARY LAYERS

Nicholas James Vaughan

Thermo-Fluids group

Department of Mechanical Engineering

Imperial College London, UK

Submitted in partial fulfilment of the requirements for the degree of Doctor of Philosophy

Department of Mechanical Engineering, Imperial College London

September 2010

Abstract

The natural mechanism for transition to turbulence in flat-plate boundary layers is the growth and breakdown of Tollmien-Schlichting (TS) waves. In the presence of significant free-stream turbulence (FST) however, streamwise velocity perturbations, known as Klebanoff modes or streaks, amplify inside the boundary layer. These distortions alter the stability characteristics of the boundary layer, and the natural mechanism is bypassed, leading to earlier transition.

Herein, a model is employed to describe the Klebanoff distortions: one Fourier component of the FST is used along with its signature inside the shear region to force the boundary layer and stimulate streaks. Varying the parameters of the forcing mode causes streaks with different frequencies and amplitudes. A base flow which is periodic in two dimensions is formed, and its linear stability is investigated using Floquet theory. Two modes emerge as the most unstable, and their eigenvalues are tracked whilst varying streak frequency and amplitude. The 'inner' mode, is related to the TS wave, but its growth rate is enhanced by unsteady streaks. The 'outer' mode is a high-frequency instability of the streaks at the edge of the boundary layer. It has no counterpart in the undisturbed boundary-layer. The critical streak amplitude for the outer mode is calculated for different streak frequencies and it agrees more closely with experiments than previous analyses which assumed the streaks to be steady. The current analysis indicates that increasing the frequency of the streaks can enhance their instability. In fact an optimum frequency exists for free-stream disturbances to penetrate the shear and stimulate unstable streaks.

Direct numerical simulations with streaks and secondary-instability eigenmodes are conducted. The simulations show that both the inner and outer mode can grow to nonlinear amplitudes and cause boundary-layer transition to turbulence.

Acknowledgements

The author draws attention to the enormous debt of gratitude he owes to Dr. T. A. Zaki who was the academic supervisor. His commitment and tireless support throughout this research were more than could possibly have been expected. Also, the author wishes to thank his colleagues in room 503 and the rest of the thermofluids group for an exciting and rewarding period at Imperial College. A special mention goes to Sandeep Saha with whom the author is lucky to have held so many enjoyable and inspiring discussions.

Many thanks go to the author's friends and family, for their support and patience. Special gratitude is paid to I. D. for her love and encouragement.

Financial support from the EPSRC in the form of a Doctoral Training Account award from the Mechanical Engineering Department at Imperial College is kindly acknowledged.

Declaration

I, Nicholas James Vaughan, declare that the work contained within this thesis is original and my own, except from that which is appropriately credited to others. Specifically that includes the algorithm for linear initial value problem, and assistance which I received in respect of the direct numerical simulations.

Contents

List of Tables

List of Figures

Chapter 1

Introduction

The transition from laminar to turbulent flow in boundary layers has interesting fundamental aspects and important consequences in practice. The streamlines of a laminar flat-plate boundary layer are smooth, and almost parallel, but in turbulent boundary layers, randomly occurring eddies stir up the flow and act to mix scalar quantities and momentum. This change in behaviour is of concern for engineers, for example the low skin friction coefficient of laminar boundary layers is appealing for aircraft designers concerned with drag, but for dissipating heat from the avionics systems on board, a turbulent state is preferable. Boundary layers in noisy free-stream environments are of particular interest. For instance, turbulent boundary layer flow on turbine blades causes an increase in skin friction but helps to avoid separation, and the transition process is affected by turbulence in the free stream.

Transition inside the boundary layer begins far upstream of the pronounced phenomena associated with the final breakdown to turbulence, and progress in hydrodynamic stability theory over the last century or so has shed light on the various physical processes involved. Transitional flows have also been studied with direct numerical simulations (DNS) in sufficient detail to extract information unobtainable from experiments. However, only relatively canonical problems are possible so far, and the high-fidelity calculations are too

computationally expensive to be used routinely as a design tool. Theory therefore has an important role in the understanding of inherent mechanisms in transition which is vital to predict or control the onset of turbulence.

In any transitional flow, a variety of processes link the laminar state to the fully developed turbulent flow. Also, for a given basic flow, the transition scenario can depend strongly on small differences in the particular conditions. For example, the critical Reynolds number at which the flow in pipes becomes turbulent lies in the range 2,000–100,000 (Durst & Ünsal, 2006), depending on how smooth the inlet is as well as other factors including perturbations in the inlet flow and wall roughness. In the case of boundary layers, different mechanisms lead to breakdown depending on the level of free-stream perturbations, and this is the topic of the present thesis.

1.1 Transition in conditions of low environmental disturbance

Transition to turbulence in boundary layer flows is generally divided into two categories based on the role played by exponential instabilities of the two-dimensional boundary layer, Tollmien-Schlichting (TS) waves. When the level of external disturbances is small, these instabilities are a vital part of the 'natural' transition process, but when environmental perturbations are significant, this natural route to transition is 'bypassed' by other mechanisms (Morkovin, 1969; Kachanov, 1994).

During the early stages of natural transition, infinitesimal broadband external disturbances are transferred into boundary layer oscillations. This process is known as receptivity, a term coined by Morkovin (1969). The TS waves are eigen-solutions of the linear stability operator for the base flow, and receptivity sets their initial amplitude (Saric, 1998). For incompressible flows, receptivity can occur in a variety of ways (Saric *et al.*, 2002): These

can include the interaction of free-stream turbulence or sound with the leading edge, surface roughness, or discontinuities in the surface curvature. What these mechanisms have in common is their facility to take a free-stream disturbance with some wavenumber, and broaden its spectrum so that it includes the wavenumber of the natural instability mode. In conditions where free-stream turbulence (FST) has low intensity, the dominant source of disturbance is irrotational acoustic perturbations (Mack, 1977), which have been shown to contribute to nascent TS waves (Kosorygin & Saric, 1995). The initial evolution of these disturbances is described by linear stability theory. The Orr-Sommerfeld–Squire eigenvalue problem governs the stability of linear viscous perturbations to a parallel two-dimensional basic flow, and is used to calculate the critical Reynolds number, R_{crit}, beyond which the most unstable mode begins to amplify exponentially.

Early work by Tollmien (1929) on two-dimensional travelling waves and the calculation of their growth rates by Schlichting in 1933 identified the so-called Tollmien-Schlichting wave which becomes unstable at $R_{crit} = 302$ in terms of the free stream velocity and the Blasius length scale. Much of the following work focused on two-dimensional waves, not least because of Squire's transformation which shows that for any unstable three-dimensional wave, there is an unstable two-dimensional wave at a lower Reynolds number.

More than a decade after the first theoretical work, Schubauer & Skramstad (1947) were the first to experimentally observe TS waves, by forcing the boundary layer with an oscillating ribbon, and a wealth of experimental work followed (for example Ross *et al.*, 1970; Strazisar *et al.*, 1977; Kozlov & Babenko, 1978). Theoretically, Lin (1955) showed that adverse pressure gradients destabilise the flow and favourable pressure gradients have the converse effect. Gaster (1962) showed that quantitative calculations of the growth rate from temporal stability calculations could be improved by considering spatially growing modes.

However, the neutral curve which describes the region of instability in the Reynolds number-frequency plane does not depend on the choice of spatial or temporal growth concepts. If the nonparallelism of the boundary layer flow is accounted for, the unstable area expands slightly and agrees more closely with experimental data (Gaster, 1974; Herbert, 1997).

When the TS waves grow to a sufficient amplitude, typically around 1% of the free-stream velocity, small three-dimensional disturbances naturally present are amplified and spanwise rows of Λ-vortices appear (Herbert, 1988). Klebanoff *et al.* (1962) recognised the three-dimensional nature of the later stages of orderly transition but attributed it to spanwise differential amplification of the TS waves. Using smoke visualisation, Knapp & Roache (1968) clearly identified that streamwise periodic rows of Λ-vortices with a spanwise spacing similar to the TS wavelength appeared in two possible arrangements. The Λ-vortices could amplify behind one-another, aligned at the same spanwise location, or in a spanwise staggered pattern. The growth of Λ-vortices is due to the secondary instability of the finite amplitude TS waves (Maseev, 1968; Herbert & Morkovin, 1980). The aligned pattern (also known as K-transition after Klebanoff) has the same streamwise wavelength as the TS wave, λ_x, which is explained by a fundamental secondary instability. The subharmonic instability is manifested in the staggered pattern with a wavelength of $2\lambda_x$ which can be associated with C- and H- types of transition, named after Craik (1971) and Herbert (1983), respectively.

After the slow growth of TS waves on a viscous time scale, the secondary instability stage occupies only around five TS wavelengths before final breakdown begins. Non-linear distortions of the flow-field lead to confined high-shear layers associated with inflectional profiles. Localised turbulent spots, first observed by Emmons (1951) form, grow and merge into fully turbulent flow over roughly one TS wavelength. A direct numerical simulation (DNS)

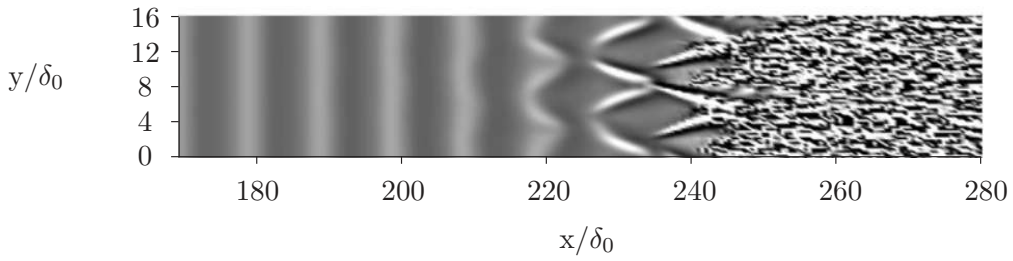

Figure 1.1: Contours of $v-$perturbation showing TS waves, subharmonic secondary instability, Λ-structures and natural transition. The inlet plane is at $R = 400$ in terms of the Blasius length scale. In the figure, lengths are nondimensionalised by the 99% thickness at the inlet, δ_0. The figure is adapted from simulation by Zaki *et al.* (2010).

of natural transition is presented in figure 1.1. The inlet condition consisted of the Blasius flow, a TS wave with amplitude 1%, and very low amplitude background disturbances $Tu \sim 0.1\%$. After streamwise amplification of the TS waves, the random perturbations triggered subharmonic secondary instability, and a staggered array of Λ-vortices can be observed upstream of the breakdown to turbulence.

Generally, in conditions of very low background turbulence, the natural transition process is completed around $R = 5,000$ in terms of the Blasius length scale. However when the FST is significant the transition process can be modified slightly or take an entirely different route.

1.2 Boundary layer streaks and their effect on transition

In the presence of FST the laminar boundary layer develops low-frequency, high-amplitude perturbations of streamwise velocity which are not associated with the TS instability. They resemble streamwise oriented jets in the perturbation field, and their spanwise spacing is on the order of the boundary layer thickness. Commonly known as boundary layer streaks, they are sometimes called 'Klebanoff modes' after the early experiments on boundary layers

perturbed with grid-generated turbulence by Klebanoff (1971).

Arnal & Juillen (1978) gave the first detailed account of the downstream growth of streamwise velocity fluctuations, u_{rms}, in a boundary layer subject to FST. When the turbulence level was $Tu = 1.1\%$ in the free stream , u_{rms} normalised by the free-stream velocity, U_∞, reached 7% inside the boundary layer at $R = 870$, which was the Reynolds number for the onset of transition. They found most of the perturbation energy half way through the boundary layer thickness, unlike the TS wave which is located close to the wall. Kendall (1985) carried out measurements of boundary layers disturbed by FST and found the velocity fluctuations to grow in the streamwise direction proportional to $x^{1/2}$. Westin *et al.* (1994) experimentally studied the development of streaks and showed that the mean-flow profile was altered by $\sim$ 1% despite streak perturbations of $u_{rms} = 7\%$. Their experiments confirmed that u_{rms} increases with $x^{1/2}$, and other references therein corroborated this as a general observation. Matsubara & Alfredsson (2001) described the similarity properties of streaks stimulated by FST as they evolved downstream. When normalised by the local displacement thickness, the wall-normal profile of the streak velocity fluctuations become independent of streamwise location. Matsubara & Alfredsson (2001) also studied the energy spectra of disturbances inside the boundary layer and found that long-streamwise-wavelength disturbances dominate, and the spanwise scale approaches the boundary layer δ_{99} thickness downstream from the leading edge. The description of streaks in the literature is thus fairly extensive and, in addition, a lot of theoretical work has been aimed at explaining the phenomenon.

The disproportionately large near-wall response to free-stream forcing is due to the mean boundary-layer shear. Rapid distortion theory (RDT) explains how the energy in a sheared broadband disturbance is amplified algebraically. For instance Moffatt (1967)

showed that the inviscid solution for a linear velocity profile tends to $u_{rms} \propto t^{1/2}$ for large times, and that low streamwise wavenumber components dominate. Phillips (1969) suggested a simple physical explanation: cross-stream velocity components displace mean momentum, for example low-velocity fluid from near the wall is lifted to cause a low-speed streak. In terms of vorticity, normal velocity perturbations tilt the mean spanwise vorticity into wall-normal vorticity, manifested as streaks.

Another perspective on the generation of streaks is non-modal stability theory (Trefethen *et al.*, 1993). In a mathematical sense, the theory states that an initial disturbance described as a superposition of decaying eigen-solutions can grow transiently because the linear stability operator is non-normal. The eigenmodes of a non-normal operator are not orthogonal. Therefore a solution consisting of a superposition of eiegenmodes has the possibility to grow, even if the modes individually decay.

The two-dimensional Orr-Sommerfeld operator itself is non-normal, but the main source of non-normality is the coupling term between the normal velocity and vorticity. By means of this coupling, normal velocity forces the vorticity, and this hints at the physical mechanism of 'lift up'. Along these lines, a large body of research has sought to identify the optimum conditions which lead to the maximum growth of energy at a particular downstream location (Butler & Farrell, 1992; Andersson *et al.*, 1999; Luchini, 2000). The energy in so-called 'optimal' perturbations can amplify significantly even below R_{crit}. Streamwise oriented vortices located inside the boundary layer undergo the maximum growth, which is consistent with RDT in so far as they have a low streamwise wavenumber. The optimal growth studies have identified a spanwise scale which is similar to that seen in experiments, but a link between naturally-occurring free-stream turbulence and the specially calculated optimal initial conditions *inside* the boundary layer is not clear.

This raises the central question of how free-stream disturbances enter the boundary layer. In fact, simple inviscid analyses in the context of RDT (Hunt & Carruthers, 1990) and linear stability theory (Jacobs & Durbin, 1998) indicate that vortical disturbances in the free-stream are completely excluded from the boundary layer. This phenomenon, known as 'shear sheltering' (Hunt & Durbin, 1999) has been studied in the viscous case, where limited penetration is possible (Jacobs & Durbin, 1998), using the continuous spectra of the Orr-Sommerfeld and Squire equations. Continuous modes encapsulate particular free-stream Fourier modes and their effect inside the boundary layer (Grosch & Salwen, 1978), thus they address the question of local boundary layer receptivity to free-stream vorticity.

Numerical and theoretical studies of boundary layer transition have used continuous modes as a model for the FST and successfully reproduced the details of streaky boundary layers from experiments. For example, Jacobs & Durbin (2001) simulated a boundary layer perturbed by FST. They used a synthetic broadband turbulent spectrum constructed from a superposition of continuous Orr-Sommerfeld modes as an inlet condition. The turbulence level was set to 3.5%, and streaks amplified up to nearly $u_{rms} = 10\%$ before transition completed around $R_x = 3 \times 10^5$, which is consistent with the experiments of Roach & Brierley (1992). The energy spectrum inside the boundary layer illustrated the shear filtering effect: high-frequency components were selectively filtered out, but low-frequency disturbances penetrated into the boundary layer. Shear filtering offers another reason for the long wavelength of streaks. Inviscid RDT indicated that these perturbations undergo the maximum amplification, but studying continuous modes shows that low-frequency free-stream perturbations are the most capable of penetrating into the boundary layer.

The shear-filtering phenomenon and its consequences have been highlighted by studying individual continuous modes (Jacobs & Durbin, 1998; Zaki & Durbin, 2005; Zaki & Saha,

2009). For example, Zaki & Durbin (2005) solved the initial value problem for the normal vorticity response to forcing by an Orr-Sommerfeld mode. The solution illustrated the transient growth of streaks inside the boundary layer, and showed that one normal-velocity mode was sufficient to cause a high-amplitude response, but only if the frequency were low.

The experimental and numerical investigations on boundary layers perturbed by FST have broadly succeeded in characterising the Klebanoff distortions. Theoretical research has examined the boundary layer receptivity to FST and explained the generation of streaks. Given their high amplitude, it seems inevitable that the impact of boundary layer streaks on transition is significant, but their precise role poses a great deal of questions, some of which remain unanswered.

1.2.1 The effect of streaks on natural transition

Free-stream turbulence is capable of stimulating two types of fluctuation inside the boundary layer: TS waves, which become exponentially unstable for a particular range of Reynolds numbers; and streaks which grow algebraically from the leading edge. It has been established that TS waves play a role in transition up to FST levels of 0.5–1.0% (Grek *et al.*, 1990; Boiko *et al.*, 1994). However, the relative importance of discrete instabilities, streaks, and possible interactions are the subject of ongoing research. For example, experiments have shown that increasing the amplitude of vortical disturbances in the free stream increases the u_{rms} associated with the streaks (see for example the comparisons made in Westin *et al.*, 1994), and the TS waves become hard to detect in the highly distorted boundary layer. However, recent work by Liu *et al.* (2008*a*) demonstrates that streaks can excite the fundamental secondary instability of the TS waves, depending on the spanwise wavelength of the streaks. The effect of FST on natural transition is likely to depend on the amplitude

of the turbulence and receptivity mechanisms for the TS waves, but a central question is whether streaks enhance or diminish the growth rate of the *primary* TS instability wave.

Experiments on boundary layers beneath turbulent free streams along with numerical and theoretical studies have shown that streaks have an impact on the TS waves. However the outcome appears to depend on assumptions made about the TS instability and the streaky boundary layer environment. Whether naturally occurring unsteady streaks have a stabilising or destabilising effect on TS waves remains a matter of intrigue.

Experiments by Grek *et al.* (1990) on the flow over a wing section showed that TS waves could be generated and detected at a moderately high free-stream turbulence level of 1.75%. They stimulated the TS wave by means of a vibrating ribbon and measured the downstream evolution of velocity disturbances with hot-wire anemometry. Separate cases with and without FST were run, and in the presence of FST, streaks with an amplitude of 6% were reported. Along the part of the chord with favourable pressure gradient (FPG) the TS waves decayed irrespective of the turbulence level, but further downstream in the adverse pressure gradient (APG) section, the TS waves grew more quickly in the absence of free-stream turbulence. Boiko *et al.* (1994) conducted similar experiments with an FST level of 1.5% on flat-plate boundary layers and also found that TS-waves had a lower amplification rate than in the case of an undisturbed Blasius boundary layer. It should be noted however that the forcing mechanism used in these experiments stems from two-dimensional Orr-Sommerfeld theory which ignores possible alterations that could affect the TS instability in the highly perturbed three-dimensional boundary layer. For example the forcing used by Boiko *et al.* (1994) is strictly two-dimensional, whereas in Bakchinov *et al.* (1995) TS waves in the presence of artificial steady streaks exhibit a pronounced three-dimensional nature. Furthermore, the forcing frequency used in Boiko *et al.* (1994) lies inside the unstable region

of the neutral curve calculated from the Orr-Sommerfeld equation, but Bakchinov *et al.* (1995) showed that in the presence of streaks, instabilities emerged from broadband low-level noise with frequencies higher than the conventional Orr-Sommerfeld theory would suggest. In fact, Bakchinov *et al.* (1995) studied the effect of ribbon forcing at two different frequencies and for the higher frequency *only*, the TS waves grew faster than predicted by Orr-Sommerfeld theory at some spanwise locations.

Cossu & Brandt (2002) studied the impulse response of a boundary layer perturbed by optimal streaks with numerical simulations. The streaks were forced by the optimal inlet conditions and were therefore steady. On the other hand, the impulse used to trigger the instability effectively excited all possible frequencies at once, and downstream the most unstable dominated. In the temporal analysis, the behaviour depended on the amplitude of the streaks after the initial transient: with no streaks the disturbance energy grew in line with linear theory, but for streak amplitudes 14–26%, this growth was reduced. The stabilising effect of the streaks was ascribed to the mean flow which was slightly distorted from the Blasius profile into a fuller shape which resembled an FPG boundary layer. In a subsequent paper Cossu & Brandt (2004) calculated the nonlinear evolution of the optimal perturbations, and extracted the streak profiles at a particular downstream location. Then they studied the stability of this base flow to linear perturbations with a Floquet expansion to account for the spanwise periodicity of the basic flow. They showed that the contribution of the spanwise Reynolds stress to the energy balance of the TS-type waves was negative and consequently the streaks reduced the growth rate of the instability.

The research cited above sought to investigate TS waves in streaky boundary layers but invoked simplifying assumptions which neglected some of the three-dimensional and unsteady characteristics of both the TS-instability in perturbed boundary layers and the

streaks themselves. For instance, using the optimally growing streaks ignores the fact that in naturally occurring boundary layers perturbed by FST, the streaks are innately unsteady, random and constantly overlapping. Abu-Ghannam & Shaw (1980) experimentally investigated the effect of turbulence on natural transition and compared their data to a range of other experiments. The trend is clear and monotonic, even in the range of turbulent levels 0–1% where TS waves have been observed: increasing FST intensity makes the transition process occur at a lower Reynolds number.

This may be due to a variety of factors, for example independent of the effect on the primary TS instability, the action of the FST could be to trigger secondary instability more effectively. However, the alternative explanation suggested by Kendall (1990) is contrary to the view that TS waves are stabilised by streaks. Kendall (1990) observed TS waves with FST levels around 0.2% and as the turbulence level increased leading to stronger streaks, the growth rate was enhanced. From the literature cited above, there still remains debate on the action of low-level FST in TS wave transition. However there is consensus that as the FST level is raised higher still, TS waves play little or no role in transition on flat-plate boundary layers.

1.2.2 Bypass transition

The growth of elongated streamwise-velocity perturbations inside the boundary layer which are due to FST has been the subject of a wealth of research starting with experiments by Klebanoff (1971). For levels of FST above $0.5 - 1\%$ Arnal & Juillen (1978) showed that the dominant disturbances inside the perturbed boundary layer cannot be easily related to TS waves. With high levels of turbulence, transition can be complete by $R = 600$ in terms of the Blasius length scale and the natural route to transition is said to have been ‘bypassed’.

The term bypass actually pertains to all transition scenarios where TS waves do not play a major role, such as transition due to pronounced surface roughness, but it is commonly understood as transition induced by FST. In contrast to natural transition, where streaks modify the growth of TS waves which are essentially an instability of the two-dimensional boundary layer, the Klebanoff distortions play an essential part in bypass transition.

For many years after the linear instability of the Blasius boundary layer had been calculated, processes involved in bypass remained obscured. Taylor (1936) was the first to argue that the difficulty in observing TS waves experimentally was due to a transition mechanism caused by free-stream turbulence. He suggested that localised separations, caused by impinging eddies, triggered inflectional instabilities which lead to turbulence. At that time the focus was on validating the existence of TS waves, and despite the practical significance of transition in the presence of FST, the phenomenon did not receive sufficient attention. Morkovin (1969) coined the term 'bypass' in 1969, but the reviews of Herbert (1988) and Kleiser & Zang (1991) still referred to the transition in the presence of high levels of FST coming 'out of the blue', via 'mysterious bypass mechanisms'. Early work alluded to a 'direct' breakdown (Kachanov, 1994), but more recently the growth of streaks and their secondary instability have been established as the precursor to turbulent spots which grow and merge downstream to maintain the upstream edge of the turbulent region (for example Matsubara & Alfredsson, 2001; Jacobs & Durbin, 2001). The dominance of bypass mechanisms in conditions of high FST can be viewed from the perspective of receptivity. Saric *et al.* (1999) argued that TS waves were predominantly receptive to acoustic perturbations, whereas vortical disturbances, manifested as turbulence, were linked to the three-dimensional aspects of breakdown. This was supported by the work of Bertolotti (1997) who conducted simulations of a boundary layer perturbed by individual free-stream

vortical modes with the parabolised stability equations (PSE). When a mode with the same frequency as the TS wave was input, the response inside the boundary layer was weak, but low-frequency forcing induced strong streak-like perturbations.

The notion that the next stage of bypass transition, after the growth of Klebanoff distortions, is a secondary instability due to the streaks themselves can be traced back to associated work on Görtler vortices. Boundary layers on curved surfaces develop streamwise oriented vortices due to a centrifugal instability, and via the displacement of mean momentum, steady perturbations of streamwise velocity result, similar to boundary-layer streaks. Swearingen & Blackwelder (1987) used this distorted flow as an experimental model for a flat-plate boundary layer with streaks. They observed breakdown to turbulence and identified antecedent 'instability oscillations'. Two types of secondary instability were possible, distinguished by the symmetry of the velocity perturbations. The most unstable sinuous mode exhibited meandering oscillations of the streamwise streaks, thus the spanwise velocity perturbation alternated downstream but did not vary in the span. The less unstable varicose mode appeared as an alternate thickening and thinning of the streak, and the spanwise velocity perturbations were symmetric about the centre-line of the streak. The sinuous instability was associated with the spanwise inflection point in the streamwise velocity profile, caused by the vortices. On the other hand, the varicose mode was linked with a wall-normal inflection point in the streamwise velocity (Saric, 1994; Asai *et al.*, 2002).

In the case of flat-plate boundary layers, experiments and numerical simulations support the view that a secondary instability of the streaks leads to breakdown. Matsubara & Alfredsson (2001) reviewed a long series of experiments on boundary layers perturbed by FST in zero pressure gradient and described how streaks undergo high-frequency oscillations prior to breakdown. Jacobs & Durbin (2001) conducted DNS of bypass transition, and a

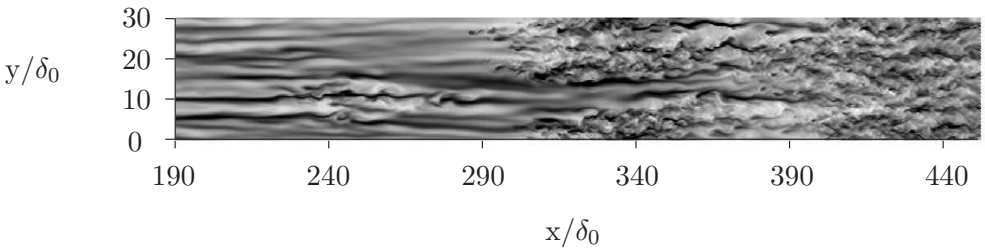

Figure 1.2: Contours of $u-$perturbation showing streaks, secondary instability, spots and and bypass transition. The inlet plane is at $R = 160$ in terms of the Blasius length scale. In the figure, lengths are nondimensionalised by the 99% thickness at the inlet, δ_0. The figure is adapted from a simulation by Jacobs & Durbin (2001).

snapshot of their flow-field is shown in figure 1.2. In their simulation, the inflow consisted of the Blasius flow and FST at an amplitude of $Tu = 3.5\%$. The figure shows contours of $u-$perturbation in the (x, z)-plane. Low-speed streaks caused by the upwelling of low-velocity fluid from close to the wall interacted with the free-stream turbulence at the edge of the boundary layer and rapidly broke down. The same breakdown mechanism was identified more recently by Hernon *et al.* (2007) in their detailed experimental investigation of bypass transition.

Further simulations of boundary layers with synthetic FST, conducted by Brandt *et al.* (2004), showed that the sinuous and varicose instabilities could also be found in transitional flat plate boundary layers perturbed by FST. Additionally, Mans *et al.* (2005, 2007) conducted experiments in a water channel with grid generated turbulence and also observed the sinuous and varicose modes of instability.

Andersson *et al.* (2001) conducted a linear stability analysis on a boundary layer distorted by spanwise periodic streaks, calculated from the evolution of the 'optimal' perturbations. The sinuous and varicose modes were identified, but there was a significant discrepancy between the critical streak amplitude for instability and the experimental evidence. The linear stability analysis predicted a minimum critical amplitude of 26%, whereas

the level of streaky perturbations inside the boundary layer in the experiments by Arnal & Juillen (1978) was much lower, $u_{rms} \sim 5 - 7\%$; Suder *et al.* (1988) also reported modest levels of perturbation around $u_{rms} \sim 5 - 9\%$ before transition. Matsubara & Alfredsson (2001) tracked the downstream evolution of u_{rms} as a function of wall-normal position, and its maximum value reached $\sim 10\%$ before the profile gained a near-wall peak indicative of turbulent flow. The linear results are also at odds with the simulations of Jacobs & Durbin (2001) and Brandt *et al.* (2004), both of which report streak perturbations of approximately $u_{rms} \sim 10\%$ in the transitional region. Although a direct comparison between the critical amplitude calculated by Andersson *et al.* (2001) and the averaged perturbation levels in the experiments does not include the possible effects of localised peaks in boundary layer disturbances, it does show an overall discrepancy.

Two possible explanations have been proposed for the disparity between the intensity of streaks measured in experiments and simulations, and the results from linear analysis. The first is due to Hernon *et al.* (2007) who experimentally studied the velocity perturbations inside a boundary layer forced by grid generated FST. They found that the statistical measures of velocity fluctuations, such as the u_{rms} values quoted above, can obscure significant instantaneous fluctuations. Using 10s sample periods, they recorded a disturbance level of approximately $u_{rms} \sim 10\%$ at the onset of transition but demonstrated that peak negative fluctuation values could reach as high as 40% of U_∞ which is in excess of the critical amplitude calculated by Andersson *et al.* (2001).

Another explanation is suggested by observing the evolution of the secondary instabilities themselves, in the streaky boundary layer. The DNS of Brandt *et al.* (2004) show a varicose breakdown which is incipient in a *streamwise* location between high and low speed streaks. Brandt & de Lange (2008) conducted DNS of carefully controlled collisions

between high- and low-speed streaks of approximately 28%. They also observed a varicose breakdown, which had its origin in the strong wall-normal shear layers resulting from head on collisions. These scenarios of instability indicate the importance of streamwise variation in the background flow, and this is not accounted for in the work of Andersson *et al.* (2001) because optimal *steady* streaks were used as a base flow in that work. In the case of sinuous instabilities, the experimental work of Mans *et al.* (2007) further supports this interpretation. Nascent sinuous instabilities in a boundary layer perturbed by FST were captured originating at the upstream terminus of a low speed streak.

In addition to the already complicated picture of secondary instabilities in bypass transition outlined above, recent simulations have renewed the interest in leading edge effects. Nagarajan *et al.* (2007) carried out DNS of bypass transition in zero pressure-gradient with two different super-elliptic leading edges. When the sharper leading edge with an aspect ratio of 10 was used, transition proceeded along the lines of Jacobs & Durbin (2001). However, the more blunt leading edge with an aspect ratio of 6 enabled a different type of transition. Wave packets initiated close to the wall amplified and broke down, unlike the instabilities observed with the sharp leading edge which were excited close to the edge of the boundary layer. Ovchinnikov *et al.* (2008) also carried out DNS of bypass transition with a leading edge, and two different turbulence length scales were investigated. With the larger length scale ($UL_{11}/\nu = 6580$) boundary layer streaks were still observed, but were found to play a less significant role. Turbulent spots were initiated after the growth of wavepackets inside the boundary layer with spanwise-vortical structures which became Λ-shaped vortices.

Leading edge effects were considered by Goldstein *et al.* (1992) who showed that wall-normal vorticity distorted at the leading edge could lead to a small-amplitude spanwise motion which caused $O(1)$ changes in the boundary layer flow downstream. Subsequently,

the origin of the wave-packets observed in the DNS of Nagarajan *et al.* (2007) was addressed by Goldstein & Sescu (2008), who extended the work by Goldstein *et al.* (1992). They demonstrated that small, low-frequency unsteady vortical perturbations near the leading edge caused distortions to the boundary layer downstream, which could support Rayleigh-type inviscid instabilities. Specifically, the results predicted a wave packet originating near the wall, similar to that observed by Nagarajan *et al.* (2007). These recent works support the emerging view that unsteady Klebanoff distortions can trigger two instabilities leading to bypass transition: the *outer* instability proposed by Jacobs & Durbin (2001) which may be related to the streak instabilities found by Andersson *et al.* (2001) and others; and the *inner* instability first found by Nagarajan *et al.* (2007) in the presence of a leading edge.

1.3 Motivation

In the presence of free-stream turbulence, it is well established that boundary layers naturally develop high-amplitude streaks which can severely affect the transition process. The exact role that streamwise velocity perturbations play, however, is not clear and a variety of perspectives have been presented in the literature. There is some discord about the effect that streaks have, but this could be explained by the different experimental conditions and assumptions made in formulating the base flow used in the analyses.

In the case of natural transition, FST is well known to bring about transition to the turbulent state further upstream, and observations by Kendall (1991, 1998) indicated an increase in TS wave activity in the presence of FST. More recently DNS by Nagarajan *et al.* (2007) and Ovchinnikov *et al.* (2008) have illustrated that wave packets close to the wall can grow and break down in the presence of high amplitude FST, but their relationship to TS waves remains unclear. Other experiments, however, have noted a stabilising effect

of streaks on TS waves, which was also found in the linear stability analysis by Cossu & Brandt (2004) for steady streaks.

A linear stability approach has also been used to study streak instabilities, associated with bypass transition. In this case too, there is some discrepancy between experiments and the analysis: Andersson *et al.* (2001) calculated a critical streak amplitude of 26% whereas experiments and DNS show transition in boundary layers with streak perturbation levels of $5 - 15\%$ (Arnal & Juillen, 1978; Suder *et al.*, 1988; Matsubara & Alfredsson, 2001; Jacobs & Durbin, 2001; Brandt *et al.*, 2004).

Most analyses of the stability of a boundary layer with streaks, conducted up to now, have assumed a base flow consisting of a Blasius profile perturbed by the nonlinear evolution of the optimal initial conditions. These initial disturbances are located well inside the boundary layer, so their link to FST is unclear. Also, the streaks calculated downstream are steady whereas naturally occurring streaks are unsteady and overlapping, and this could be the source of the discrepancy with the experimental results. The importance of unsteadiness has been suggested by instantaneous views of instabilities in experiments and DNS (Brandt *et al.*, 2004; Mans *et al.*, 2007) . The complex and random flow inside boundary layers perturbed by FST contains a range of frequencies, and localised high perturbation amplitudes or gradients could have a significant effect. However, simplified theoretical analyses have been made with just one frequency, for example by Wu & Choudhari (2003) and Goldstein & Sescu (2008). Both works emphasise that unsteadiness in the base state can lead to an instability that would not be present if the initial perturbations stimulating the streaks were steady.

A framework is developed herein for studying the stability of boundary layers perturbed

by streaks which accounts for their origin in the unsteady free-stream turbulence. Free-stream modes with low frequencies are known to stimulate streaks more effectively than high frequency modes, but it is not clear which frequencies inside the boundary layer are the most significant in transition. For this reason, streaks with different frequency and amplitude are considered in the current analysis.

1.4 Overview

To study the influence of streaks on boundary layer stability, a base flow must first be established. The natural boundary layer perturbed by FST contains a low-frequency broadband spectrum of complex random fluctuations which would yield an intractable stability problem. However, recent work on the 'continuous mode' model for bypass transition (Zaki & Durbin, 2005; 2006; Durbin & Wu, 2006) shows that just one low-frequency Fourier component of the FST can be used to generate streaks and recover realistic bypass transition scenarios. The base flow ansatz used in the present stability analysis therefore also uses a particular free-stream mode with frequency and wavenumbers chosen to reflect boundary layer streaks caused by FST. A schematic of the proposed model is shown in figure 1.3. The free-stream mode triggers Klebanoff streaks which grow downstream as shown in the figure. Since the model includes unsteadiness in the streaks, the alternating streaks with positive and negative fluctuations are observed at a single spanwise location, and they can overlap in the wall-normal direction. The main focus of this research is the instability of the boundary layer flow with streaks. When the flow becomes unstable, instabilities grow and merge and the boundary layer becomes fully turbulent. Using the simplified model here, the amplitude and frequency of the free-stream mode are varied in order to investigate their influence on the streaks, and in turn, the boundary layer stability.

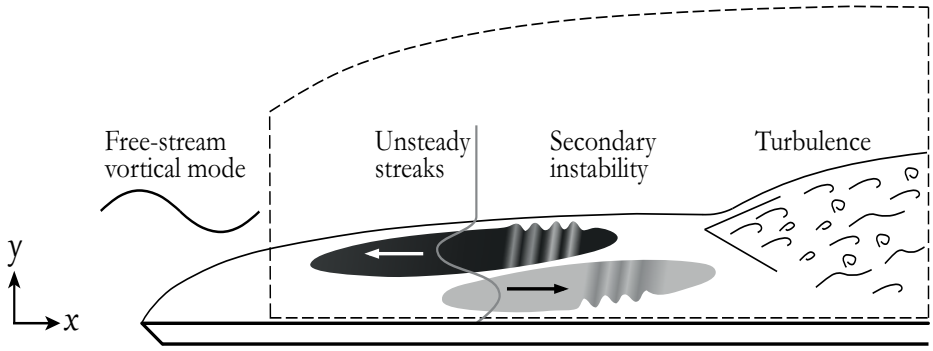

Figure 1.3: Schematic of boundary layer transition due to a free-stream vortical mode.

The base flow is composed of a mean boundary layer flow and the streaks, and in order to study its linear stability, infinitesimal perturbations are introduced. By deriving the stability equations, an eigenvalue problem is formed. Coefficients of the stability equations include base flow terms, and because the streaks are periodic in the spanwise direction, Floquet theory is invoked in the solution method. In the analysis of steady free-stream modes, the normal mode assumption, familiar from Orr-Sommerfeld analysis, is invoked in the streamwise and temporal dimensions. Unsteady streaks, however, are more complicated, the low frequency of the base flow suggests that a quasi-steady approximation to the streaky flow could be used (Wu & Choudhari, 2003). However this assumption is based on the premise that the relevant instability growth rate is much higher than the frequency of the base flow (Kerczek & Davis, 2006; Luo & Wu, 2010). Clearly, around the neutral conditions for instability, this is not satisfied and therefore a fully unsteady analysis is undertaken which accounts for all phases of the unsteady base flow. Wu & Choudhari (2003) posed the question of how quasi-steady analyses relate to the global Floquet modes and this issue is addressed herein.

This thesis is divided into five chapters. In chapter one, the physical problem of boundary layer transition was introduced and the richness and variety of the phenomena was emphasised. Discrepancies between experiments and previous analyses motivated studying

the stability of a more realistic unsteady base flow. A set of objectives for the remaining chapters is given below:

1. Find the secondary instability of unsteady streaks.

2. Gain understanding of the instability modes, particularly how their mechanisms relate to shear and unsteadiness in the base flow.

3. Investigate the behaviour of the linear instability modes in non-linear simulations, to assess their potential role in bypass transition.

4. Relate the findings of the instability analysis and DNS to previous experiments and simulations from the literature.

A preliminary analysis is conducted in chapter two, which employs a linear method to calculate unsteady streaks. This shows that the boundary layer becomes more unstable with increasing streak amplitude and frequency. Two types of instability are found, and the growth rate depends on the streak frequency and amplitude: One is linked to the TS wave, and the other is a streak instability. Simulations show that both modes of instability are capable of causing breakdown. In chapter three, direct numerical simulations are performed to calculate a base flow which takes nonlinear and non-parallel effects into account. The stability problem for this base flow is also formulated and, in chapter four, the linear stability results are presented. The findings from chapter two are extended in the context of streaks calculated from DNS, and the effects of nonlinearity and unsteadiness are explored. The structure of the modes and their nonlinear breakdown are studied with DNS. The main conclusions from the work are presented in chapter five.

Chapter 2

Stability of linear streaks

2.1 Introduction

Linear stability methods have been applied to shear flows since the end of the nineteenth century. In 1879, Rayleigh derived the governing inviscid equations for a base flow which depended on the wall normal direction only. It was noted that an inflection point in the base flow was a necessary condition for instability, therefore the exponential instability of Blasius boundary layers could not be explained by inviscid theory. The seminal Orr-Sommerfeld shear-flow stability equations, which included the effects of viscosity were derived independently by Orr (1907) and Sommerfeld (1908). In the absence of streaks, the solutions of the Orr-Sommerfeld equation for boundary-layer flow include the TS instability, and the eigen-solution accurately describes its exponential growth and the early stages of natural transition.

Observations from experiments and numerical simulations indicate that instabilities also grow and lead to breakdown when the boundary layer is distorted by streaks. When the free-stream turbulence level is low, the dominant instability is still the TS wave, albeit modified by the presence of streaks (Kendall, 1990; Grek *et al.*, 1990). If the turbulence intensity

is above approximately 1% of U_∞, then instabilities associated with the bypass mechanism take over (Matsubara & Alfredsson, 2001; Jacobs & Durbin, 2001; Nagarajan *et al.*, 2007). The conditions required for the instability directly precede the onset of transition. Therefore, in order to assess the influence of streaks on stability, a linear perturbation analysis of streaky boundary layers is carried out. Linear stability alone does not take into account the issue of receptivity, nor the nonlinear evolution of the instability into the final stages of breakdown. However, it does address the key question of the role played by unsteadiness of the base flow in the inception of instabilities and the early phases of the transition process.

In chapter one, it was postulated that the shortcomings in previous stability analyses of boundary layers with streaks were due to the model used for the base flow. In this chapter, that hypothesis is tested with a preliminary study of a streaky boundary-layer flow forced by unsteady free-stream perturbations. First the method for calculating the base flow is described, and some typical streak profiles are presented. Then the secondary stability equations are derived and the assumed form of the solution is given. The computer code used to solve the equations is then validated, based on test cases with data for comparison from the literature. After the linear stability tool has been established, the streaky boundary layer is investigated. Two modes of instability are found, and the influence of streak amplitude and frequency are examined. After calculating the linear instability modes, results from direct numerical simulations are presented which illustrate their nonlinear evolution and breakdown.

2.2 Theoretical formulation

The stability of boundary layers with embedded streaks is studied in the framework of a linear secondary instability analysis. This approach considers perturbations to a base state,

u_2 which is a superposition of a mean flow and a primary saturated disturbance,

$$u_2(x, y, z, t) = U_0(y) + A_u u_1(x, y, z, t). \tag{2.1}$$

In the current context, these are the Blasius profile $U_0(y)$ and a Klebanoff streak $u_1(x, y, z, t)$, where x, y, z, and t are the streamwise, wall-normal, spanwise directions and time, respectively. The streak is unsteady and three-dimensional with amplitude A_u. Since u_2 is periodic, Floquet expansions in the streamwise and spanwise directions are used to formulate the stability problem. In this section, the model of the base flow is discussed, followed by the formulation of the eigenvalue problem.

2.2.1 Base flow

Naturally occurring streaks in boundary layers are caused by turbulence in the free stream, which contains a spectrum of frequencies and wavenumbers. Here, a base flow for the stability analysis is calculated from the boundary layer response to one Fourier mode of the FST. This is calculated in two stages: first the signature of the free-stream disturbance inside the boundary layer is calculated, which addresses the issue of receptivity; second the evolution of streaks, triggered by normal velocity coupling with the boundary layer shear, is computed.

The amplitude of the free-stream disturbances considered is on the order of a few percent, therefore they are roughly two orders of magnitude smaller than the free-stream velocity. As such, they have often been treated as linear perturbations (for example Jacobs & Durbin, 2001). The linear stability equations for the two-dimensional boundary layer flow are given below.

$$\left[\left(\frac{\partial}{\partial t} + U_0\frac{\partial}{\partial x} - \frac{1}{R}\nabla^2\right)\nabla^2 - \frac{d^2U_0}{dy^2}\frac{\partial}{\partial x}\right] v_1 = 0, \tag{2.2a}$$

$$\left(\frac{\partial}{\partial t} + U_0\frac{\partial}{\partial x} - \frac{1}{R}\nabla^2\right)\eta_1 = -\frac{dU_0}{dy}\frac{\partial v_1}{\partial z}. \tag{2.2b}$$

The Reynolds number is given by $R = U^*_\infty L^*_B/\nu^*$, where * indicates a dimensional quantity, U^*_∞ is the free-stream velocity, ν^* is the kinematic viscosity, and the Blasius length scale is defined by $L^*_B = \sqrt{\nu^* x^*/U^*_\infty}$. The mean flow, U_0, nondimensionalised by U^*_∞, is given by the Blasius solution for flow over a flat plate. The spatial dimensions and time, given by x, y, z and t respectively, are nondimensionalised by L^*_B and L^*_B/U^*_∞. The normal-velocity and vorticity perturbations are denoted by v_1 and η_1. The parallel flow assumption is invoked, therefore the mean flow is defined at a particular streamwise location, x^*, and assumed not to change with the nondimensional x and the wall-normal component of the base flow is assumed negligible. The boundary layer assumptions have been used widely in stability analyses. For example it was used in calculating the Tollmien-Schlichting instability, optimal transient growth (Butler & Farrell, 1992; Cossu *et al.*, 2008), and the stability of streaks (Andersson *et al.*, 2001). The assumption is used throughout this thesis, and is based on the fact that, V_0/U_0, and $\partial U_0/\partial x$ are both $O(1/R)$ for Blasius flow, and in studies of transition, R is of the order of several hundreds.

The continuous modes of the Orr-Sommerfeld equation

The coefficients of equation (2.2) are homogeneous in the x, z and t dimensions, so normal mode solutions can be assumed:

$$\begin{bmatrix} v_1(\boldsymbol{x},t) \\ \eta_1(\boldsymbol{x},t) \end{bmatrix} = \begin{bmatrix} \hat{v}_1(y) \\ \hat{\eta}_1(y) \end{bmatrix} \mathrm{e}^{i(k_x x + k_z z - \omega t)}, \tag{2.3}$$

where k_x and k_z are the streamwise and spanwise wavenumbers, and ω is the frequency. The bold characters represent vector quantities. Substituting the normal mode forms into equation (2.2) leads to an eigenvalue problem for the coupled Orr-Sommerfeld and Squire equations, respectively:

$$\left[(-i\omega + ik_xU_0)(d_y^2 - k^2) - \frac{1}{R}(d_y^2 - k^2)^2 - ik_x\frac{d^2U_0}{dy^2}\right]\hat{v}_1 = 0, \tag{2.4a}$$

$$\left[(-i\omega + ik_xU) - \frac{1}{Re}(d_y^2 - k^2)\right]\hat{\eta}_1 = -ik_z\frac{\partial U_0}{\partial y}\hat{v}_1, \tag{2.4b}$$

where d_y indicates the derivative with respect to y and $k^2 = (k_x^2 + k_z^2)$. The boundary conditions at the wall are

$$\hat{v}_1(y=0) = \hat{v}_1'(y=0) = \hat{\eta}_1(y=0) = 0. \tag{2.5}$$

For the semi-bounded flow over a plate, there are two possible types of boundary conditions in the free stream. The whole spectrum of eigen-solutions consists of a finite number of discrete modes and a continuous spectrum, each class corresponding to a different type of free-stream boundary condition. Modes from the discrete spectrum have most of their energy inside the boundary layer, and outside of the boundary layer they decay with increasing distance from the wall. Their free stream conditions are,

$$\hat{v}_1, \hat{v}_1', \hat{\eta}_1 \to 0 \text{ as } y \to \infty. \tag{2.6}$$

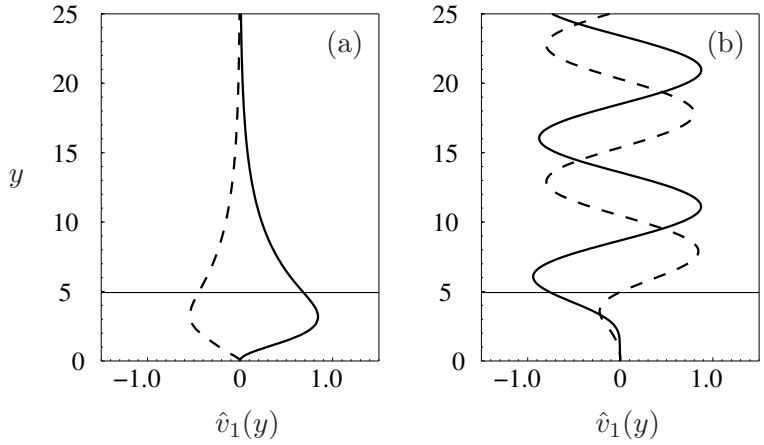

Figure 2.1: Vertical velocity mode shapes: (a) two-dimensional discrete mode at $R = 200$; (b) continuous mode with $k_x = 0.0300$, $k_y = k_z = 0.6379$. (——) Real$\{\hat{v}_1(y)\}$, (- - -) Imag.$\{\hat{v}_1(y)\}$.

The continuous modes, are purely oscillatory in the free stream with a wavenumber k_y, and the boundary conditions are,

$$\hat{v}_1, \hat{v}_1', \hat{\eta}_1 \text{ bounded as } y \to \infty. \tag{2.7}$$

Inside the boundary layer, continuous modes decay towards the wall depending on the Reynolds number and their wavenumbers. Examples of the wall-normal shape for both a discrete and continuous mode are exhibited in figure 2.1.

Grosch & Salwen (1978) first established that the entire spectrum forms a complete basis, and any disturbance can be described as a sum over the eigenfunctions. In a later paper, Salwen & Grosch (1981) solved the initial-value problem for the temporal growth of perturbations. It was demonstrated that a patch of free-stream vorticity could be represented by the continuous modes. Continuous modes were subsequently shown by Jacobs & Durbin (2001) to be a useful way to describe FST. In their simulations of bypass transition, the inlet plane was downstream of the leading edge, and the inflow included synthetic turbulence formed by a superposition of modes from the continuous spectrum. Zaki & Durbin (2005)

reproduced the main features of bypass transition with a canonical simulation including streaks which were forced by just one long-wavelength continuous mode. Therefore, in the present study the effect of free-stream disturbances inside the boundary layer is modelled with modal solutions from the continuous spectrum of the Orr-Sommerfeld operator.

Following Jacobs & Durbin (1998), the solution for the continuous mode is guided by the behaviour of the Orr-Sommerfeld equation in the free stream. Outside of the boundary layer, where $U_0(y) = U_\infty$, the Orr-Sommerfeld equation becomes a fourth order differential equation in y with constant coefficients,

$$\left[(\partial_y^2 - k^2)^2 - ik_x R\big((U_\infty - c)(\partial_y^2 - k^2)\big)\right] \hat{v}_1 = 0, \tag{2.8}$$

where the phase speed of the solution $c = \omega/k_x$. This equation suggests solutions of the form $\hat{v}_1 = \mathrm{e}^{\lambda y}$, and substituting this into equation (2.8) leads to a characteristic equation,

$$([k_x^2 + k_z^2] - \lambda^2)(\lambda^2 - [k_x^2 + k_z^2] - iR[k_x U_\infty - \omega]) = 0, \tag{2.9}$$

with four roots:

$$\lambda_{1,2}^2 = k_x^2 + k_z^2 + ik_x R(U_\infty - c), \tag{2.10a}$$

$$\lambda_{3,4}^2 = k_x^2 + k_z^2. \tag{2.10b}$$

The roots $\lambda_{3,4}$ represent solutions which exponentially decay and grow with y, and the latter is rejected because it is not physical. If $\lambda_{1,2}$ have zero real part, $\lambda_{1,2} = \pm ik_y$ and the two solution components are oscillatory. In this case, the superposition of admissible solutions

describes the behaviour of a continuous mode in the free stream,

$$\hat{v}_1 \sim C_1 \mathrm{e}^{+ik_y y} + C_2 \mathrm{e}^{-ik_y y} + C_3 \mathrm{e}^{\lambda_3 y}. \tag{2.11}$$

Substituting k_y into (2.10a) leads directly to a dispersion relation for continuous modes,

$$\omega = k_x U_\infty - \frac{i}{R}(k_x^2 + k_y^2 + k_z^2). \tag{2.12}$$

With this analytic form for the eigenvalue, the Orr-Sommerfeld problem can be solved for the continuous modes as a boundary value problem,

$$\left[(-i\omega + ik_x U_0)(\partial_y^2 - k^2) - \frac{1}{R}(\partial_y^2 - k^2)^2 - ik_x \frac{d^2 U_0}{dy^2}\right] \hat{v}_1 = 0, \tag{2.13a}$$

with boundary conditions,

$$\hat{v}_1(y = 0) = 0, \tag{2.13b}$$

$$\hat{v}_1'(y = 0) = 0, \tag{2.13c}$$

$$\hat{v}_1(y_\infty) = 1, \tag{2.13d}$$

$$\frac{(\hat{v}_1'' + k_y^2 \hat{v}_1)|_{y_1}}{(\hat{v}_1'' + k_y^2 \hat{v}_1)|_{y_2}} = \mathrm{e}^{\sqrt{k_x^2 + k_z^2}(y_2 - y_1)}. \tag{2.13e}$$

The last two boundary conditions correspond to an arbitrary normalisation of the mode shape, and the boundedness condition, proposed by Jacobs & Durbin (1998), which is implemented by relating the solution at two points in the free stream, y_1 and y_2.

The dispersion relation (2.12) shows that all the continuous mode eigen-solutions are damped and decay in time at a rate proportional to $1/R$. Typical continuous mode shapes, $\hat{v}_1(y; R, k_x, k_y, k_z)$, are shown in figure 2.2, and they illustrate the shear sheltering effect

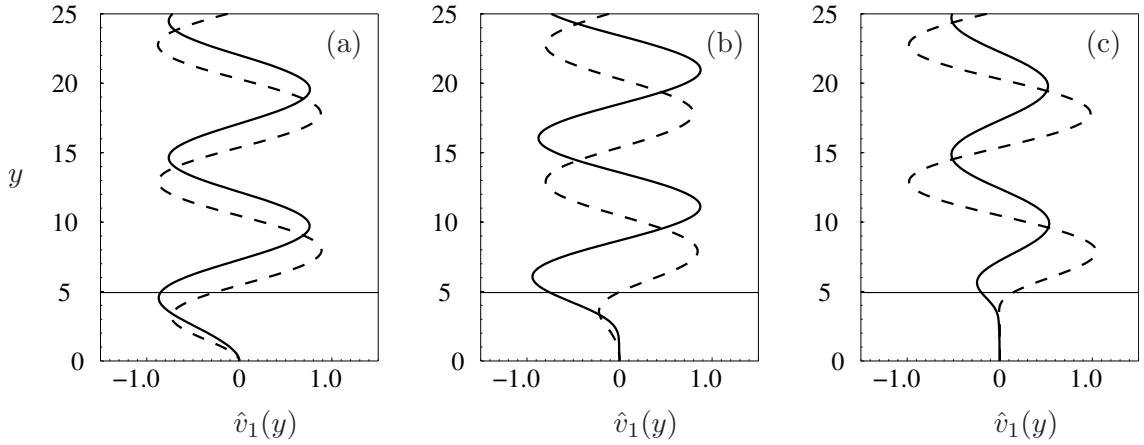

Figure 2.2: Vertical velocity continuous mode shapes, (——) Real$\big(\hat{v}_1(y)\big)$, (- - -) Imag.$\big(\hat{v}_1(y)\big)$. $R = 200$, $k_y = k_z = 0.6379$: (a) $k_x = 0.0035$; (b) $k_x = 0.0300$; (c) $k_x = 0.300$.

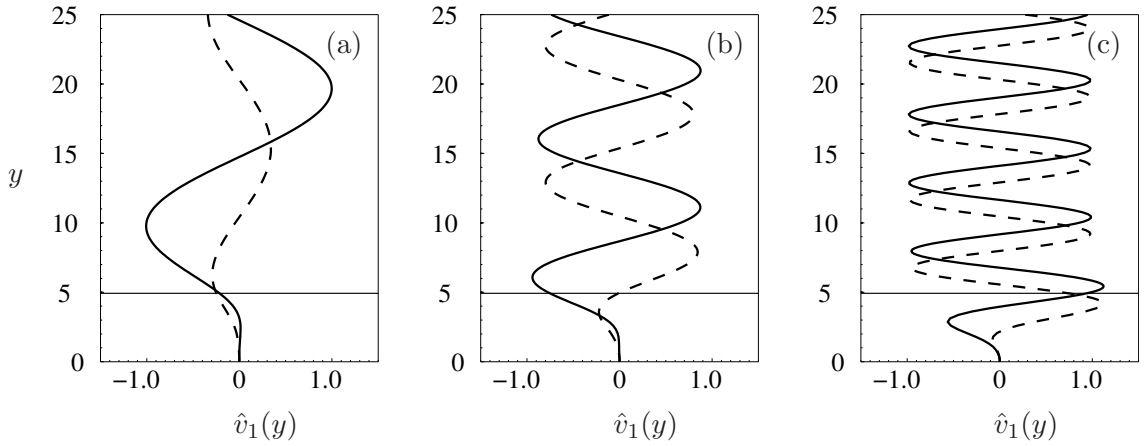

Figure 2.3: Vertical velocity continuous mode shapes, (——) Real$\big(\hat{v}_1(y)\big)$, (- - -) Imag.$\big(\hat{v}_1(y)\big)$. $R = 200$, $k_x = 0.0300$, $k_z = 0.6379$: (a) $k_y = 0.3189$; (b) $k_y = 0.6379$; (c) $k_y = 1.276$.

(Jacobs & Durbin, 1998; Zaki & Saha, 2009). The functions are oscillatory in the free stream and decay with decreasing y close to the wall. As the streamwise wavenumber k_x is increased, the effect of shear sheltering is enhanced, and the v-perturbation penetrates less effectively into the region of mean shear. This phenomenon is closely related to experimental observations of boundary layers subject to FST which illustrate the dominance of long streamwise-wavelengths, and show that penetration is inversely related to frequency (Hernon *et al.*, 2007).

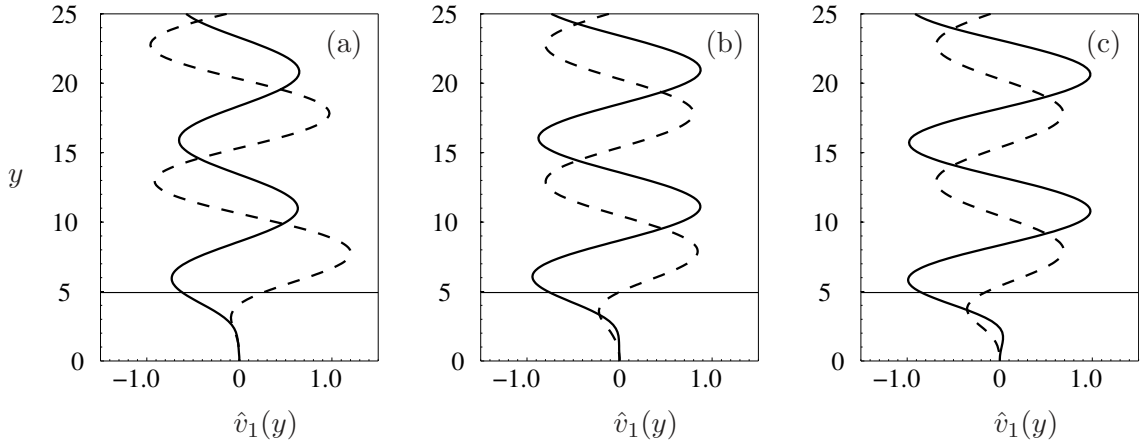

Figure 2.4: Vertical velocity continuous mode shapes, (——) Real$\big(\hat{v}_1(y)\big)$, (- - -) Imag.$\big(\hat{v}_1(y)\big)$. $R = 200$, $k_x = 0.0300$, $k_y = 0.6379$: (a) $k_z = 0.3189$; (b) $k_z = 0.6379$; (c) $k_z = 1.276$.

Spanwise and wall-normal wavenumbers also have an impact on vortical mode penetration and this is illustrated in figures and . Similar to previous results by Zaki & Durbin(2005, 2006), the penetration increases with k_y, but k_z has a small effect. Variations with k_y and k_z are not the main focus of this work, and the rest of the results in this chapter use $k_y = k_z = 0.6379$.

The linear amplification of streaks

Once the signature of the free-stream disturbance on the boundary layer itself is established, the perturbations inside the boundary layer interact with the mean shear which leads to the generation of boundary layer streaks, and that process can also be analysed with linear stability methods. The streaks can grow to a considerable amplitude however, which could bring the linearisation into question. Despite this, Zaki & Durbin (2006) used a linear approach to effectively capture the initial amplification of streaks due to forcing by a normal-velocity continuous mode, and their eventual decay. The analysis used the temporal growth concept, and did not account for non-linearity or non-parallel effects arising from the streamwise growth of the boundary layer. However, when it was compared to DNS of a

spatially evolving boundary layer with a similar normal-velocity forcing at the inlet plane, the streamwise growth of the perturbations agreed well with the linear results.

The work by Zaki & Durbin(2005, 2006) calculated the evolution of the linear streaks by solving an initial value problem (IVP) for the normal-vorticity perturbation. The normal-vorticity equation has a forcing term which includes the normal velocity, and which leads to the transient growth of perturbations inside the boundary layer. Like the Orr-Sommerfeld problem, the solution to the IVP was described in terms of normal modes in x and z, except here the time dependence was generalised,

$$\begin{bmatrix} v_1(\boldsymbol{x},t) \\ \\ \eta_1(\boldsymbol{x},t) \end{bmatrix} = \begin{bmatrix} \tilde{v}_1(y,t) \\ \\ \tilde{\eta}_1(y,t) \end{bmatrix} \mathrm{e}^{i(k_x x + k_z z)}. \tag{2.14}$$

These forms were substituted into (2.2)(b) to yield the normal vorticity equation,

$$\frac{\partial \tilde{\eta}_1(y,t)}{\partial t} = \left(\frac{1}{R}(\partial_y^2 - k^2) - ik_x U_0 \right) \tilde{\eta}_1(y,t) - ik_z \frac{\partial U_0}{\partial y} \tilde{v}_1(y,t), \tag{2.15a}$$

with boundary and initial conditions,

$$\tilde{\eta}_1(y=0,t),\ \tilde{\eta}_1(y\to\infty,t) = 0, \tag{2.15b}$$

$$\tilde{\eta}_1(y,t=0) = 0, \tag{2.15c}$$

can be solved after specifying the forcing from the normal-velocity. Choosing R, k_x, k_y, k_z and solving equation (2.13) for the continuous mode shape $\hat{v}_1(y)$ leads to the formulation of $\tilde{v}_1(y,t) = \hat{v}_1(y)e^{-i\omega t}$. Then the evolution of normal-vorticity is computed, using a spectral technique to resolve the $y-$direction, and numerical integration in time.

In order to calculate the boundary layer response to the free-stream forcing, the normal-vorticity equation (2.15) is solved. The wall-normal dependence of $\tilde{\eta}_1$ is described by an expansion in terms of the Chebyshev polynomials. The spectral method converges exponentially, and Chebyshev polynomials are chosen as a basis because the domain is non-periodic in the $y-$direction. First, the Chebyshev derivative matrices must be defined, which are made up from the values of Chebyshev polynomials and their derivatives at different collocation points. The i^{th} collocation point is given by,

$$\hat{y}_i = \cos(i\pi/N), \tag{2.16}$$

where N is the total number of collocation points. The j^{th} Chebyshev polynomial is defined as,

$$T_j(\hat{y}) = \cos(j\arccos(\hat{y})). \tag{2.17}$$

The i^{th} row of the Chebyshev matrix $\boldsymbol{d}_0$ corresponds to the i^{th} collocation point, and the j^{th} column corresponds to the j^{th} Chebyshev polynomial. The matrices are square and N Chebyshev polynomials are included. The Chebyshev derivative matrices $\boldsymbol{d}_n$ have a similar structure, except the j^{th} column corresponds to the n^{th} derivative of the j^{th} Chebyshev polynomial, $d^n T_j/d\hat{y}^n$.

The Chebyshev polynomials are defined on the domain $\hat{y} = [-1, 1]$, which is not useful for the boundary layer problem with a semi-infinite domain. To solve equation (2.15) using the Chebyshev basis, the Chebyshev domain must be mapped from $\hat{y} = [-1, 1]$ to the domain $y = [0, y_{top}]$. This means that the semi-infinite domain is truncated to a finite height, $y = y_{top}$. Since the formulation for continuous modes in equation 2.11 actually contains a component which decays with y as well as two purely oscillatory components,

the solution domain must be large enough for the decaying component to become negligible on the top boundary. The truncation location, y_{top}, is therefore a point in the free stream which is chosen far enough away from the wall, such that the solution inside the boundary layer is not affected by changing y_{top}. A value of $y_{top} = 40$ was found to be sufficient. The mapping between the two domains $\hat{y} \mapsto y$ is chosen to cluster the collocation points around the boundary-layer shear so that the area with high gradients is better resolved. Specifically, half the grid points are located in the range $y = [0, y_m]$, where y_m was a parameter, chosen near the edge of the boundary layer. The mapping is given by,

$$y = \frac{1 + \hat{y}}{A + \frac{2}{y_{top}} - \hat{y}}, \tag{2.18}$$

where,

$$A = \frac{y_{top} - 2y_m}{y_{top}\, y_m}. \tag{2.19}$$

Using the chain rule, it is straightforward to define the derivatives $d^n T_j / dy^n$, and these derivatives are used to create the mapped Chebyshev derivative matrices. The mapped Chebyshev derivative matrices, $\boldsymbol{D}_n$, are laid out similar to $\boldsymbol{d}_n$, but the j^{th} column corresponds to the n^{th} derivative, with respect to y instead of $\hat{y}$, of the j^{th} Chebyshev polynomial, $d^n T_j / dy^n$.

Having established the mapped Chebyshev derivative matrices, $\tilde{\eta}_1$ is expressed using the expansion,

$$\tilde{\eta}_1 = \boldsymbol{D}_0 \boldsymbol{b}, \tag{2.20a}$$

$$\frac{\partial \tilde{\eta}_1}{\partial y} = \boldsymbol{D}_1 \boldsymbol{b}, \tag{2.20b}$$

$$\frac{\partial^n \tilde{\eta}_1}{\partial y^n} = \boldsymbol{D}_n \boldsymbol{b}, \tag{2.20c}$$

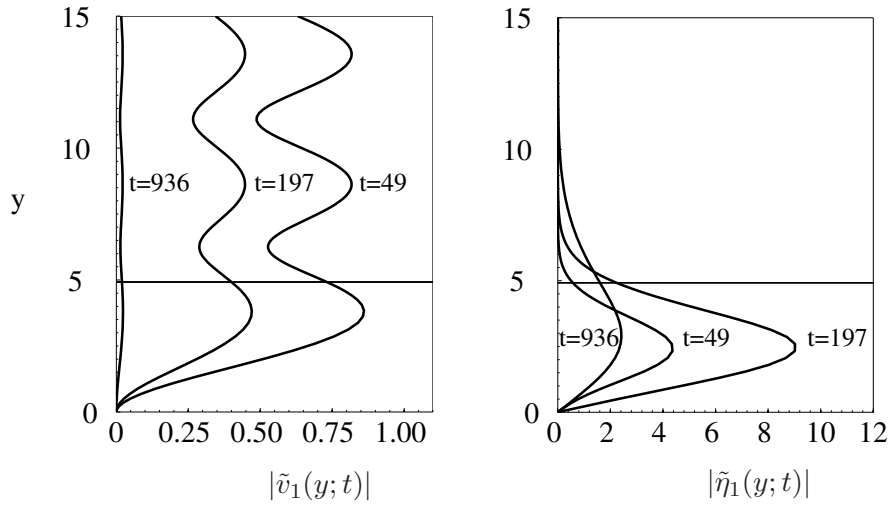

Figure 2.5: At left the decaying normal velocity mode $|\tilde{v}_1(y;t)|$, and at right the transient response of normal vorticity $|\tilde{\eta}_1(y;t)|$. $R = 200$, $k_x = 0.0035$, $k_y = k_z = 0.6379$.

$$\frac{\partial \tilde{\eta}_1}{\partial t} = \boldsymbol{D}_0 \frac{d\boldsymbol{b}}{dt}, \tag{2.20d}$$

where $\boldsymbol{b}$ is the vector of spectral coefficients. Substituting these expansions into equation (2.15a) yields the equation for the time dependence of the spectral coefficients,

$$\frac{d\boldsymbol{b}}{dt} = \boldsymbol{D}_0^{-1}[\frac{1}{R}(\boldsymbol{D}_2 - k^2\boldsymbol{D}_0) - ik_xU_o\boldsymbol{D}_0]\boldsymbol{b} - ik_z\frac{\partial U_0}{\partial y}\tilde{v}_1. \tag{2.21}$$

Equation (2.21) was solved with the initial conditions $\boldsymbol{b}(t = 0) = 0$, using an implicit, multistep time integration algorithm. The above algorithm was implemented by the author's fellow student, S. Saha. To ensure convergence, three hundred Chebyshev polynomials were used to resolve the wall-normal direction.

The results from solving equation (2.15a) with forcing from a continuous mode exhibit an initial growth of normal vorticity, whilst the forcing from the normal velocity is effective, followed by decay due to viscosity. This is illustrated in figure 2.5. Note that $|\tilde{\eta}_1|$ only grows close to the wall where mean shear is present because the forcing to the normal vorticity equation is proportional to $U_0'\tilde{v}_1$.

Considering the forcing term also demonstrates the importance of coupling between the mean shear and the normal velocity (Zaki & Durbin, 2005), and the importance of shear sheltering. Only normal velocity modes which penetrate into the boundary shear can force the normal vorticity. In figure 2.6, a comparison is made between the effects of a highly- and a moderately-penetrating normal-velocity modes, corresponding to figures 2.2(a) and (b). The streamwise-velocity perturbation is plotted, and is calculated from the normal velocity and vorticity,

$$\tilde{u}_1(y,t) = \frac{i}{k_x^2 + k_z^2}\left(k_x \frac{\partial \tilde{v}_1(y,t)}{\partial y} - k_z \tilde{\eta}_1(y,t)\right). \tag{2.22}$$

For low-k_x modes, the normal velocity is directly proportional to normal vorticity. In figure 2.6, the maximum in y of $|\tilde{u}_1(y,t)|$ is shown as a function of time, for the two different forcing modes with unit initial amplitude.

The rapid initial growth of the streamwise velocity depends strongly on how much the normal velocity-forcing couples to the mean shear, $U_0'\tilde{v}_1$. Therefore, the streamwise wavelength of the forcing perturbation affects the amplitude of the response downstream. Long-wavelength continuous modes, which penetrate deeply into the boundary region, stimulate the streaks to a high amplitude more effectively than short-wavelength modes. This demonstrates the consequences of shear sheltering on the development of Klebanoff streaks.

The streamwise velocity is a dynamic response to forcing from an oscillatory, albeit decaying, normal-velocity mode. Its full time dependence is therefore composed of both an oscillatory component with frequency Real$\{\omega\}$, and the transient growth and decay which is illustrated in figure 2.6. This can be understood in the context of analytical work on the IVP by Zaki & Durbin (2005, 2006). It was shown that the normal vorticity response

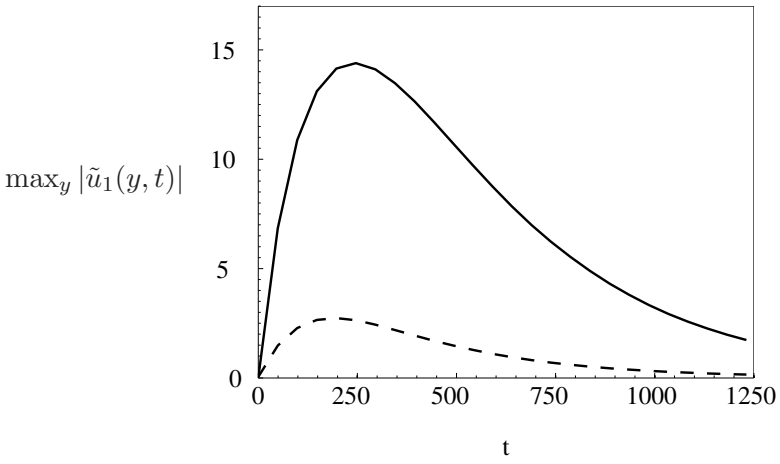

Figure 2.6: The evolution of streamwise velocity perturbation response, at $R = 200$, due to free-stream forcing with $k_x = 0.0035$ (——); $k_x = 0.0300$ (- - -), and $k_y = k_z = 0.6379$.

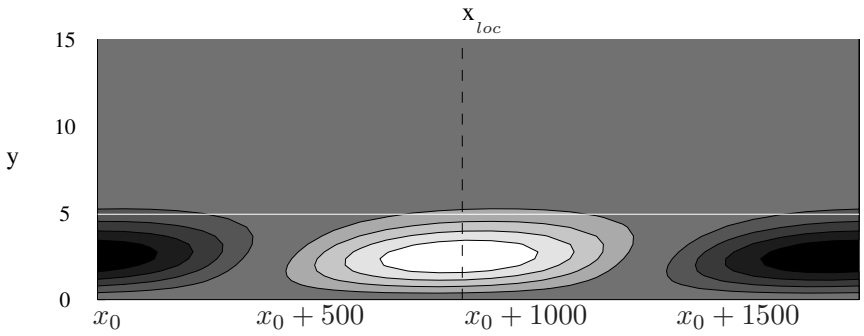

Figure 2.7: Contours of u_1 in the $x - y$ plane. Parameters for the forcing Orr-Sommerfeld mode are $R = 200$, $k_x = 0.0035$, $k_y = k_z = 0.6379$. Light and dark contours mark positive and negative velocity perturbations, respectively.

to forcing from a continuous Orr-Sommerfeld mode consists of the entire k_y-spectrum of Squire modes with the same k_x and k_z as the forcing. Each mode in that spectrum has a frequency with the same real part as the forcing but a different decay rate.

Since the transient behaviour takes place on a long time-scale governed by the decay rate of the forcing mode, it is not accounted for in the formulation of the base flow for the stability analysis. This is reasonable because the goal of the stability analysis is to demonstrate the effect of streak oscillation at a particular downstream location. In a natural boundary layer exposed to FST, the forcing in the free-stream is constant in time which means that for

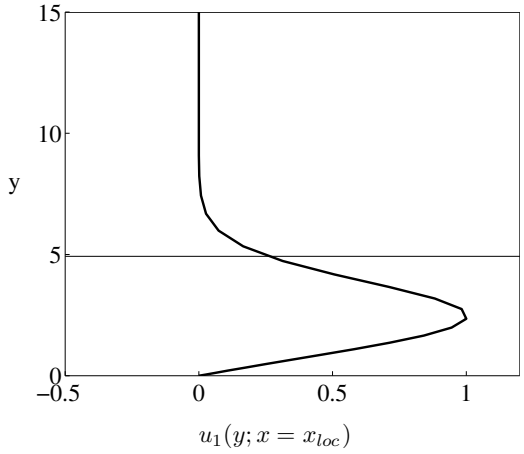

Figure 2.8: The wall normal profile of the streamwise velocity, u_1, extracted from figure 2.7 at the location marked x_{loc}.

any particular streamwise location, the primary disturbance amplifies to an approximately constant level, in the time averaged sense. The base flow is therefore constructed as,

$$u_2(x, y, z, t) = U_0(y) + A_u u_1(x, y, z, t), \tag{2.23}$$

where,

$$u_1(x, y, z, t) = \text{Real}\{\hat{u}_1(y) e^{i(k_x x - \omega_r t)}\} \cos(k_z z). \tag{2.24}$$

The complex mode shape, $\hat{u}_1(y)$ is given by $\tilde{u}_1(y, t)$ at the time of the maximum transient response, and $\omega_r = \text{Real}(\omega)$. The forcing is provided by two oblique continuous modes with opposite spanwise wavenumber $\pm k_z$. This yields a solution that does not translate in the spanwise direction, which is consistent with streaky boundary layers observed in experiments. Due to the linearity of the problem, the solution u_1 can be normalised such that its maximum value is unity, and then scaled with the amplitude A_u. Experimental observations have shown that the streamwise component of velocity dominates in boundary layers perturbed by FST, and the present linear results also show this (see for example figure 2.6), therefore the wall-normal and spanwise components, v_1 and w_1, are not accounted for

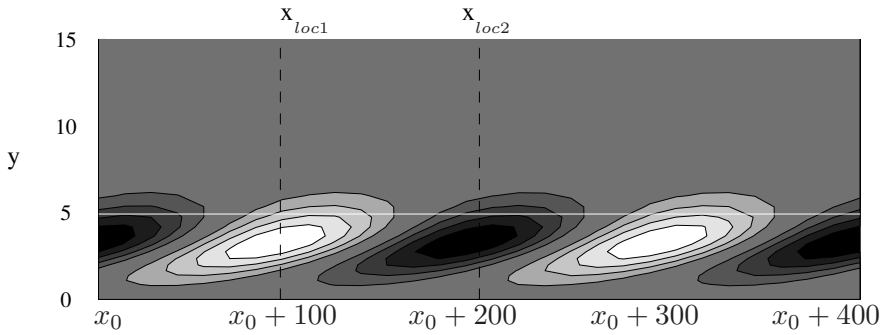

Figure 2.9: Contours of u_1 in the $x - y$ plane. Parameters for the forcing Orr-Sommerfeld mode are $R = 200$, $k_x = 0.0300$, $k_y = k_z = 0.6379$. Light and dark contours mark positive and negative velocity perturbations, respectively.

in the base flow.

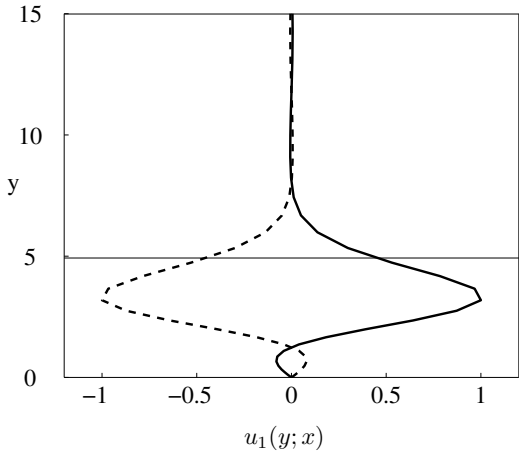

Figure 2.10: The wall normal profile of the streamwise velocity, u_1 extracted from the case in figure 2.9 at the locations indicated x_{loc1} (——), and x_{loc2} (- - -).

To illustrate the structure of the streamwise velocity response inside the boundary layer, a side view of the contours of u_1 is shown in figure 2.7. The alternation between high- and low-speed streaks in the streamwise direction is made clear, and at a streamwise location of a positive perturbation, marked x_{loc}, the streak profile is extracted and plotted in figure 2.8.

The amplitude of the streamwise velocity response was shown to depend on the wavelength for a given initial amplitude of $\tilde{v}_1$ in figure 2.6, but the shape of the u_1-velocity perturbation also depends on k_x. Figure 2.9 shows contours of u_1 in a side view for a higher

wavenumber than in figure 2.7. The peaks in positive and negative fluctuations occur at the same wall normal location which is not representative of the complex flow in natural boundary layers perturbed by FST. For example Hernon *et al.* (2007) showed that positive fluctuations tend to exist closer to the wall than negative fluctuations. This discrepancy with the experiment is a consequence of the simplified model. However, the areas of high- and low-velocity perturbation overlap considerably, in the wall normal direction, and this is close to observations in experiments, for example by Mandal *et al.* (2010). The solid line in figure 2.10 which shows u_1 in an area of mostly positive streak perturbation, a small negative perturbation near the wall is present, this can be contrasted to the case for longer wavelength forcing shown in figure 2.8. There the streak disturbance is simply a positive fluctuation at all y-locations. The overlapping is caused by the tilting of streamwise variations into wall-normal gradients by the mean shear, so the effect is greater for higher streamwise wavenumbers. This interesting change in the form of streamwise velocity perturbation, depending on the wavelength, indicates one of the ways that unsteadiness in the base flow could affect the stability of boundary layers perturbed by streaks.

2.2.2 Secondary stability

The secondary stability equations are derived by considering linear perturbations to the base state, equation (2.23). The streak ansatz discussed above is periodic in the streamwise and spanwise directions, as well as in time. The time dependence is eliminated by adopting a coordinate frame that translates at the Orr-Sommerfeld wave speed, which is the free-stream velocity for a continuous mode. Therefore, in terms of $x' = x - U_\infty t$, the base flow is expressed as,

$$u_2(x', y, z) = U_0(y) + A_u u_1(x', y, z), \tag{2.25}$$

and the perturbed state is,

$$\boldsymbol{v}(x', y, z, t) = \{U_0(y) + A_u u_1(x', y, z)\}\mathbf{e}_x + B\boldsymbol{v}_3(x', y, z, t), \tag{2.26}$$

where B is sufficiently small for linearisation. The secondary stability problem is derived by substituting (2.26) into the Navier-Stokes equations. Due to the linearity of u_2, terms $O(A_u^2)$ are removed and the equations satisfied by the base state u_2 are subtracted. Terms of order B^2 are neglected, and the following linear secondary stability equations are obtained in terms of vorticity,

$$\left(\frac{1}{Re}\nabla^2 - \frac{\partial}{\partial t}\right)\boldsymbol{\omega}_3 - (\boldsymbol{v}_2\cdot\nabla)\boldsymbol{\omega}_3 - (\boldsymbol{v}_3\cdot\nabla)\boldsymbol{\omega}_2 + (\boldsymbol{\omega}_2\cdot\nabla)\boldsymbol{v}_3 + (\boldsymbol{\omega}_3\cdot\nabla)\boldsymbol{v}_2 = 0. \tag{2.27}$$

where $\boldsymbol{\omega} \equiv (\xi, \eta, \zeta)^T$ is the vorticity vector. Only the u_2 component of $\boldsymbol{v}_2$ is non-zero. By analogy to the Orr-Sommerfeld and Squire primary perturbation equations, a pair of equations are derived for the secondary disturbances. The equation for $\nabla^2 v_3$ is derived by subtracting the z-derivative of the third component of (2.27) from the x-derivative of the first component. The second component leads directly to an equation for η_3. Since u_3 can not be eliminated from the secondary instability problem, the continuity equation is required in order to complete the system:

$$\begin{aligned}
&\frac{\partial^2 U_0}{\partial y^2}\frac{\partial v_3}{\partial x'} + \left(\frac{1}{R}\nabla^2 - \frac{\partial}{\partial t} - (U_0 - U_\infty)\frac{\partial}{\partial x'} - A_u u_1\frac{\partial}{\partial x'}\right)\nabla^2 v_3 \\
+\quad & A_u\Bigg(u_3\frac{\partial^3 u_1}{\partial x'^2\partial y} + v_3\frac{\partial^3 u_1}{\partial x'\partial y^2} + w_3\frac{\partial^3 u_1}{\partial x'\partial y\partial z} \\
&\quad -\left[\frac{\partial^2 u_1}{\partial y\partial z} + \frac{\partial u_1}{\partial z}\frac{\partial}{\partial y}\right]\eta_3 + \left[\frac{\partial u_3}{\partial x'} - \frac{\partial w_3}{\partial z}\right]\frac{\partial^2 u_1}{\partial x'\partial y} \\
&\quad +\left[\frac{\partial \xi_3}{\partial x'} - \frac{\partial \zeta_3}{\partial z}\right]\frac{\partial u_1}{\partial z} + \frac{\partial v_3}{\partial x'}\left[\frac{\partial^2 u_1}{\partial y^2} - \frac{\partial^2 u_1}{\partial z^2}\right] \\
&\quad +\frac{\partial v_3}{\partial z}\frac{\partial^2 u_1}{\partial x'\partial z} - \frac{\partial \xi_3}{\partial z}\frac{\partial u_1}{\partial x'} + \left[\frac{\partial u_3}{\partial z} + \frac{\partial w_3}{\partial x'}\right]\frac{\partial^2 u_1}{\partial y\partial z} - \frac{\partial \zeta_3}{\partial x'}\frac{\partial u_1}{\partial x'}\Bigg) = 0,
\end{aligned} \tag{2.28a}$$

$$\left(\frac{1}{R}\nabla^2 - \frac{\partial}{\partial t}\right)\eta_3 - \frac{\partial \eta_3}{\partial x'}(U_0 - U_\infty) - \frac{\partial v_3}{\partial z}\frac{\partial U_0}{\partial y}$$
$$+ \quad A_u\left(- \frac{\partial \eta_3}{\partial x'}u_1 - u_3\frac{\partial^2 u_1}{\partial x' \partial z} - v_3\frac{\partial^2 u_1}{\partial y \partial z} - w_3\frac{\partial^2 u_1}{\partial z^2} \right.$$
$$\left. + \frac{\partial v_3}{\partial y}\frac{\partial u_1}{\partial z} - \frac{\partial v_3}{\partial z}\frac{\partial u_1}{\partial y}\right) = 0, \tag{2.28b}$$

$$\frac{\partial u_3}{\partial x'} + \frac{\partial v_3}{\partial y} + \frac{\partial w_3}{\partial z} = 0. \tag{2.28c}$$

Homogeneous boundary conditions are enforced on u_3, v_3, w_3, and on $\partial v_3/\partial y$ at the wall and in the free stream.

2.2.3 Floquet theory

In the limit $A_u \to 0$, equations (2.28)(a and b) reduce to the classical Orr-Sommerfeld and Squire equations, and normal mode solutions can be assumed in the x, z, and t dimensions. For finite streak amplitudes, A_u, the coefficients of the secondary instability equations (2.28) remain homogeneous in time, but the coefficients u_1 are periodic in x' and z. Therefore, the normal mode assumption is not valid in those dimensions, and Floquet theory states that the solution takes the form

$$\boldsymbol{v}_3(x', y, z, t) = \tilde{\boldsymbol{v}}_3(x', y, z)\mathrm{e}^{\sigma t}\mathrm{e}^{(\gamma_x x' + \gamma_z z)}, \tag{2.29}$$

where $\tilde{\boldsymbol{v}}_3(x', y, z)$ is periodic in x' and z with the same period as the base flow,

$$\tilde{\boldsymbol{v}}_3(x', y, z) = \tilde{\boldsymbol{v}}_3\left(x' + 2\pi/k_x, y, z\right) = \tilde{\boldsymbol{v}}_3\left(x', y, z + 2\pi/k_z\right).$$

The perturbation $\tilde{\boldsymbol{v}}_3$ is therefore replaced by its Fourier representation in x' and z, and the secondary perturbation has the form,

$$\boldsymbol{v}_3(x', y, z, t) = e^{\sigma t} \sum_{n=-\infty}^{\infty} \sum_{m=-\infty}^{\infty} \boldsymbol{v}_{m,n}(y) e^{i([mk_x+\gamma_x]x'+[nk_z+\gamma_z]z)}, \tag{2.30}$$

where γ_x and γ_z have been absorbed into the summation over Fourier modes.

An eigenvalue problem is formulated by substituting (2.30) into the governing equations (2.28). The streamwise and spanwise dependent base flow serves to couple modes, $\boldsymbol{v}_{m,n}$, with those that are adjacent in discrete wavenumber space, $\boldsymbol{v}_{m\pm1,n}$, and $\boldsymbol{v}_{m,n\pm1}$. The eigenvalue problem therefore formally consists of an infinite set of coupled differential equations, but in practice a discretised and truncated set is solved.

The distinction between temporal and spatial growth concepts in the context of secondary stability framework was discussed by Herbert (1988), and is analogous to the primary instability case. In the temporal problem, σ is the complex frequency eigenvalue in the moving frame and γ_x and γ_z are real parameters. If the spatial growth were to be considered, the complex eigenvalue would be γ_x, with Real$\{\sigma\} = 0$. Since the equations are linear in σ, γ_x will appear up to the fourth order, and considerable savings in computational effort can be made by considering temporal, instead of spatial growth. The aim of the stability analysis here is to quantify the effect of introducing unsteady streaks into the boundary layer, and for example studying the effect of streak frequency and amplitude. The results are not intended to be compared to experimental measurements of the spatial growth of disturbances, therefore the temporal growth concept is considered.

Modes $\boldsymbol{v}_3$ with $\gamma_x = mk_x$, where m is an integer, are identical to a renumbering of the Fourier modes in equation (2.30). Therefore, it is sufficient to consider $|\gamma_x| \leq \frac{1}{2}k_x$. When γ_x is set to 0, the wavenumbers in the expansion (2.30) belong to the series 0, k_x, $2k_x$, ... , and

the mode is called fundamental in the streamwise direction. Alternatively, when $\gamma_x = \frac{1}{2}k_x$ the wavenumbers in the expansion belong to the series $\frac{1}{2}k_x$, $1\frac{1}{2}k_x$, $2\frac{1}{2}k_x$, ... , the mode is subharmonic in the streamwise direction. When γ_x is between these values, the mode is detuned. The same mode classifications are possible in the spanwise direction, based on the choice of γ_z.

In addition to the classification of modes as fundamental or subharmonic in the streamwise and spanwise dimensions, the spanwise symmetry of the base flow, $u_1 \sim cos(k_z z)$, means that a further distinction can be made. For a given (γ_x, γ_z) pair, the entire spectrum of eigen-solutions can be separated into two subsets: sinuous and varicose modes. The difference between the two types of solutions is clarified by considering the real form for the Fourier expansion in the spanwise direction, for example in the case of fundamental modes with $\gamma_x = \gamma_z = 0$,

$$\boldsymbol{v}_3(x', y, z, t) = e^{\sigma t} \sum_{n=-\infty}^{\infty} \sum_{m=0}^{\infty} [\boldsymbol{v}_{m,n,sin}(y) \sin(nk_z) + \boldsymbol{v}_{m,n,cos}(y) \cos(nk_z)] e^{imk_x x'}. \quad (2.31)$$

After substituting this into the stability equations (2.28), and equating terms multiplied by either $\sin(nk_z)$ or $\cos(nk_z)$, it can be shown that $u_{m,n,sin}$ modes do not couple with $u_{m,n,cos}$ modes, and the same applies for v and w. However, $u_{m,n,sin}$ modes do couple with $v_{m,n,sin}$ and $w_{m,n,cos}$ modes, and collectively these velocity perturbations are called sinuous modes due to the wavy appearance of the perturbation streamlines in a plan view. Similarly, the $u_{m,n,cos}$, $v_{m,n,cos}$ and $w_{m,n,sin}$ modes are coupled, and together they represent varicose modes. In this case, the perturbation streamlines have a periodic thickening-thinning pattern centred on each streak. These mode types are illustrated schematically in figure 2.11 for the spanwise fundamental case in panels (a) and (b).

In the case of subharmonic modes, the same mathematical distinction can be made.

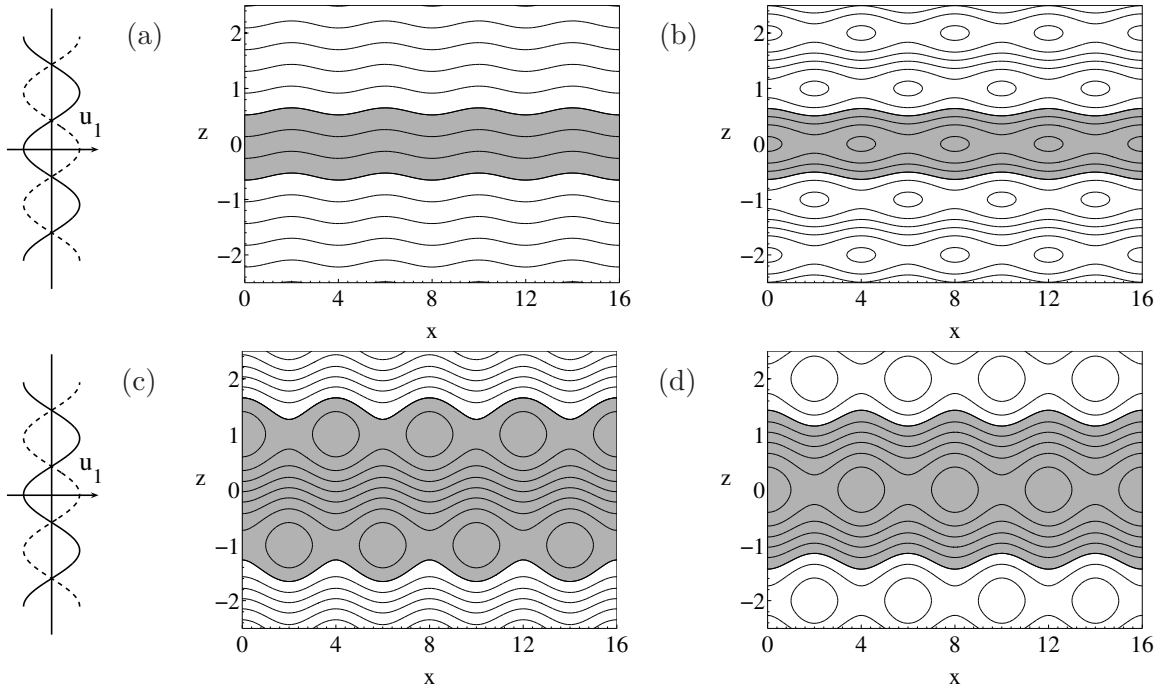

Figure 2.11: At far left, the spanwise variation of the streak amplitude is shown at two x' locations which are exactly out of phase. The four sub-plots show streamlines of the perturbation field in the $x-z$ plane for (a) the spanwise fundamental, sinuous mode; (b) the spanwise fundamental, varicose mode; (c) the spanwise subharmonic, sinuous mode; (d) the spanwise subharmonic, varicose mode. Only the first component of the spanwise Floquet expansion is shown. The spanwise wavenumber of the base flow, $k_z = \pi$ for this schematic.

However, the perturbation streamlines in plan view become less easily distinguishable as sinuous or varicose, because both types of modes exhibit ostensibly sinuous and varicose characteristics, simultaneously. In keeping with the convention in Cossu & Brandt (2004), the sinuous modes demonstrate a wavy sinuous form, centred around $z = 0$, and the varicose modes show a swelling and slimming which is centred at $z = 0$. These types of mode are shown in figure 2.11, panels (c) and (d).

The perturbation patterns in figure 2.11 exhibit a well-defined and unchanging symmetry in the case of steady base streaks with $k_x = 0$. In this case, the relationship between the stability modes and the base flow is preserved at all downstream locations since the phase of u_1 is unchanging with x' ($k_x = 0$). For example, with a negative base streak around $z = 0$

as in figure 2.11, the subharmonic sinuous modes permanently have a sinuous pattern in the neighbourhood of the negative streak, and a varicose pattern around the positive streak. In contrast, the subharmonic varicose modes permanently have a varicose pattern in the neighbourhood of the negative streak, and a sinuous pattern around the positive streak.

In the case of unsteady streaks, the fundamental perturbation patterns in figures 2.11(a) and (b) remain distinct. However, the spanwise sub-harmonic modes in 2.11(c) and (d) become physically indistinguishable because of the variation of the background streak: An originally varicose mode with respect to the solid u_1 profile is sinuous farther downstream ($x' = x'_o + \pi/k_x$), with respect to the dashed u_1 streak. Since the Floquet problem is formally an integration over all phases of the base flow, the spanwise subharmonic eigenmodes from the sinuous and varicose expansions collapse in the unsteady case. This property served as one of the validation criteria for the numerical solution of the eigenvalue problem.

Another result of the spanwise symmetry of the solutions is that the eigenvalue problems associated with the sinuous and varicose components of the expansion (2.31) can be solved independently. The eigenvalue problem is therefore split into two smaller systems which reduces the overall computational cost.

2.2.4 Numerical solution of the eigenvalue problem

The eigenvalue problem was solved numerically by discretising the wall-normal direction, accounting for a finite number of modes in the Fourier expansions, and formulating the generalised matrix eigenvalue problem,

$$\boldsymbol{A}\bar{\boldsymbol{x}} = \sigma \boldsymbol{B}\bar{\boldsymbol{x}}, \tag{2.32}$$

with σ being the complex frequency eigenvalue. Here $\bar{\boldsymbol{x}}$ is the eigenvector containing all the components of $\boldsymbol{v}_3$, with each modal component defined at all the discrete y-points. The $\boldsymbol{A}$ and $\boldsymbol{B}$ matrices represent the discretised form of the linear stability operators, including the periodic base flow. The $\boldsymbol{A}$ matrix includes all the terms which do not have time derivatives of secondary disturbance velocities, and the $\frac{\partial}{\partial t}$ terms are represented in the $\boldsymbol{B}$ matrix. The algorithm for solving the stability problem first populates the $\boldsymbol{A}$ and $\boldsymbol{B}$ matrices, and then solves the eigenvalue problem using the ARPACK library routines (Lehoucq *et al.*, 1998).

The development of the subroutines that furnish matrices $\boldsymbol{A}$ and $\boldsymbol{B}$ started with the code used by Liu *et al.* (2008*a*,*b*). In that work, a stability problem was formed for a base flow consisting of a Blasius mean flow, $U_0(y)$, plus streamwise travelling TS waves, u_{TS}, and streaks, u_k, which were periodic in the spanwise direction with finite amplitudes A and B respectively,

$$\boldsymbol{v}_2(x', y, z) = \big(U_0(y) + Bu_k(y, z) + Au_{TS}(x', y), Av_{TS}(x', y), 0\big)^T. \tag{2.33}$$

Their main goal was to find the effect of low-amplitude streaks on the secondary instability of TS waves, which is very different from the present aim of finding the secondary instability of unsteady streaks. However, because the base flow was periodic in the streamwise and spanwise directions, Floquet theory was invoked in those dimensions, and the form for the solution was similar to the present form, given in equation (2.30). There were some major differences though, between the algorithms used for solving the stability problem in Liu *et al.* (2008*a*,*b*), and accounting for unsteady streaks. For example, the underlying symmetry in the base-flow equation (2.33), allowed sinuous and varicose modes to be solved for independently, but the old algorithm did not exploit this fact. Also, the base flow with steady streaks and TS waves was actually a linear combination of base-flow terms which

were each periodic in only one direction, whereas unsteady streaks are themselves periodic in both x' and z at once. As a consequence, the functions which dealt with the coupling between terms in the solution expansion and the periodic base-flow were more complicated in the case of unsteady streaks, as described below.

The structure of the eigenvector

In order to describe the numerical technique, the structure of the eigenvector is first explained. In equations (2.28)(a, b, and c) the eigenvector appears as $(\nabla^2 v_3, \eta_3, w_3)^T$, but all these terms are composed of the primitive variables $(u_3, v_3, w_3)^T$. The choice of $\nabla^2 v_3$ and η_3 has its origin in the Orr-Sommerfeld and Squire equations, where $\nabla^2 v_3$ is completely decoupled from η_3. However, with a more complicated base flow there is no advantage to this choice of variables so, here the eigenvector is chosen to be in terms of $(u_3, v_3, w_3)^T$ because this is more straightforward to post-process.

The eigenvector $\bar{\boldsymbol{x}}$ can be broken down on three levels. The different wavenumbers of the Floquet expansion are on the top level. In the following example, which is fundamental in the x' and z directions, the Fourier series are truncated at the second harmonic:

$$\bar{\boldsymbol{x}} = (\boldsymbol{v}_{1,1}, \boldsymbol{v}_{2,1}, \boldsymbol{v}_{0,1}, \boldsymbol{v}_{1,2}, \boldsymbol{v}_{2,2}, \boldsymbol{v}_{0,2}, \boldsymbol{v}_{1,0}, \boldsymbol{v}_{2,0}, \boldsymbol{v}_{0,0})^T, \tag{2.34}$$

where the subscripts correspond to the m, n subscripts in equation (2.30). At the second level, the velocity vector $\boldsymbol{v}_{m,n}$ for each wavenumber combination contains the three (x, y, z) components of velocity,

$$\boldsymbol{v}_{m,n} = (\bar{\boldsymbol{u}}_{m,n}, \bar{\boldsymbol{v}}_{m,n}, \bar{\boldsymbol{w}}_{m,n})^T. \tag{2.35}$$

Instead of the complex Fourier series in equation (2.30), the code implements a real Fourier

expansion in terms of trigonometric functions. Therefore at the third level, each component of velocity, for each wavenumber combination, can be broken down into the Fourier terms, as follows,

$$\bar{\boldsymbol{u}}_{m,n} = (\boldsymbol{u}_{cos(mk_x),cos(nk_z)}, -\boldsymbol{u}_{sin(mk_x),cos(nk_z)}, -\boldsymbol{u}_{cos(mk_x),sin(nk_z)}, \boldsymbol{u}_{sin(mk_x),sin(nk_z)})^T. \tag{2.36}$$

The individual Fourier components $\boldsymbol{u}_{cos(mk_x),cos(nk_z)}$ are discretised using a spectral Chebyshev technique similar to that used in the solution for the initial value problem in the base-flow formulation. The vectors such as $\boldsymbol{u}_{cos(mk_x),cos(nk_z)}$ are each of size N, where N is the number of Chebyshev polynomials used in the expansion. The overall length of the eigenvector is given by,

$$M = (4N \times 3 \times N_A + 2N \times 3 \times Z_A) \times N_B + (2N \times 3 \times N_A + N \times 3 \times Z_A) \times Z_B, \tag{2.37}$$

where N_A and N_B are the number of non-zero wavenumbers included in the streamwise and spanwise Floquet expansions respectively. The parameters Z_A and Z_B depend on whether fundamental or subharmonic instabilities are sought. If the streamwise(spanwise) expansion is fundamental, then the zero wavenumber is included in the expansion and $Z_{A(B)} = 1$, otherwise, $Z_{A(B)} = 0$. The complexity of the problem clearly leads to large matrix eigenvalue problems. For example, an eigenvalue problem which is fundamental in both directions, with 5 wavenumbers included in each Fourier expansion, and 50 Chebyshev polynomials has a size $M = 18,150$.

Populating the system matrices

The column structure of the matrices $\boldsymbol{A}$ and $\boldsymbol{B}$ reflects the layout of the eigenvector, and different rows correspond to distinct equations. Individual equations are generated by grouping like terms. For example, after the Floquet form for the solution is substituted into the governing equations, every term which is multiplied by $\cos(2k_x x)\sin(3k_z z)$ appears in the '$\cos(2k_x x)\sin(3k_z z)$ equation'. The $\cos(2k_x x)\sin(3k_z z)$ term itself can be cancelled from both sides of this equation to form one row of the matrices $\boldsymbol{A}$ and $\boldsymbol{B}$. Again, the complicated sequence of the rows can be broken down on three levels, like the eigenvector. On the top level, rows are organised by the wavenumber combination, then on the second level, the three stability equations (2.28)(a, b, and c) are represented sequentially, and the final level of organisation pertains to the $\cos\,/\,\sin(mk_x), \cos\,/\,\sin(nk_z)$ nature of the periodic term being represented.

There are various ways to construct matrices $\boldsymbol{A}$ and $\boldsymbol{B}$ and one is discussed briefly here. The governing equations are linear, which means that a termwise decomposition is possible. For example if $\boldsymbol{A}_i^j$ represents the ith term in the jth stability equation, then $\boldsymbol{A} = \sum_i \sum_j \boldsymbol{A}_i^j$. The individual terms $\boldsymbol{A}_i^j$ are computed by taking each component of the solution expansion, conducting whatever differential operation the $(i,j)^{th}$ term in the equation dictates, and multiplying it with the base flow terms as necessary, and then updating the correct part of the matrices. Terms from the equation which involve the mean flow, U_0, will appear in blocks in the matrices $\boldsymbol{A}$ and $\boldsymbol{B}$ which are on the diagonal, with respect to the first level of matrix organisation. However, terms from the equation which involve u_1, will appear on off-diagonal blocks. This is because when one component of the solution expansion, with a particular wavenumber combination, say $\boldsymbol{u}_{cos(2k_x),sin(3k_z)}\cos(2k_x x)\sin(3k_z z)$ is multiplied by U_0, then the periodicity, $\cos(2k_x x)\sin(3k_z z)$, is not affected. However

if it is multiplied by u_1, the periodic component of the base flow, that product will no longer contain $\cos(2k_x x)\sin(3k_z z)$, and the $\boldsymbol{u}_{cos(2k_x),sin(3k_z)}$ terms will be shifted out of the $\cos(2k_x x)\sin(3k_z z)$ equation onto a different row. The algorithm used for solving the stability problem in Liu *et al.* (2008*a*,*b*) only implemented this shifting in either the streamwise or spanwise wavenumber because the base flow terms were individually periodic in one dimension only. However, since the base flow which consists of unsteady streaks is periodic in two dimensions, the shifting occurs both in the streamwise and spanwise wavenumbers simultaneously in the present algorithm.

2.2.5 Validation

The validation of the Floquet algorithm for the stability of periodic flows is carried by tested against results published by Herbert (1988) for the secondary stability of streamwise travelling TS waves. For calculating the secondary stability of TS waves, the base flow was changed to,

$$\boldsymbol{v}_2(x', y) = \big(U_0(y) + A\, u_{TS}(x', y), A\, v_{TS}(x', y), 0\big)^T, \tag{2.38}$$

where u_{TS} and v_{TS} were obtained from the most unstable mode of the Orr-Sommerfeld operator. This solution is a streamwise periodic, travelling TS wave. In the model assumed by Herbert (1988), the downstream growth of the mode is ignored and instead it is assigned an amplitude A. The TS wave is two-dimensional, therefore the spanwise Floquet expansion is no longer required, and a normal mode with spanwise wavenumber β is assumed,

$$\boldsymbol{v}_3(x', y, z, t) = e^{\sigma t + i\beta z} \sum_{m=-\infty}^{\infty} \boldsymbol{v}_m(y) e^{i([mk_x + \gamma_x]x')}. \tag{2.39}$$

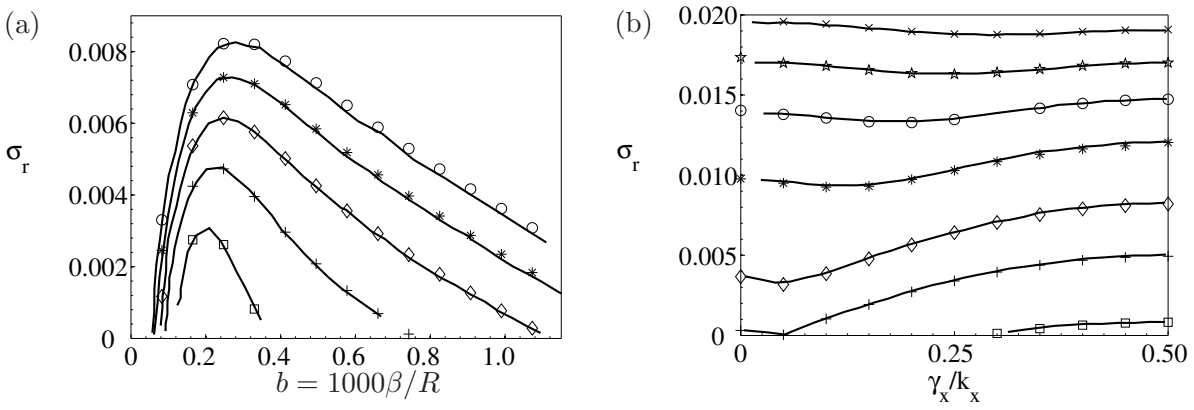

Figure 2.12: Validation case for the secondary instability of TS waves at $R_{\delta^*} = 1042$, nondimensional frequency $F = 124$. Symbols are results from the present algorithm, and lines are obtained from Herbert (1988). The growth rate of the subharmonic instability is shown versus spanwise wavenumber in (a), with TS wave amplitudes, $A = \{2, 4, 6, 8, 10\} \times 10^{-3}$. In (b), the growth rate is plotted versus the detuning factor at $\beta = 0.2$. The lines are for amplitudes, $A = \{2, 5, 10, 20, 30, 40, 50\} \times 10^{-3}$. In each figure, σ_r increases monotonically with A.

For a particular Reynolds number, $R = 606$, and normalised TS wave frequency $F = 10^6\omega_{TS}/R = 124$ (where ω_{TS} is the frequency of the TS wave), the results from the present calculations were compared to the data in Herbert (1988). In figure 2.12(a), the results for different TS wave amplitudes and spanwise wavenumbers of the subharmonic instability are presented, and the quantitative agreement is very good. A comparison for different TS wave amplitudes and values of the streamwise detune factor, γ_x, is shown in figure 2.12(b) with fundamental modes at left, and subharmonic modes at right, again the agreement between Herbert (1988) and the present results is excellent.

In order to test the implementation of spanwise-periodic terms, the results were compared the boundary-layer instabilities in the presence of steady streaks, calculated by Liu *et al.* (2008*b*). Although the main focus of that work concerned the secondary instability of TS waves, in some cases, the base flow consisted of z-periodic streaks alone,

$$\boldsymbol{v_2}(x', y, z) = \big(U_0(y) + Bu_k(y, z), 0, 0\big)^T. \tag{2.40}$$

A validation case by Liu *et al.* (2008*b*) also compared results to the instability modes reported in Cossu & Brandt (2004), in the presence of z-periodic streaks. Here the base flow was changed to steady streaks with the same parameters as Liu *et al.* (2008*b*) selected, and a normal mode with streamwise wavenumber α was assumed,

$$\boldsymbol{v}_3(x', y, z, t) = e^{\sigma t + i\alpha x} \sum_{n=-\infty}^{\infty} \boldsymbol{v}_n(y) e^{i([nk_z + \gamma_z]z)}. \tag{2.41}$$

In all cases, results from the present algorithm matched the solutions presented by Liu *et al.* (2008*b*). An additional validation of numerical algorithm with spanwise periodic terms is presented later, in section 3.4.2.

2.2.6 Resolution

For the main results presented in this chapter, the base flow consists of the doubly-periodic, streaky boundary layer, calculated as described in section 2.2.1. With this base flow, resolution tests were carried out in order to check the convergence of the Chebyshev expansion in the wall-normal direction, and the truncation level of the Floquet expansions. The wall-normal expansion converged with $N = 50$ Chebyshev modes, but the Floquet expansions required in the streamwise and spanwise directions were influenced by the base wavenumber vector of the streak, (k_x, k_z). The streaks considered here reflect the natural boundary layer conditions, and have a spanwise wavelength on the order of the boundary layer thickness, but a long streamwise wavelength $O(100\delta_{99})$. For this reason, $N_B = 2$ non-zero wavenumber modes were sufficient for the spanwise Floquet expansion, but the streamwise expansion was more challenging. Due to the low base wavenumber of the streaks, k_x, an instability with a wavenumber $mk_x \sim O(\delta_{99})$ would require the streamwise expansion to be truncated at a very high level. The data in table 2.1 demonstrates this, and shows that with $k_x = 0.0150$,

N_A	σ_r	σ_i
2	-0.0007385	0.01828
3	0.001314	0.02999
4	0.002713	0.04122
5	0.003918	0.05175
6	0.004926	0.06168
7	0.005686	0.07101

Table 2.1: The dependence of the eigenvalues σ on the number of nonzero wavenumbers in the streamwise Floquet expansion, N_A. In this case, the instability mode was fundamental in the streamwise and spanwise directions, $R = 200$, $A_u = 0.20$, $k_x = 0.0150$, $k_y = 0.6379$, and $k_z = 0.6379$.

and $A_u = 20\%$, the Floquet expansion is not converged even with $N_A = 7$ modes.

However, components of the secondary instability mode with wavenumbers pk_x, where $p \sim N_A$, can derive energy from the base flow without necessarily involving significant coupling with lower wavenumber components 0, $1k_x$, $2k_x$, ... Also, as Orszag & Patera (1983) noted, energy can be transferred directly from the mean flow to the secondary instability modes, with the periodic base flow acting only as a catalyst. This implies that for a long-wavelength base flow with a much shorter wavelength secondary instability, some small wavenumber components of the secondary mode expansion could be omitted without loss of accuracy. The results in table 2.2 support this view, and show firstly that the results with $N_A = 7$ can be calculated with the fundamental, $n = 1$ mode omitted. In this case the Floquet expansion includes a quantity of $N_A = 6$ wavenumbers, mk_x, where $m = A_{off} + (1, 2, \ldots, N_A)$, and $A_{off} = 1$. As the wavenumber offset, A_{off}, is increased and N_A is reduced, the solution is not significantly affected, down to $N_A = 4$. Also, as this truncated window of wavenumbers is moved closer to zero by reducing A_{off} but maintaining $N_A = 4$, the original data, calculated with lower N_A and no offset, are recovered. This is shown in table 2.2 where the bold text represents the original data.

Since the most unstable mode is of physical interest, the solution parameter A_{off} is

N_A	A_{off}	m-range	σ_r	σ_i
7	**0**	**[1,7]**	**0.005686**	**0.07101**
6	1	[2,7]	0.005686	0.07101
5	2	[3,7]	0.005702	0.07100
4	3	[4,7]	0.005786	0.07083
6	**0**	**[1,6]**	**0.004926**	**0.06168**
4	2	[3,6]	0.004958	0.06162
5	**0**	**[1,5]**	**0.003918**	**0.05175**
4	1	[2,5]	0.003924	0.05174

Table 2.2: The dependence of the eigenvalues σ on N_A, and the wavenumber offset, A_{off}. The parameters are the same as for table 2.1, and the bold fonts represent the original data with no wavenumber offset, duplicated for comparison.

varied until the highest growth rate is found. This process is akin to that carried out in conventional Orr-Sommerfeld studies or more recent work with embedded steady streaks, for example by Cossu & Brandt (2004), who varied the streamwise wavenumber to find the most unstable mode. The difference is that here, the periodic base flow requires the solution to be composed of a range of coupled wavenumbers as opposed to a single mode. For the streak parameters used in tables 2.1 and 2.2, the Floquet solutions were tested to ensure convergence, at the most unstable value of the offset A_{off}. In figure 2.13, the effect of varying N_A on the Floquet solution is presented and the results converge at $N_A = 4$.

2.3 Linear stability results

The solution to the numerical eigenvalue problem in equation (2.32) yields the linear instability of the Blasius boundary layer perturbed by unsteady, three-dimensional streaks. The streak amplitude and streamwise wavelength were varied in order to demonstrate the role of unsteadiness in bypass transition. The parameters of the base flow considered here are representative of the streaky boundary layer upstream of the inception of turbulent spots in simulations and experiments of transition due to free-stream turbulence. The

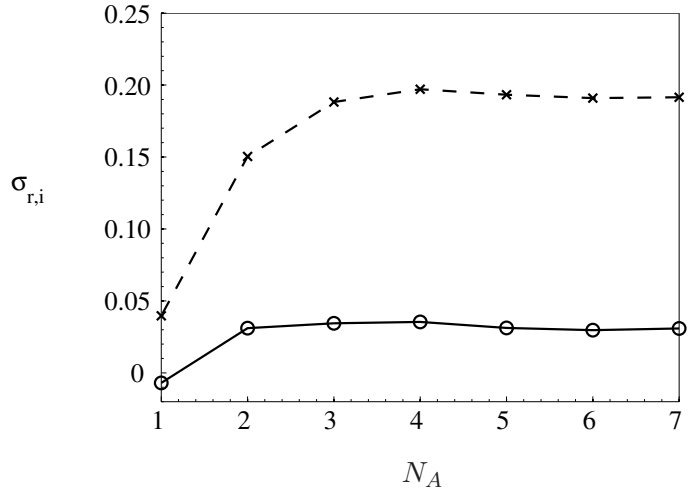

Figure 2.13: Convergence of the real part of the eigenvalue, σ_r (——); and the imaginary part, σ_i (- - -), with respect to N_A. The parameters are the same as for table 2.1, and in this case the streamwise wavenumber offset, $A_{off} = (26 - N_A)$, $N_B = 2$, and the instability was fundamental in both the streamwise and spanwise dimensions.

downstream location for the stability calculation was chosen with reference to the direct numerical simulations by Jacobs & Durbin (2001), and the Reynolds number was set at $R = 200$. In the same simulations, contours of the energy spectral density show that the boundary layer streaks have their peak energy content around the wavenumber range $k_x \in [0.003, 0.045]$, and $k_z = 0.6379$. These values are also in agreement with Matsubara & Alfredsson (2001), and are therefore selected for the range to be studied herein. Streak amplitudes, $A_u = \{5, 10, 15, 20\}\%$ are considered . This is approximately in accord with the experimental observations of Matsubara & Alfredsson (2001) and of Westin *et al.* (1994). They showed averaged perturbation levels on the order of 10%, but instantaneous fluctuations could have had larger amplitudes.

Whether the presence of unsteady streaks enhances the stability of the boundary layer is evaluated by computing the most unstable eigenmodes. For each set of streak parameters, the most unstable modes were sought amongst the whole spectrum of possible instabilities with different streamwise and spanwise detune factors, and different spanwise symmetries.

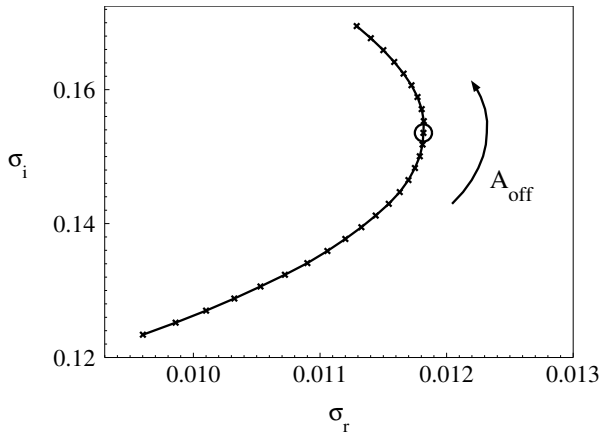

Figure 2.14: Variation of the real and imaginary parts of the eigenvalue, σ_r and σ_i with $A_{off} \in [55, 81]$. The arrow indicates the direction of increasing A_{off}, and the parameters are $R = 200$, $A_u = 15\%$, $k_x = 0.0035$, $k_y = k_z = 0.6379$. The most unstable case is marked with a circle.

Two classes of instability emerged as the most rapidly amplified, and they are discussed in the following sections. The two classes are classified based on the wall-normal distribution of energy associated with the instability, and they are denoted as the 'inner' and 'outer' modes. This terminology is also motivated by previous studies of transition in the presence of free-stream turbulence, where the onset of breakdown has been attributed to two types of instability: one class is predominantly close to the wall (Nagarajan *et al.*, 2007), and the other occurs near the edge of the boundary layer (Jacobs & Durbin, 2001; Hernon *et al.*, 2007).

2.3.1 The inner mode

The inner mode arises in the fundamental Floquet expansion for streamwise and spanwise wavenumbers, and has a varicose symmetry. Eigenvalue spectra were calculated over a broad range of A_{off} for each streak considered. This is shown in figure 2.14, where the inner mode was tracked in the complex plane as A_{off} was varied. For streaks with $A_u = 15\%$, and $k_x = 0.0035$, the inner mode is most unstable for a value of $A_{off} = 72$, marked with

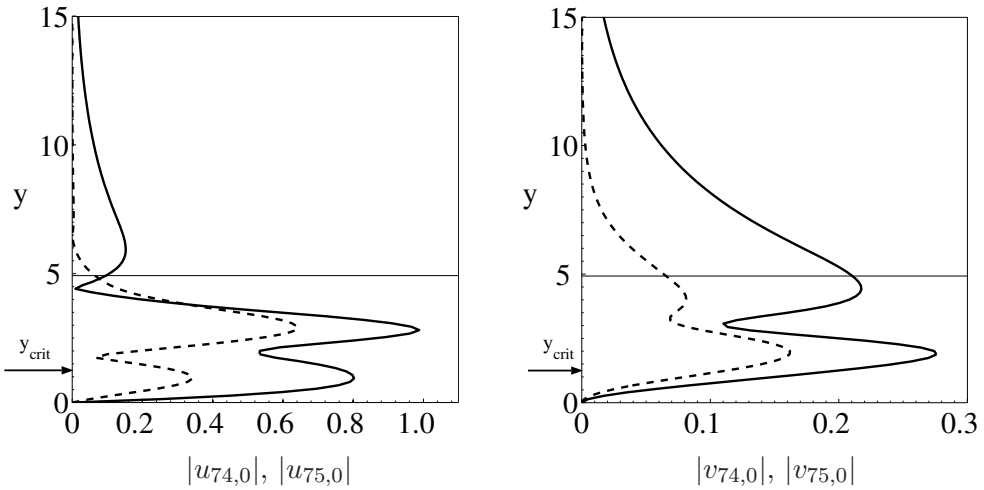

Figure 2.15: At left, the wall-normal profile for the inner mode streamwise velocity; at right, the wall-normal velocity. The parameters correspond to the most unstable case in figure 2.14. The absolute value for the most energetic (——), and second most energetic (- - -) components are plotted. These components have wavenumber vectors ($mk_x = 0.2590, nk_z = 0.0$), and ($mk_x = 0.2625, nk_z = 0.6379$), respectively. The critical layer corresponding to the most energetic mode is indicated with an arrow.

a circle. Hereafter, when the inner mode is referred to, the most unstable value of A_{off} is implied.

For the streak parameters in figure 2.14, select components of the inner mode Floquet expansion are presented in figure 2.15. The two most energetic components are plotted, and they are identified based on the maximum in the y-direction of the absolute value of the mode shapes. The critical layer for the most energetic component of the expansion is indicated in figure 2.15. It is deep inside the boundary layer at $y/\delta_{99} = 0.2524$, quite close to the wall which leads to the denomination 'inner mode'. For a TS wave the critical layer coincides with the peak in the u-mode shape, but due to the streaks the inner mode has two peaks, and the critical layer lies between them.

The streamwise velocity component with a wavenumber vector ($mk_x = 0.2590, nk_z = 0.0$) is the most energetic component in this case. The $nk_z = 0$ mode is present since the spanwise Floquet expansion for the inner mode is fundamental, and this component tends

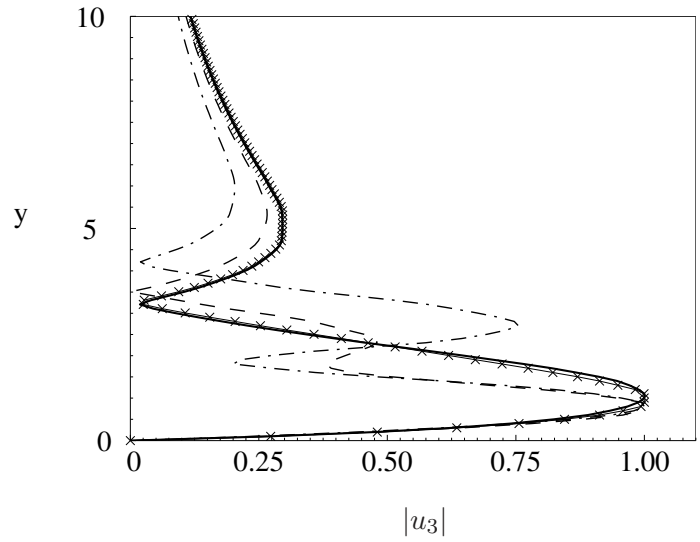

Figure 2.16: The streamwise-velocity of the inner mode, wall-normal profiles of the two-dimensional components are plotted for different streak amplitudes. $k_x = 0.0035$, $A_u = 0.0$/TS wave, (——); $A_u = 2.5\%$, (×); $A_u = 5.0\%$, (- - -); $A_u = 10.0\%$, (— · —).

to contain a good portion of the total energy. Since this component is two-dimensional, only the streamwise and wall-normal velocity fluctuations are non-zero. However, some three-dimensional elements of the solution expansion do have significant energy, due to the streaky base flow.

As the amplitude of the streaks is reduced, the two-dimensional $nk_z = 0$ components of the inner mode increasingly dominate over other parts of the expansion. In the limit $A_u \to 0$, only the two-dimensional component remains, and the inner mode assumes all the properties of a conventional TS wave. This is in line with the base flow which, in this limit consists only of the Blasius mean flow. The link to the discrete Orr-Sommerfeld mode is made evident by comparing the shape function of the TS wave to the spanwise independent component from the inner mode. Figure 2.16 illustrates that the difference between the u-perturbation profiles vanishes as the streak amplitude is reduced to zero.

Further evidence that the inner mode originates in the TS wave is presented in figure 2.17 which shows the growth rate as a function of streak amplitude. For $A_u = 0$, the

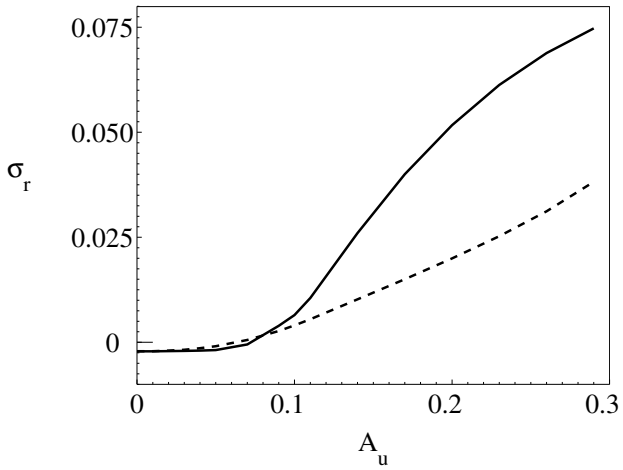

Figure 2.17: The effect of streak amplitude on the growth rate of the inner mode, σ_r. Results for two streak wavenumbers are shown: ——, $k_x = 0.030$; - - -, $k_x = 0.0035$.

growth rate is equal to that of the TS wave. As A_u is increased initially the growth rate is not significantly affected, and the denomination 'inner mode' is not necessarily warranted. However as A_u exceeds approximately 7%, the growth rate starts to increase rapidly with streak amplitude, and the inner instability mechanism takes over. In figure 2.17, the growth rate of the inner mode for two different streak wavenumbers is shown, and the shorter wavelength streak is more unstable. This suggests a possible explanation of the reason the growth rate of the inner mode contradicts the results in Cossu & Brandt (2004) which exhibit a stabilising effect of streaks on the TS wave. Their analysis assumed a steady base streak. Here it is demonstrated that unsteadiness has a destabilising effect. Therefore the disparity could be due to unsteadiness in the base flow, as conjectured in the introduction and suggested by Wu & Choudhari (2003). An alternative explanation, suggested by Cossu & Brandt (2002) is that the mean flow becomes nonlinearly disturbed by the streaks which has a stabilising influence on the TS wave, and this is addressed later in chapter 4. The effect of streak unsteadiness is investigated further in figure 2.18 where the growth rate of the inner mode is presented versus streak wavenumber, k_x, for different streak amplitudes. The influence of k_x is clear: short-wavelength streaks generally destabilise the inner mode

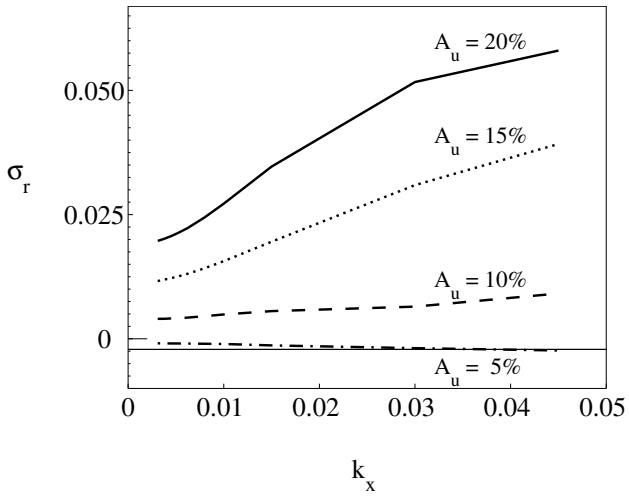

Figure 2.18: The effect of streak wavenumber on the growth rate of the inner mode, σ_r. Results for four streak amplitudes are shown: ——, $A_u = 20\%$; $\cdots$, $A_u = 15\%$; - - -, $A_u = 10\%$; — · —, $A_u = 5\%$. The thin horizontal line is the growth rate of the corresponding TS wave.

more strongly than long-wavelength ones. Though the effect is inappreciable for $A_u = 5\%$, the growth rate is significantly higher than the TS wave for $A_u \geq 10\%$, and the difference depends strongly on k_x.

For the range of streak parameters studied, the most energetic component of the Floquet expansion for the inner mode was identified, and the frequency in the stationary frame was calculated. Note that the eigenvalue, σ, is the complex frequency in the moving coordinate frame, $x' = x - U_\infty t$. However the frequency in the stationary frame, ω_m of a particular component of the Floquet expansion with streamwise wavenumber mk_x, is given by $\omega_m = \sigma_i - U_\infty m k_x$. The frequency and streamwise wavenumber of the components with the most energy are given in figures 2.19 (a) and (b) as a function of streak amplitude. In each figure, results for two streaks with different wavenumbers are presented. Below $A_u \sim 7\%$, the frequency and wavenumber are nearly constant and similar to those of the TS wave. As a result, the phase speed of the inner mode agrees closely with that of the TS wave, this is shown in figure 2.20. However, as the amplitude of the streaks is increased $A_u > 7\%$, both

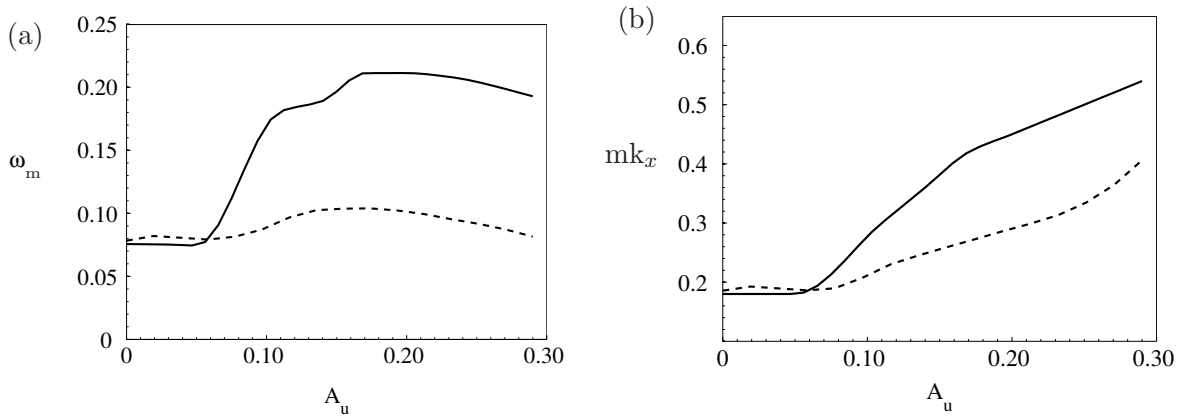

Figure 2.19: The effect of streak amplitude on the most energetic component in the Floquet expansion for the inner mode. The frequency ω_m of the inner mode, at left, and wavenumber mk_x at right. The base streak wavenumbers are $k_x = 0.0035$ (- - -) and $k_x = 0.030$ (——).

the frequency and wavenumber of the inner mode depend on the streaks, and the phase speed can reach up to $0.6U_\infty$.

The present results from linear theory are therefore in agreement with Kendall (1991) who conducted experiments with free-stream turbulence over a boundary layer and observed instabilities similar to TS waves, except that they had a higher frequency and growth rate. Bakchinov *et al.* (1995) conducted experiments with steady streaks, and used a ribbon to force near-wall instabilities at two frequencies. In light of the present results, it is not surprising that the instability in the experiments became three-dimensional, although the inner mode has a higher frequency than either of the frequencies used by Bakchinov *et al.* (1995). Also, in the higher frequency experiment only, the instability grew at a higher rate than the undisturbed TS wave in the spanwise locations of positive streak perturbations.

The influence of the spanwise wavelength of the streaks on the inner instability was investigated, but little effect was found. With a streak amplitude of $A_u = 15\%$ two streamwise wavelengths were investigated whilst varying the spanwise wavenumber in the range $k_z \in [1 \pm 0.2] \times k_{z,0}$ where $k_{z,0} = 0.6379$, which is the wavenumber used elsewhere in this

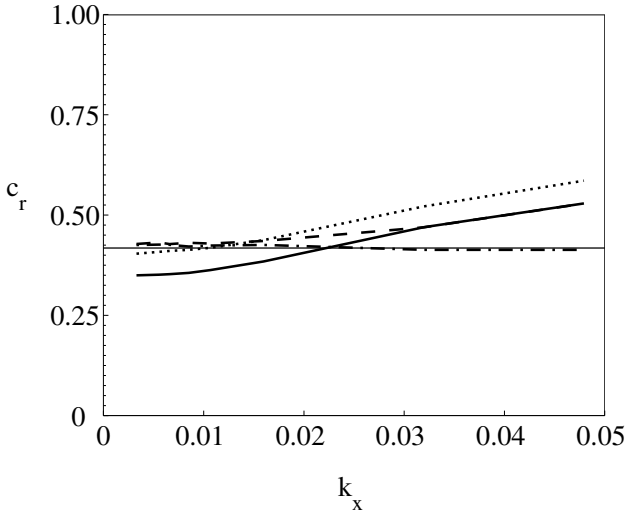

Figure 2.20: The phase speed of the inner mode versus streak wavenumber, at different streak amplitudes: ——, $A_u = 20\%$; $\cdots$, $A_u = 15\%$; - - -, $A_u = 10\%$; — · —, $A_u = 5\%$. The thin horizontal line marks the TS phase speed.

chapter. As shown in figure 2.21, over that whole range, the growth rate for streaks with $k_x = 0.0035$ increased slightly with k_z, and decreased by 7.6% with $k_x = 0.0300$. This indicates that the inner mode does not derive energy from spanwise shear in the base flow, which is in line with the well established link between varicose instabilities and the wall-normal profile of the base flow $u_2(y)$ - see for example Saric (1994). The effect of unsteadiness exhibited in figure 2.18 could therefore be due to the difference in the wall-normal streak profiles, $u_1(y)$, as k_x is changed which was illustrated in figures 2.7 to 2.10.

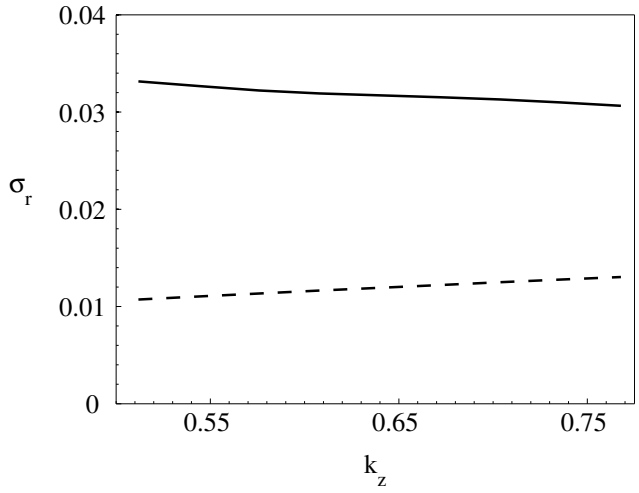

Figure 2.21: The effect of the spanwise wavenumber of the streaks on the growth rate of the inner mode. Results at $A_u = 15\%$ for two streak wavenumbers are shown: ——, $k_x = 0.030$; - - -, $k_x = 0.0035$.

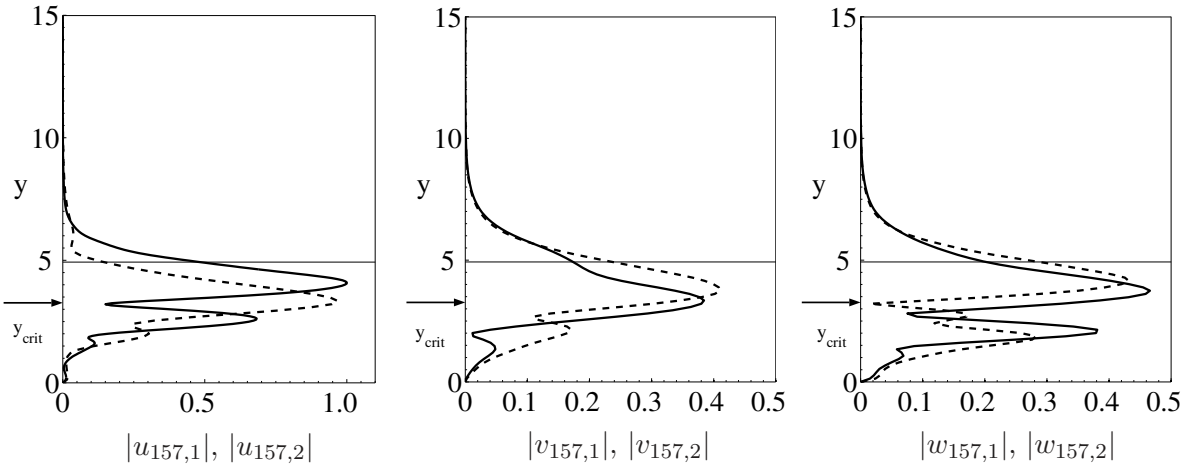

Figure 2.22: The wall-normal profile for the outer mode's velocity: at left, the streamwise velocity; in the centre, the wall-normal velocity; at right, the spanwise velocity. The parameters are $R = 200$, $A_u = 15\%$, $k_x = 0.0035$. The absolute value for the most energetic (——), and second most energetic (- - -) three dimensional components are plotted. These components have wavenumber vectors ($mk_x = 0.5495, nk_z = 0.6379$), and ($mk_x = 0.5495, nk_z = 1.2758$), respectively. The critical layer corresponding to the most energetic mode is indicated with an arrow.

2.3.2 The outer mode

In contrast to the inner mode, the outer mode is a streak instability, and it is not related to an instability of the unperturbed Blasius boundary layer. The outer mode only exists in the presence of streaks, and it appears in the fundamental expansion for streamwise wavenumbers, and the subharmonic expansion for spanwise wavenumbers. As such, the outer mode does not belong to a particular class of symmetry, owing to the underlying base flow's unsteadiness.

In the Floquet expansion for the outer mode, the modal component which generally contained the most energy was the streamwise independent term, $mk_x = 0$, and this was dominated by the streamwise velocity, u_3. For a streak with $A_u = 15\%$ and $k_x = 0.0035$, the two most energetic travelling wave components of the outer mode are presented in figure 2.22. Most of the energy in the outer mode is located high in the boundary layer,

further from the wall than in the case of the inner mode. The outer mode is so-called because its critical layer is close to the edge of the boundary layer as shown in figure 2.22, $y/\delta_{99} = 0.6626$. The mode shapes somewhat resemble those found in the experiments of Bakchinov *et al.* (1995) who studied artificially triggered streaks. In that work, two modes were found to be capable of growing: one related to the TS wave, possibly with an increased growth rate; and one caused by the spanwise shear between adjacent streaks, which had a higher phase speed and much of its energy located further away from the wall.

The frequency, ω_m and wavenumber, mk_x of the most energetic three-dimensional components of the outer mode are presented in figure 2.23, versus streak amplitude for two streak wavenumbers, $k_x = \{0.0035, 0.030\}$. Low streak amplitudes are not presented, because the outer mode requires a streaky base flow with a moderate amplitude to exist. As the streak amplitude is increased and the outer instability becomes established, the most unstable wavenumber is around $mk_x = 0.6$ for streaks with $k_x = 0.030$. This value very closely matches the wavenumber of the instability observed in the simulations of transitional boundary layers with free-stream turbulence, presented in Brandt *et al.* (2004). For streaks with $k_x = 0.0035$, the wavenumber of the outer mode is slightly smaller and therefore closer to the wavenumber of the most unstable sinuous instability, $\alpha = 0.3$, predicted by Andersson *et al.* (2001) in their inviscid analysis of steady streaks.

The frequency of the outer mode, presented in 2.23(a), is rather large. This gives rise to the high phase speed and correspondingly high critical layer. The phase speed lies in the range $c_r \sim (0.8 - 0.9)U_\infty$, as shown in figure 2.24, and depends only weakly on streak amplitude and wavenumber. This is in agreement with previous experimental and numerical studies of streak instability. For example, the experiments of Mans *et al.* (2007) and Swearingen & Blackwelder (1987), along with the DNS of Jacobs & Durbin (2001) all

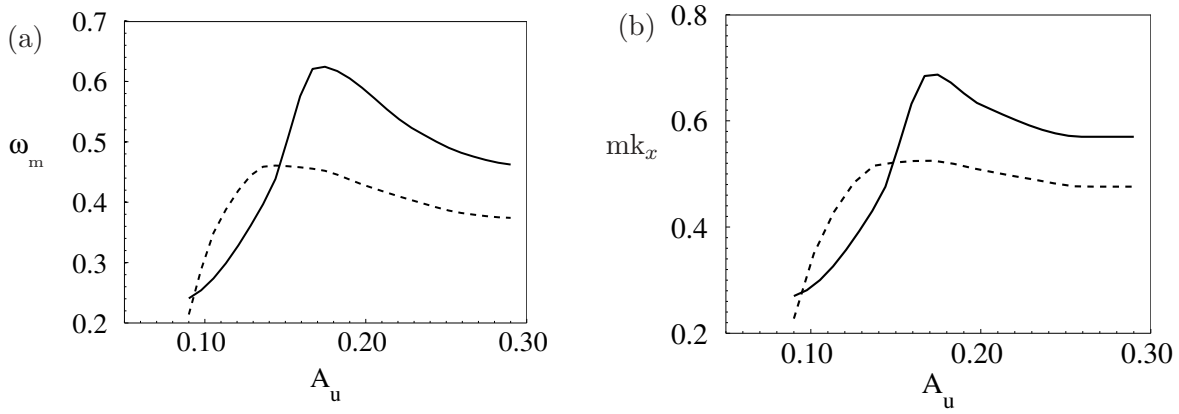

Figure 2.23: At left, the effect of streak amplitude on the frequency, ω_m of the outer mode; and at right, the effect on streamwise wavenumber, mk_x. The data correspond to the most energetic component in the Floquet expansion. The base streak wavenumbers are $k_x = 0.0035$ (- - -) and $k_x = 0.030$ (——).

reported an instability with a phase speed close to the free-stream velocity. The computed phase speed is also in agreement with the analysis of Andersson *et al.* (2001).

The growth rate of the outer mode increased with streak amplitude and wavenumber, and σ_r is plotted versus k_x in figure 2.25. For streaks with a low amplitude, $A_u = 5\%$, however, the outer mode is stable for most of the wavenumber range considered, which is in line with the notion of the outer mode as a streak instability: significant amplitude streaks are required to destabilise the outer mode. For all streak amplitudes the growth rate increased slightly with increasing streak wavenumber. In fact, streaks with $A_u = 5\%$ become slightly unstable to the outer mode for high-wavenumber streaks around $k_x > 0.02$.

The effect of spanwise wavenumber on the outer mode is, however, quite strong. Figure 2.26 shows that the growth rate increases with k_z. The growth rate was studied over the same k_z-range as the inner mode, and with $k_x = 0.030$ it increased by 116%. This implies that spanwise shear, $\partial u_2/\partial z$, between the streaks drives the outer mode and affirms the outer mode as a streak instability. It also explains why the streak amplitude is important

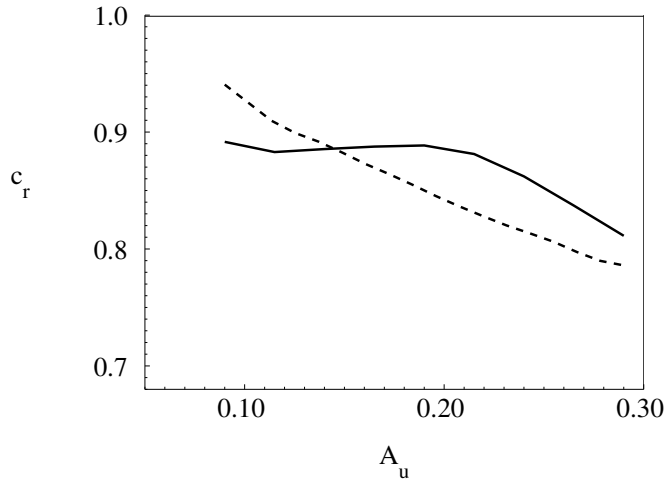

Figure 2.24: The effect of streak amplitude on the phase speed, c_r of the outer mode. The phase speed is for the most energetic component in the Floquet expansion. The base streak wavenumbers are $k_x = 0.0035$ (- - -) and $k_x = 0.030$ (——).

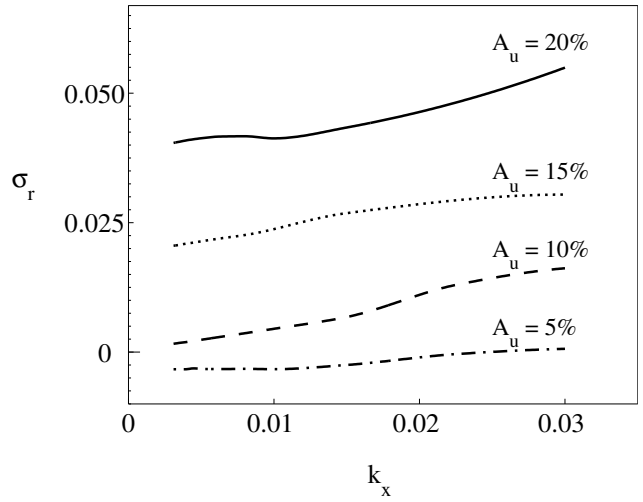

Figure 2.25: The effect of streak wavenumber and amplitude on the growth rate of the outer mode, σ_r. Results for four streak amplitudes are shown: ——, $A_u = 20\%$; $\cdots$, $A_u = 15\%$; - - -, $A_u = 10\%$; — · —, $A_u = 5\%$.

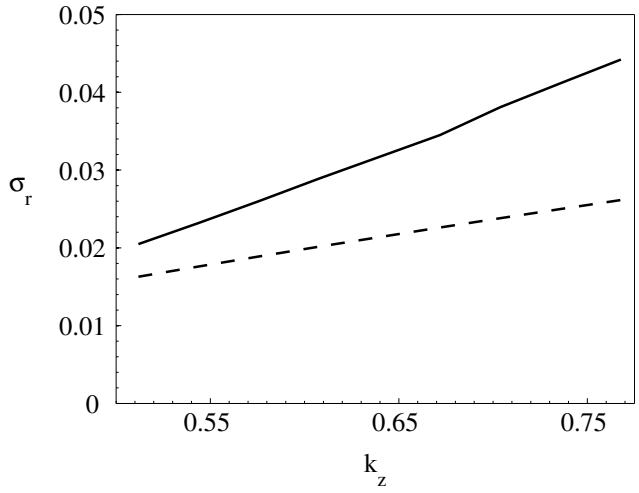

Figure 2.26: The effect of the spanwise wavenumber of the streaks on the growth rate of the outer mode. Results at $A_u = 15\%$ for two streak wavenumbers are shown: ——, $k_x = 0.030$; - - -, $k_x = 0.0035$.

($\partial u_2/\partial z \propto k_z A_u$), but the effect of the streamwise wavenumber, k_x, shown in figure 2.25, is weaker than in the case of the inner mode which is associated with the wall normal base flow profile.

To draw out the effect of unsteadiness, the critical streak amplitude for the outer mode to become unstable is presented versus streak wavenumber in figure 2.27. The results show that unsteady streaks become unstable at a critical amplitude $A_u \sim 5 - 8\%$, and increasing the unsteadiness of the base flow reduces the critical A_u. The critical amplitude is lower than that calculated by Andersson *et al.* (2001) for steady optimal streaks, and the difference is due to the base flow anatz. Since the outer mode is essentially a streak instability, the effect of nonlinear mean flow modifications, which are taken into account in their analysis, is not expected to play a role. Instead the major difference is that the present analysis is for unsteady streaks. As in the case of the inner mode, this explanation for the difference between the current results and previous analyses, is also supported by the destabilising effect of increasing the wavenumber, which is evident in figure 2.27.

The critical streak amplitude calculated here compares more closely to experimental

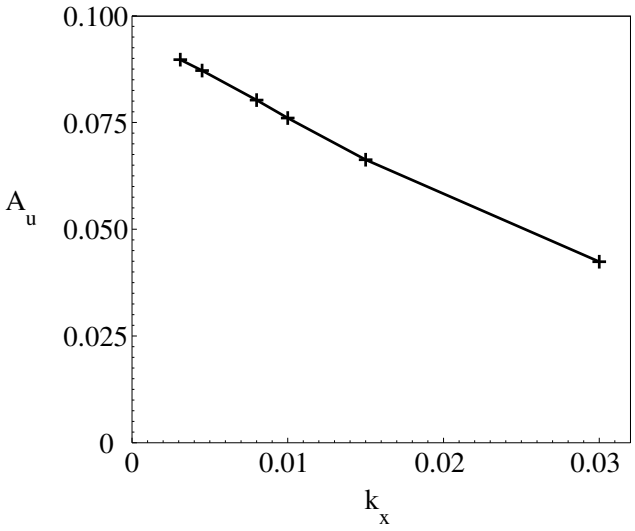

Figure 2.27: Dependence of the critical streak amplitude, A_u, for the outer instability on the streamwise wavenumber of the streak.

observations than the previous analysis by Andersson *et al.* (2001). For instance Kendall (1990) reported Klebanoff modes of amplitude $u_{rms} = 5 - 10\%$ upstream of boundary layer transition, and all the references outlined in Westin *et al.* (1994) indicate conditions in the range $u_{rms} \in [5, 11]\%$ at the onset of transition. In experiments, the boundary layer would naturally be exposed to broadband free-stream disturbances which leads to streaks with significant energy in the unsteady components, previously overlooked by analyses of steady streaks.

The current results are also in agreement with simulations of transition in the presence of FST. For example, DNS of Jacobs & Durbin (2001) and Brandt *et al.* (2004) both reported streak amplitudes around $u_{rms} = 10\%$ upstream of transition. Although the averaged data from these experiments and simulations could conceal localised perturbations somewhat closer in amplitude to the critical level predicted by Andersson *et al.* (2001), the latter simulations were at odds with previous analyses of steady streaks in another respect. Brandt *et al.* (2004) noted an almost equal number of sinuous and varicose instabilities in their simulations, whereas Andersson *et al.* (2001) predicted a dominantly sinuous instability. The

observations of Brandt *et al.* (2004) can be explained in the light of the present unsteady analysis. Due to the spanwise subharmonic nature of the outer mode, it encompasses perturbation patterns that can appear either sinuous or varicose, depending on the local phase of the base streak.

In contrast to the DNS by Jacobs & Durbin (2001) and Brandt *et al.* (2004), the following section describes simulations performed in a more controlled environment. The streaks are generated by a single vortical mode at the inlet with specific parameters, as opposed to a broad spectrum. In the simulations, the inner or outer mode is also applied at the inlet. By varying the amplitude and wavenumber of the streak, the effect of these parameters on the nonlinear evolution of the inner and outer instabilities is studied.

2.4 Direct numerical simulations

This section reports on DNS of the inner and outer instabilities in a flat-plate boundary layer distorted by streaks. In the simulations, the laminar streaky boundary layer was observed to break down to turbulence after the amplification of the inner or outer instability. The dependence of both instabilities on the streak amplitude and frequency is investigated in order to verify whether the results of linear theory are observable in the non-linear problem.

The three-dimensional, incompressible Navier–Stokes equations are solved using the numerical algorithm described in Rosenfeld *et al.* (1991). It should be noted that all direct simulations reported in this thesis were conducted with assistance from other members of the group, for which the author is very grateful. The method is a fractional step formulation where the convective terms are treated explicitly using Adams–Bashforth time advancement; the diffusion and pressure terms are advanced by Crank–Nicolson and implicit Euler schemes, respectively. The spatial discretisation is based on local volume fluxes

on a staggered computational grid.

In terms of Reynolds number, the computational domain spans $200 \leq R \leq 640$. The inflow plane is therefore upstream of the critical Reynolds number for the first unstable TS wave. While the exit plane is downstream of the critical R, it is well upstream of the location where the orderly transition process would be complete, $R \sim 5,000$. The length scale used in the DNS is the 99% thickness of the boundary layer at the inlet to the domain, δ_0, and the size of the computational domain is $360 \times 20 \times 12$, in the streamwise, wall-normal, and spanwise directions, respectively. The computational domain contains six spanwise wavelengths of the streak, therefore six full wavelengths of the inner mode are represented, and three for the outer mode. Simulating turbulent flow with high fidelity is not the aim of the simulations, and the domain is is considered sufficient to capture the early growth of the instabilities.

The grid resolution was finer than the recommended values in Jacobs & Durbin (2001), who performed an extensive grid refinement study. A total of 14 million points were used in order to accurately capture the amplification of the secondary instabilities of the streaky boundary layer and non-linear breakdown to turbulence.

A free-slip boundary condition is applied on the top boundary of the computational domain which is contoured in order to ensure zero-pressure-gradient in the downstream direction. The distance between the wall and the top boundary increases downstream direction from the inlet by the same amount that the boundary layer displacement thickness increases. At the bottom wall, a no-slip boundary condition is enforced , and a convective outflow condition is applied at the exit plane. At the inlet to the simulation domain, in addition to the Blasius profile, two perturbations are prescribed. The first is a continuous

Orr-Sommerfeld mode v_1 which gives rise to boundary layer streaks via the *lift up*, or vorticity tilting, mechanism. The parameters of the Orr-Sommerfeld mode, therefore, determine the spanwise spacing, frequency, and intensity of the streaks. The second disturbance is an inner or outer instability mode obtained from the Floquet analysis. The inflow condition is therefore,

$$\begin{aligned} \boldsymbol{v}_0(y,z,t) = \boldsymbol{v}_B(y) &+ A_v \text{Real}\left\{\cos(k_z z)\hat{u}_1(y)e^{i(-\omega t)}\right\}\mathbf{e}_x \\ &+ A_v \text{Real}\left\{\cos(k_z z)\hat{v}_1(y)e^{i(-\omega t)}\right\}\mathbf{e}_y \\ &- A_v \text{Imag.}\left\{\sin(k_z z)\hat{w}_1(y)e^{i(-\omega t)}\right\}\mathbf{e}_z \\ &+ A_s \sum_n \sum_m \text{Real}\left\{\boldsymbol{v}_{m,n}(y)e^{i([nk_z+\gamma_z]z-\omega_m t)}\right\}, \end{aligned} \tag{2.42}$$

where $\boldsymbol{v}_B$ is the Blasius flow, $\hat{\boldsymbol{v}}_1$ is the forcing Orr-Sommerfeld mode, and ω_m is the frequency of each component of the streamwise Floquet expansion of the instability wave. The parameters A_v and A_s are the amplitudes of the continuous Orr-Sommerfeld mode and the secondary instability, respectively.

2.4.1 The inlet Orr-Sommerfeld mode and boundary layer streaks

In the simulations, the amplifying boundary layer streaks were generated in response to inlet forcing by the continuous Orr-Sommerfeld mode. The streak intensity was dictated by the amplitude A_v and wavenumber of the Orr-Sommerfeld mode. The wall-normal and spanwise wave-numbers were $k_y\delta_0 = \pi$ and $k_z\delta_0 = \pi$. The latter corresponds to a streak spanwise spacing on the order of the boundary layer thickness. Two low-frequency continuous modes were selected, $\omega^1 = 0.0304$ and $\omega^2 = 0.0491$ (in terms of δ_0), because they stimulate streaks more effectively than high-frequency forcing. Each was independently prescribed at the inlet of the domain in order to induce boundary-layer streaks at their respective frequencies.

An investigation of the role of streak intensity on stability was easily achieved by changing the amplitude of the inlet Orr-Sommerfeld mode, A_v, while holding its frequency constant. On the other hand, an assessment of the influence of streak unsteadiness was less straightforward. Changing the frequency of the inlet Orr-Sommerfeld mode also changed the streak amplitude, because, for example, high frequency Orr-Sommerfeld modes at the inlet penetrate the boundary layer less than low frequency modes and therefore stimulate the streaks downstream less. Therefore, a calibration of the inlet A_v was required in order to ensure that both inlet frequencies of the Orr-Sommerfeld disturbance yielded the same streak intensity downstream. For the lower frequency mode, an inlet amplitude $A_v = 2.5\%$ led to a maximum streak strength $u_{rms} \sim 19\%$. The same streak intensity required a larger inlet amplitude, $A_v = 3.5\%$, for the higher frequency Orr-Sommerfeld mode. The larger A_v is consistent with previous work on the coupling between the Orr-Sommerfeld forcing and the Squire, or streak, response (Zaki & Durbin, 2005). Indeed, solutions of the IVP were used to guide the choice of inlet amplitude when trying to achieve a particular target amplitude, although ultimately A_v was adjusted through trial and error.

When the Orr-Sommerfeld continuous mode was prescribed alone at the inlet of the domain, the amplification of the boundary layer streaks was followed by viscous decay. The downstream evolution of the streak amplitude agreed qualitatively with the behaviour of the solution to the initial value problem in section 2.2.1. In all the simulations with only an Orr-Sommerfeld inlet perturbation, the boundary layer remained laminar.

When the secondary instability mode, be it of the inner or outer type, was also included at the inlet plane along with the Orr-Sommerfeld mode, breakdown of the streaky boundary layer was observed within the computational domain. These simulations are discussed in sections 2.4.2 and 2.4.3 for the inner and outer instabilities, respectively. The current

simulations of modal interactions bear similarity to the DNS of Zaki & Durbin (2005, 2006). They simulated pairs of continuous Orr-Sommerfeld modes: a low-frequency and a high-frequency pair. The low-frequency disturbance lead to the generation of streaks. The high-frequency pair did not penetrate the boundary layer due to shear sheltering. Instead, the high frequency modes interact with the lifted streaks in the free stream causing breakdown to turbulence. It is therefore possible that the instability mechanism in those simulations is related to an "outer" mode. However, the high-frequency component in that work was not, formally, an instability of the base flow in the sense of linear stability analysis.

The inner and outer modes studied were calculated from the temporal Floquet analysis, at a Reynolds number downstream of the inlet plane in the DNS, therefore the simulations represent a somewhat *ad hoc* approach. However, the emphasis here is on gaining an empirical view of the inner and outer instabilities in a flat-plate boundary layer. For instance, the streak amplitude in the DNS is a function of the streamwise coordinate, and therefore comparing the growth rates of the inner- and outer-modes from the simulations and the Floquet analysis would not be very instructive. Instead, changes in the location of transition onset are regarded as indicative of the variation of the growth rate of the secondary instability.

2.4.2 The inner mode

With both the continuous Orr-Sommerfeld mode and the inner instability superposed at the inlet, transition to turbulence was possible within the computational domain. In all the simulations, the amplitude of the inner instability mode at the inlet was maintained at $A_s = 1.5\%$. The time-averaged skin friction coefficient C_f is plotted in figure 2.28 for the reference simulation, in which the inlet Orr-Sommerfeld mode parameters are $\omega^1 = 0.0304$

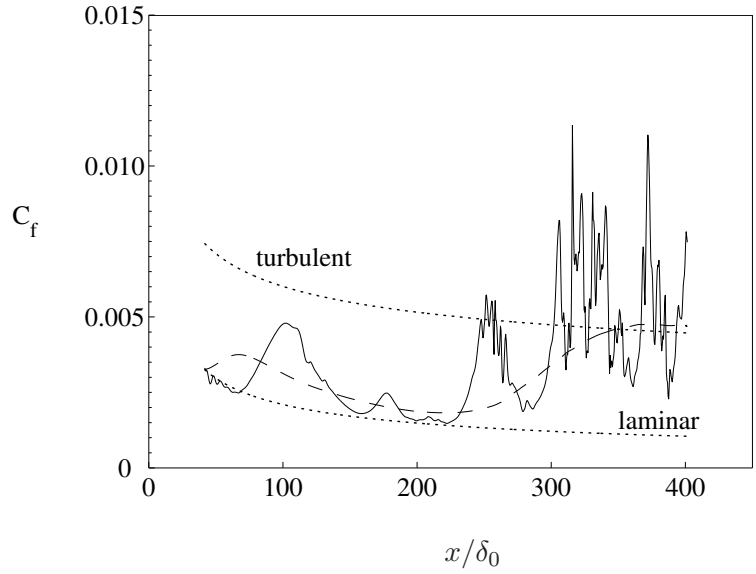

Figure 2.28: Instantaneous (——) and time averaged (- - -) skin friction profiles from DNS of the inner instability in which the inlet Orr-Sommerfeld mode parameters are $\omega^1 = 0.0304$ and $A_v = 2.5\%$.

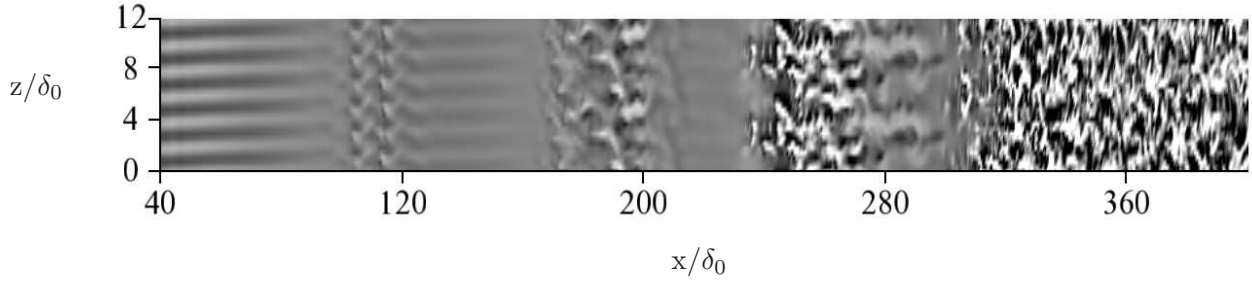

Figure 2.29: Contours of the $v-$perturbation velocity ($-0.05 \leq v \leq 0.05$), at the same time instant as figure 2.28. The plane is $y/\delta_x = 0.5$, where δ_x is the boundary layer thickness at the location of the turbulent patch. Light and dark contours mark positive and negative velocity perturbations, respectively.

and $A_v = 2.5\%$. The initial increase in the skin friction is due to the development of streaks. Theoretical skin friction curves for developed laminar and turbulent flow are also plotted in the figure, they come from the Blasius solution and the turbulent correlation $C_f = 0.455/(log(0.06R_x))^2$. Transition from the laminar to turbulent skin-friction level is evident. An instantaneous skin friction curve is also included, and it illustrates the intermittent nature of the transition region.

A top view of the $v-$perturbation field inside the boundary layer is shown in figure 2.29. Light and dark contours mark positive and negative velocity perturbations, respectively, and this is the case for all subsequent DNS figures in this thesis. The time instance corresponds to the instantaneous C_f curve in figure 2.28. The top view shows the upstream laminar flow, a turbulent patch in the transition region, and the fully-turbulent boundary layer near the exit of the domain. In the transition region, the turbulent patch has a spanwise homogeneous appearance in contrast to the more sporadic turbulent spots which are triggered in bypass transition of boundary layers (Jacobs & Durbin, 1998; Nagarajan *et al.*, 2007). Unlike the random forcing of the streaks in the bypass problem, the inlet forcing in the present controlled simulations is via the inner mode. As a result, the instability which precedes breakdown develops periodically across the spanwise extent of the domain.

The dependence of breakdown location on the intensity of the streaks was investigated by varying the inlet amplitude of the lower-frequency continuous Orr-Sommerfeld mode, $\omega^1 = 0.03$. Three values of $A_v = \{2.0, 2.5, 3.0\}\%$ were simulated. The maximum resulting streak amplitudes were $u_{rms} = \{17.2, 19.4, 21.4\}\%$, respectively. At the lowest amplitude, transition was not observed within the computational domain. However, as the streak intensity increased, transition moved upstream (table 2.3). This is in agreement with the results of the linear Floquet analysis where the growth rate of the inner instability increased

ω	$A_v(\%)$	$\max(u_{rms})(\%)$	Transition Re_x ($\times 10^{-5}$)	
			Start	End
0.03	2.0	17.2	—	—
0.03	2.5	19.4	2.20	3.65
0.03	3.0	21.4	1.33	3.20
0.05	3.5	19.7	1.32	2.45

Table 2.3: Transition location in DNS of the inner instability.

with streak amplitude. These findings are also in agreement with previous studies such as Boiko *et al.* (1994), who show that transition via TS-type waves growth can be promoted by streaky disturbances inside the boundary layer.

The dependence of transition location on the streak unsteadiness was evaluated by changing the inlet Orr-Sommerfeld mode frequency. The inlet Orr-Sommerfeld amplitude, A_v, was adjusted in order to ensure equal maximum streak amplitudes. Breakdown of the boundary layer took place significantly earlier upstream in the case of the higher-frequency streaks (see table 2.3). The dependence on streak frequency is also in agreement with the prediction of linear theory. The Floquet analysis indicated that the growth rate of the inner mode instability increases nearly linearly with k_x of the streaks for $A_u \geq 15\%$ (figure 2.17).

2.4.3 The outer mode

Direct numerical simulations were carried out with both the low-frequency Orr-Sommerfeld mode and an outer instability prescribed at the inlet of the computational domain. The amplitude of the outer mode was fixed at $A_s = 1.0\%$. This value was required in order to provoke transition at Reynolds numbers comparable to those of the inner mode. Transition to turbulence took place in all the DNS, even at streak amplitudes as low as $u_{rms} = 17.2\%$. This amplitude is significantly lower than the threshold for instability predicted by the

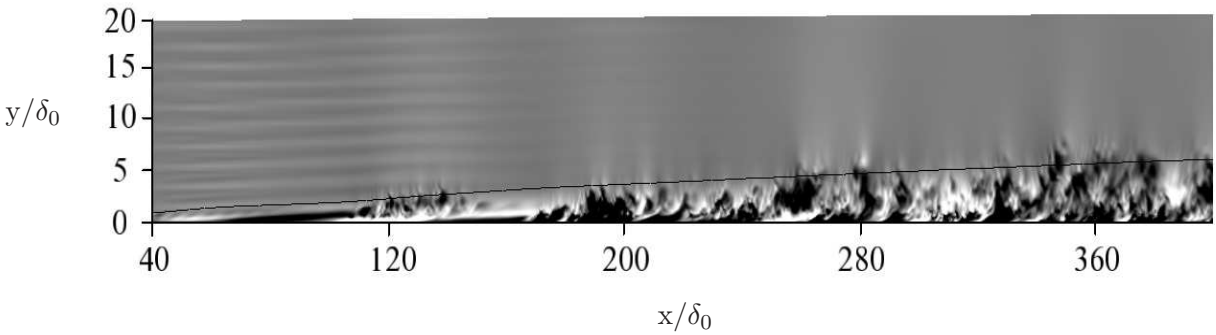

Figure 2.30: Contours of the instantaneous $u-$perturbation field in the (x,y)–plane ($-0.1 \leq u \leq 0.1$). The side view shows the laminar, transitional, and fully turbulent regions of the boundary layer.

steady analysis of Andersson *et al.* (2001). The simulations are therefore indicative of the significance of streak unsteadiness on the stability of the boundary layer.

A side view of the entire streamwise extent of the computational domain is shown in figure 2.30. The contours of instantaneous $u-$perturbations illustrate the laminar, transitional, and turbulent regions of the flow. At a moderate amplitude of the inlet Orr-Sommerfeld mode, $A_v = 2.5\%$, transition due to the outer instability (figure 2.30) is complete farther upstream in comparison to the case of the inner mode (figure 2.29).

The effects of streak intensity and frequency on the outer-instability and, in turn, on transition location were evaluated using DNS. The results of the simulations are summarised in table 2.4. Increasing the amplitude or frequency of the streaks caused early transition. However, the effect of altering the intensity of the streaks is much more significant than changing their frequency - this is consistent with the results of the Floquet analysis (figure 2.25).

The results from this chapter have shown that boundary layers with unsteady streaks calculated from the linear initial value problem were potentially unstable to two modes of instability: the inner mode and outer mode. The inner mode was related to the TS wave, but unsteady linear streaks increased the growth rate significantly. This could shed light

ω	$A_v(\%)$	$\max(u_{rms})(\%)$	Transition Re_x ($\times 10^{-5}$)	
			Start	End
0.03	2.0	17.2	1.55	4.00
0.03	2.5	19.4	1.07	2.70
0.03	3.0	21.4	0.925	2.60
0.05	3.5	19.7	1.07	2.45

Table 2.4: Transition location in DNS of the outer instability.

on the breakdown mechanism observed by Nagarajan *et al.* (2007) in their simulations of bypass transition with a leading edge. Also, if the amplitude of the streaks exceeded a critical amplitude, the flow became unstable to the outer mode. The amplitude required for the streak instability was lower than previously calculated in an analysis with steady, nonlinear streaks (Andersson *et al.*, 2001).

The results from the present chapter agreed more closely than previous analyses with many experiments and simulations from the literature, and the improvement could be explained by the base flow. The streak ansatz employed was different from prior studies in the literature in a variety of ways, for example the initial conditions represented a Fourier component of the unsteady free-stream turbulence and its signature in the boundary layer. The fact that the growth rate of the inner and outer modes increased with k_x suggested specifically that it was unsteadiness in the base flow that triggered the inner mode, and led to a streak instability with a comparatively low critical amplitude. However, the mechanism by which unsteadiness affected the system was not made clear, for instance changing k_x simultaneously altered both the streamwise dependence of the base flow, and the wall-normal shape of the streak profile.

The discrepancy between the present results and previous analyses could also be due to neglecting nonparallel and nonlinear effects in calculating the base flow. The nonlinear

exchange of energy from the streaks to the mean flow leads to a distorted U_0 which has a fuller shape than the Blasius profile. This distorted mean-flow was reported by Cossu & Brandt (2002) to have a stabilising influence on TS waves. Since the base flow in section 2.2.1 did not account for this effect, it could bear on the inner mode results, which exhibit the generally destabilising impact of linear streaks. In the subsequent chapters, nonlinear streaks are calculated and used as a base flow for the stability analysis.

Chapter 3

Nonlinear base flow and stability formulation

3.1 Introduction

The preceding chapter demonstrated the difference between the stability characteristics of an undisturbed boundary layer and boundary layers distorted by streaks. The results emphasised the influence of choosing a particular model for the streaky base flow, and the effect of unsteadiness was shown to have a significant impact on the instability modes. In this and the following chapter, a more accurate model for the streaks is established. This allows the roles played by unsteadiness and nonlinearity of the base flow in boundary layer instability to be studied in detail.

The Klebanoff distortions considered here have a low streamwise wavenumber and the boundary layer grows significantly over one wavelength, therefore nonparallel effects could play a role in their development. With the method described in section 2.2.1 however, they were neglected, and this could impact on the stability results. Also, naturally occurring streaks reach amplitudes where nonlinearity could be important. In the case of streak instabilities, Andersson *et al.* (2001) made a direct comparison between results from two stability analyses. The first employed the so-called 'shape assumption' in which the base

flow was calculated from linearised equations, and the second used streaks calculated from the fully nonlinear equations. The outcome showed that the nonlinearity had an effect on the instability, albeit at high streak amplitudes of approximately 40%.

In the following chapters an analysis of the stability of boundary layers distorted by unsteady streaks is conducted, with a more accurate ansatz for the base flow. Nonlinear and nonparallel effects are taken into account. Direct numerical simulations are used to calculate the streamwise evolution of a boundary layer, perturbed at the inlet plane by a vortical free-stream mode. Like the previous stability analysis, a particular downstream location is selected, and the stability analysis is carried out at that Reynolds number. Due to the downstream growth of the boundary layer, the streamwise dependence of the base flow is not periodic, and a Floquet expansion in the streamwise direction is no longer used. This can be justified by the results in chapter 2 which show that, in spite of the obvious influence of unsteadiness, the streamwise wavenumber of the instability is smaller than the streaks. The base flow calculated at a particular cross-stream plane in the DNS is unsteady, and this is accounted for in the stability analysis with a time-periodic base flow, and Floquet theory is invoked in time. Similar to the previous chapter, the streaks are also periodic in the span, and a Floquet expansion is used in this dimension. However, since the base flow calculations are nonlinear, the base state is composed of multiple spanwise wavenumbers.

In this chapter the DNS used to calculate the nonlinear streaky boundary layer are described, and the base flow used for the stability analysis is illustrated. Then the formulation of the stability problem for the time-periodic base flow is given. Finally a validation case for the new implementation of the Floquet algorithm is presented, specifically, the time dependent and nonlinear aspects are addressed.

3.2 Non-linear base flow

Direct numerical simulations of the Navier-Stokes equations are performed with an inflow condition consisting of a superposition of the Blasius profile and a perturbation which triggered the streaks. The three-dimensional, incompressible Navier–Stokes equations are solved using the numerical algorithm described chapter 2. The flow parameters of the simulations were chosen to match the DNS of bypass transition by Jacobs & Durbin (2001). In those simulations, the inlet plane corresponded to $R = 163$, and the streaks grew downstream before the onset of secondary instability around $350 < R < 400$. The spanwise correlation of streamwise disturbance velocity inside the boundary layer indicated a spacing of approximately $0.6\delta_{99}$ between the high and low speed regions of the streaks. Disturbance energy spectra at the onset of transition concurred with the correlation and showed that most of the energy content was in the wavenumber range $0.5 \leq k_z \leq 1.0$, and the nondimensional frequency range $F < 100$.

In the present simulations, the inlet plane is at the same Reynolds number as in the DNS of Jacobs & Durbin (2001), and the inflow was formed of the Blasius flow, $\boldsymbol{v}_B$, and a three-dimensional free-stream vortical mode, $\boldsymbol{v}_1$:

$$\begin{aligned} \boldsymbol{v}_0(y,z,t) = \boldsymbol{v}_B(y) \quad &+ \quad A_v \mathrm{Real}\left\{\cos(k_z z)\hat{u}_1(y)e^{i(-\omega t)}\right\}\mathbf{e}_x \\ &+ \quad A_v \mathrm{Real}\left\{\cos(k_z z)\hat{v}_1(y)e^{i(-\omega t)}\right\}\mathbf{e}_y \\ &- \quad A_v \mathrm{Imag.}\left\{\sin(k_z z)\hat{w}_1(y)e^{i(-\omega t)}\right\}\mathbf{e}_z. \end{aligned}$$

Streaks developed downstream, and reached their maximum amplitude near the location of transition onset reported in the previous simulations of bypass transition. The streamwise location selected for the stability calculations was $R = 360$. The local streak wavenumber

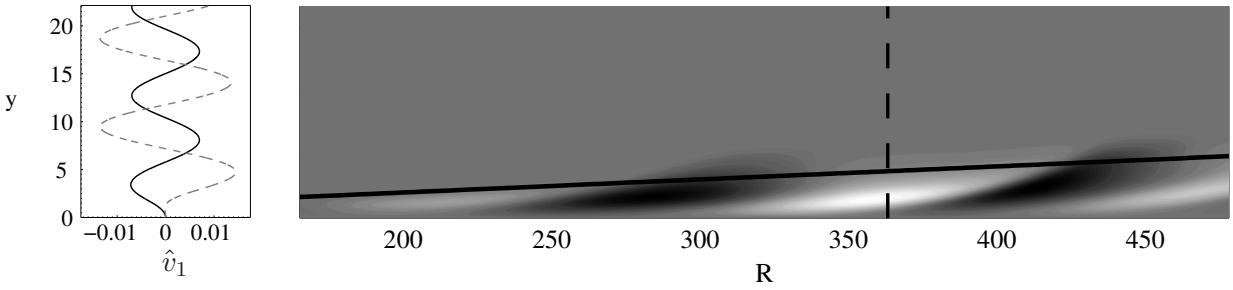

Figure 3.1: The boundary layer response to forcing by a single, unsteady free-stream vortical mode, $F = 60$. The figure at left shows the v component of the free-stream forcing mode; the figure at right a side view of the u-perturbation field, $-0.20 < u_1 < 0.20$. The $y-$coordinate is normalised by the Blasius length scale at the target Reynolds number, $R = 360$, where the stability analyses are carried out. This location is marked by the dashed line.

was selected to be $k_z = 0.71$ ($\lambda_z = 8.9$), nondimensionalised by the local Blasius length scale. The range of frequencies, ω, was chosen to be $F = 10^6 \text{Real}\{\omega\}/R \in [0, 60]$. The amplitudes, A_v, of the free-stream vortical mode were selected to give rise to streaks with amplitudes $\{5, 10, 15, 20\}\%$ at the streamwise position $R = 360$. The linear IVP was used to help choose the values of A_v in order to achieve the desired amplitudes. In some cases however, a trial and error method was used to get the streak amplitudes within 10% of the desired amplitude, then the streak was simply scaled to the correct amplitude. An example simulation is presented in figure 3.1. At left, the wall-normal component of the forcing is shown, nondimensionalised by the Blasius lengthscale at $R = 360$. At right, contours of the streamwise velocity perturbation are shown in a side view. The edge of the boundary layer is marked with a black line. The downstream amplification of the unsteady streak can be contrasted to the linear calculations shown in figures 2.7 and 2.9.

To build up a database of streaky base flows, separate DNS were conducted whilst varying ω, and A_v. Since the streaks evolved nonlinearly, their amplitude could not be simply scaled as in the equation (2.23) for linear streaks. Instead the strength of the inlet perturbation, A_v, was tuned in the range $(0.27, 1.08)\%$ to control the downstream

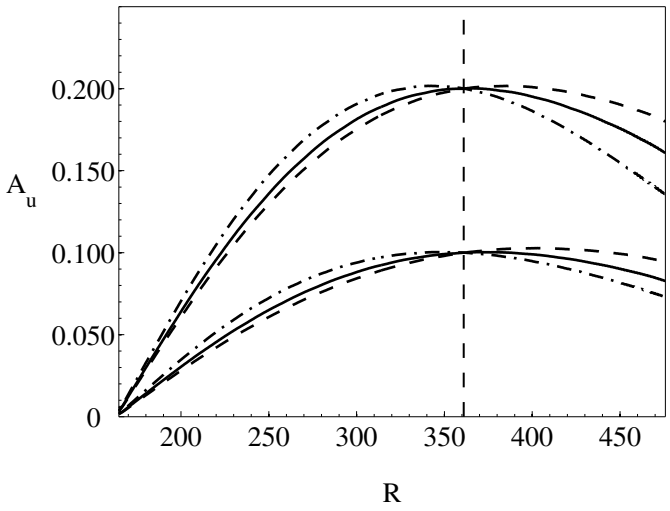

Figure 3.2: The evolution of the streak amplitude A_u is plotted versus downstream Reynolds number, for three streak frequencies: - - -, $F = 0$; ——, $F = 20$; — · —, $F = 40$. Two maximum streak amplitudes, $A_u = \{10, 20\}\%$, at the target location $R = 360$ are shown.

streak amplitude. The streak distortion is calculated from the total streamwise velocity u_2, according to $u_1 = u_2 - U_0$, where U_0 is the nonlinear mean flow obtained by spanwise and temporal averaging. The amplitude is defined by $A_u = \max|u_1|$. The downstream evolution of A_u is presented in figure 3.2 for different frequency streaks.

In figures 3.1 and 3.2 the streamwise location of the stability analysis is indicated with a dashed line. In figures 3.3 and 3.4, the base flow is illustrated at this location, in the cross-stream plane, for both steady and unsteady streaks. At left, line contours of the total boundary layer flow u_2 are shown, and at right the perturbation, u_1, is plotted with filled contours. The steady streak has unchanging high- and low-speed regions in the $z-$direction, but this is not the case for unsteady streaks as shown in figure 3.4. Results from the previous chapter supported the importance of this unsteadiness, but two different aspects could have played a role: The alternation of the streak perturbation in time (compare the profiles at $t = 0$ and $t = \pi/\text{Real}\{\omega\}$ in figure 3.4); also, the wall-normal profile of the streak, which depends on the frequency of the forcing. For example at $t = \pi/2\text{Real}\{\omega\}$ in figure 3.4,

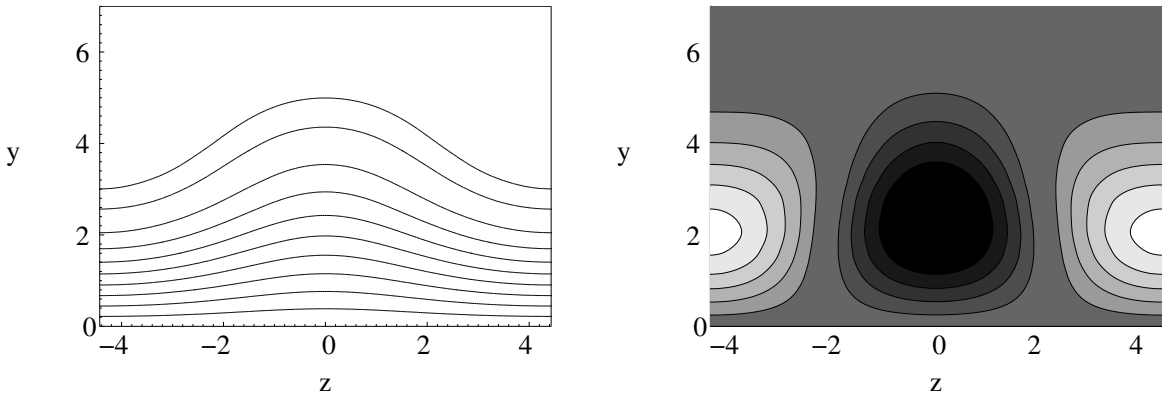

Figure 3.3: The nonlinear base flow in the cross-stream plane at $R = 360$. At left contours of the total base flow are shown at levels $u_2 = \{0.1, 0.2, \ldots, 0.9, 0.95\}$. At right contours of the perturbation, $u_1 = u_2 - U_0$ are shown at intervals of 0.025 away from zero, darker areas are negative perturbations, lighter areas are positive. In this case $F = 0$ and $A_u = 15\%$.

high- and low-speed regions of the streak overlap in the wall-normal direction. Results in the next chapter shed light on the different effects of unsteadiness in the base flow.

The spanwise and temporal variation of the base flow shown in figures 3.3 and 3.4 are dominated by the fundamental frequency and spanwise wavenumber of the forcing mode (ω and k_z). However, due to nonlinear effects, some energy is transferred to higher harmonics, and the base flow is therefore described with a Fourier expansion,

$$u_2(y, z, t) = U_0(y) + u_1(y, z, t), \tag{3.1}$$

where,

$$u_1(y, z, t) = \sum_{n=0}^{M} \sum_{m=0}^{N} \text{Real}\{\hat{u}_1^{m,n}(y) e^{i(m\omega t + n k_z z)}\}. \tag{3.2}$$

Note that since the nonlinear mean flow distortion is represented in U_0, the steady component $u_1^{0,0}$ is zero.

Three components of the base flow expansion are presented in figure 3.5, for unsteady streaks with $F = 60$ and amplitudes $A_u = \{10, 20\}\%$. Two features of figure 3.5 are due to

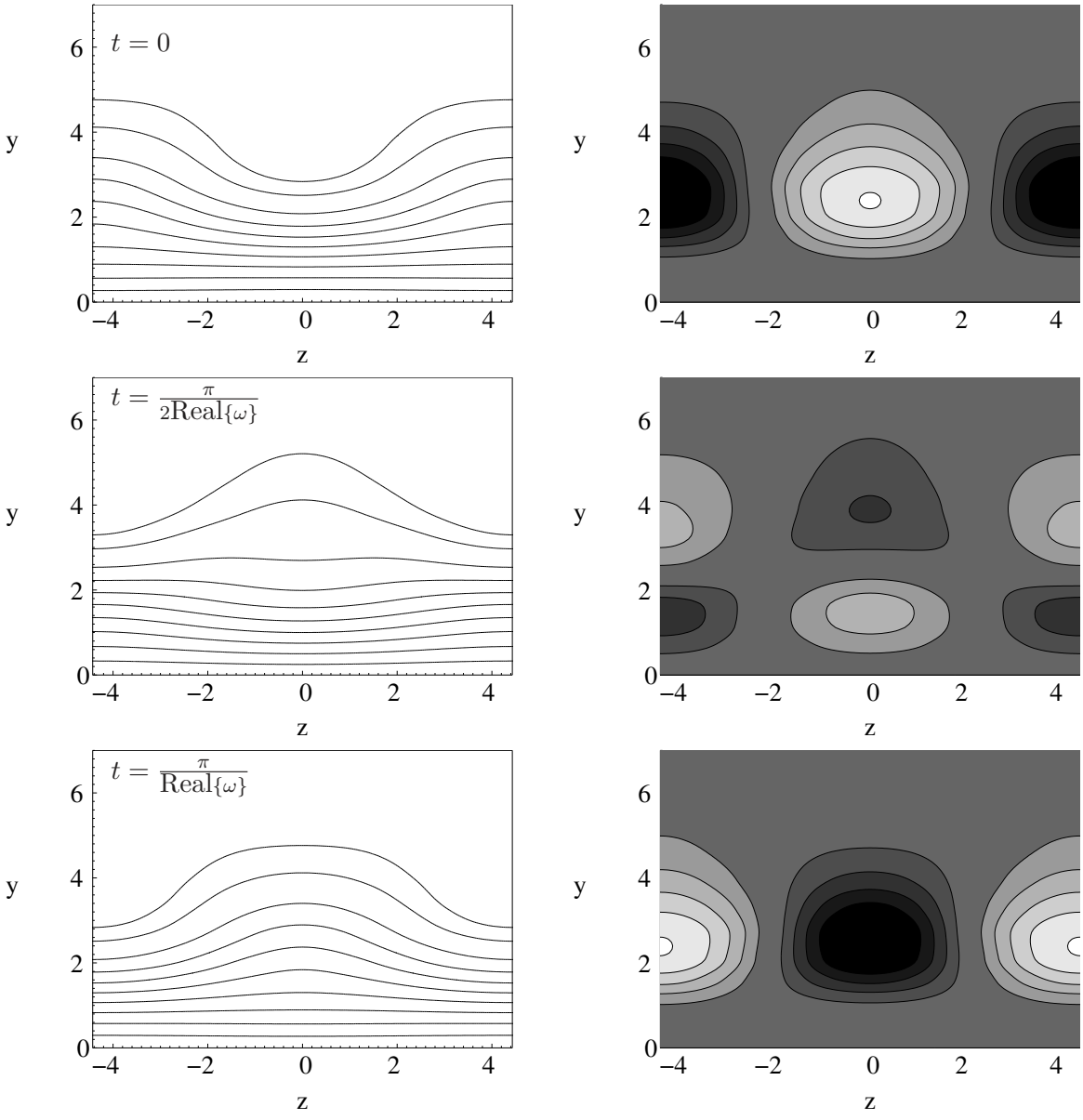

Figure 3.4: The nonlinear base flow in the cross-stream plane at $R = 360$. In this case $A_u = 15\%$, $F = 60$ and the rows correspond to different phases in the unsteady base flow's period. At left contours of the total base flow are shown at levels $u_2 = \{0.1, 0.2, \ldots, 0.9, 0.95\}$. At right contours of the perturbation, $u_1 = u_2 - U_0$ are shown at intervals of 0.025 away from zero, darker areas are negative perturbations, lighter areas are positive.

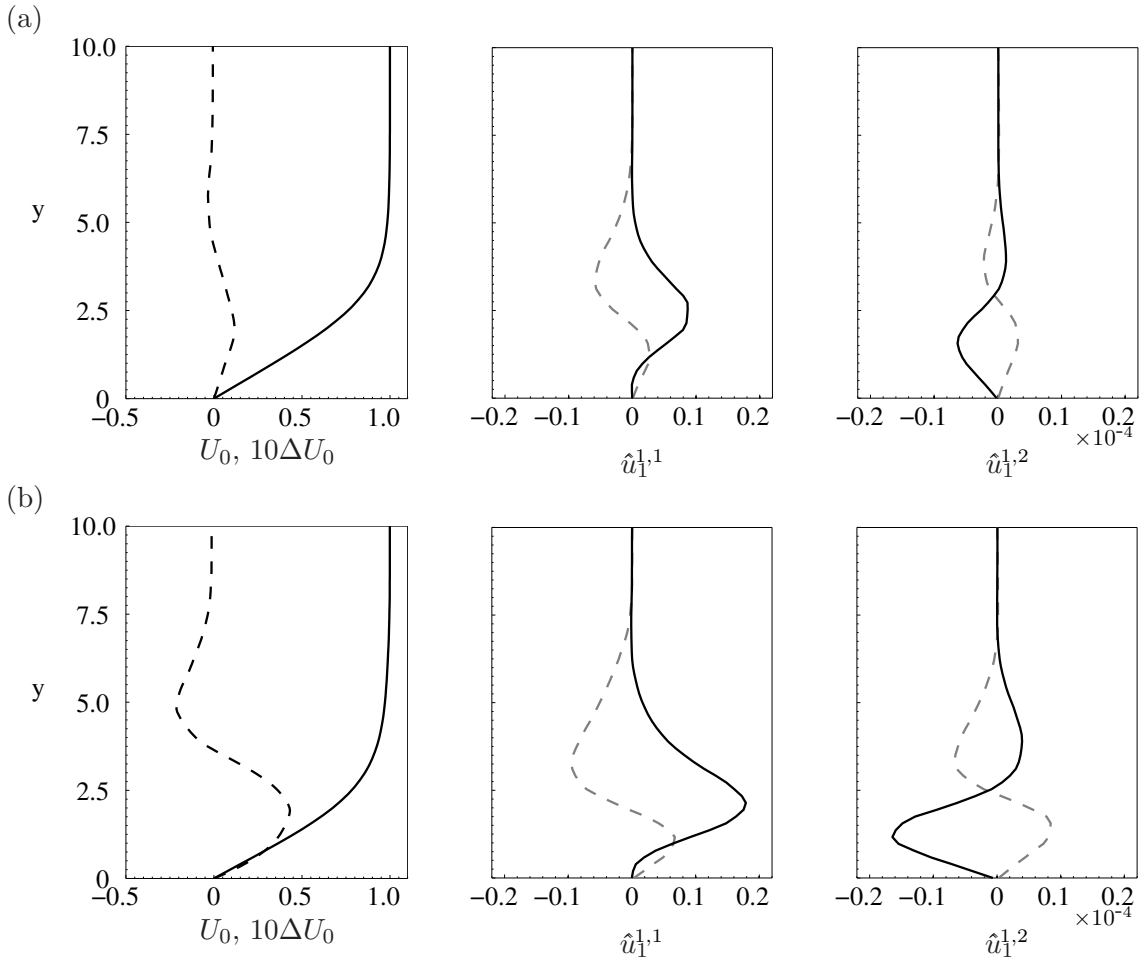

Figure 3.5: The wall-normal profile of three base flow components at the target Reynolds number, $R = 360$. In the top row (a) the streak amplitude is $A_u = 10\%$; in the bottom row (b) $A_u = 20\%$. The frequency is $F = 60$ in both cases. At left the mean flow, U_0 (——) is plotted along with the distortion from the Blasius solution, scaled for clarity, $10\Delta U_0$)(- - -). At right, the real (——) and imaginary (- - -) parts of two Fourier components of the perturbation streak, $\hat{u}^{m,n}$ are presented.

nonlinearity: (a) The mean flow distortion from the Blasius profile, $U_0 - U_{Blasius}$, which is scaled by a factor of 10 for clarity and (b) the small level of energy in the higher harmonic. As the amplitude of the streak is increased, so does the energy in the second spanwise harmonic, and the magnitude of the nonlinear mean flow distortion also increases. In this example with $F = 60$, $\Delta U_0 = \max_y(|U_0 - U_{Blasius}|)/U_\infty = 1.36\%$ for $A_u = 10\%$, which compares closely to the experiments of Westin *et al.* (1994) and $\Delta U_0 = 4.35\%$ for $A_u = 20\%$. Thus the effects of nonlinearity increase with amplitude, which poses the question of how to truncate the Fourier expansion (3.2) for numerical purposes.

This was addressed by quantifying the amount of energy that was captured by a truncated Fourier series, and comparing it to the total perturbation energy. The comparison was made at $R = 360$, and the $y-$location at which the peak u_{rms} perturbation signal was recorded. The relative error when including $M = N = 2$ modes in the temporal and spanwise expansions was described by,

$$\mathcal{E} = 1 - \sum_{n=0}^{2}\sum_{m=0}^{2} E_{m,n}/E_{total}, \tag{3.3}$$

where $E_{m,n}$ is the energy content in the $\hat{u}_1^{m,n}$ mode, and $E_{total} = \sum_{n=0}^{\infty}\sum_{m=0}^{\infty} E_{m,n}$. Figure (3.3) shows the amount of energy not represented by truncating the series, for all the streak frequencies and amplitudes considered. Stronger nonlinear interactions emerge as the amplitude and frequency of the streaks are increased. However, including only two modes in the Fourier expansions is sufficient to reduce the amount of energy omitted to approximately two orders of magnitude lower than the total energy, even for the worst case. Therefore $M = N = 2$ modes was selected as the truncation level in defining the nonlinear base flow streaks for the subsequent stability analysis.

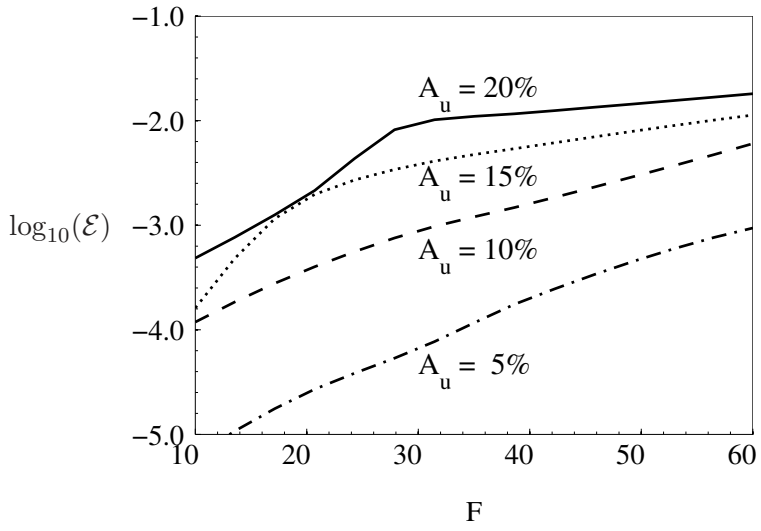

Figure 3.6: Relative error due to truncation of the Fourier series expansion of the base streak. The error is plotted for the range of streak frequencies and amplitudes considered in the stability analysis.

3.3 Stability formulation

The secondary stability equations are derived by considering linear perturbations to the base state, defined by equation (3.1). The base flow varies in time, but since it is extracted from the DNS at a particular streamwise location, it does not vary in this dimension, and the approach is slightly different from chapter 2. The equations are cast in the stationary frame, and the following form for the perturbed state is assumed,

$$\boldsymbol{v}(x,y,z,t) = \{U_0(y) + u_1(y,z,t)\}\mathbf{e}_x + B\boldsymbol{v}_3(x,y,z,t). \tag{3.4}$$

Substituting equation (3.4) into the Navier-Stokes equations, subtracting the terms satisfied by the base state u_2, and assuming B is small enough for linearisation, therefore neglecting terms $O(B^2)$, leads to the linear stability equations. As in the previous formulation, three equations are required, and, in line with the conventional Orr-Sommerfeld and Squire system, two equations govern $\nabla^2 v_3$ and η_3,

$$\begin{aligned} & \frac{\partial^2 U_0}{\partial y^2}\frac{\partial v_3}{\partial x} + \left(\frac{1}{R}\nabla^2 - \frac{\partial}{\partial t} - U_0\frac{\partial}{\partial x} - u_1\frac{\partial}{\partial x}\right)\nabla^2 v_3 \\ + & \left(- \left[\frac{\partial^2 u_1}{\partial y \partial z} + \frac{\partial u_1}{\partial z}\frac{\partial}{\partial y}\right]\eta_3 + \left[\frac{\partial \xi_3}{\partial x} - \frac{\partial \zeta_3}{\partial z}\right]\frac{\partial u_1}{\partial z} \right. \\ & \left. + \frac{\partial v_3}{\partial x}\left[\frac{\partial^2 u_1}{\partial y^2} - \frac{\partial^2 u_1}{\partial z^2}\right] + \left[\frac{\partial u_3}{\partial z} + \frac{\partial w_3}{\partial x}\right]\frac{\partial^2 u_1}{\partial y \partial z}\right) = 0, \end{aligned} \tag{3.5a}$$

$$\begin{aligned} & \left(\frac{1}{R}\nabla^2 - \frac{\partial}{\partial t}\right)\eta_3 - \frac{\partial \eta_3}{\partial x}U_0 - \frac{\partial v_3}{\partial z}\frac{\partial U_0}{\partial y} \\ - & \left(\frac{\partial \eta_3}{\partial x}u_1 + v_3\frac{\partial^2 u_1}{\partial y \partial z} + w_3\frac{\partial^2 u_1}{\partial z^2} - \frac{\partial v_3}{\partial y}\frac{\partial u_1}{\partial z} + \frac{\partial v_3}{\partial z}\frac{\partial u_1}{\partial y}\right) = 0, \end{aligned} \tag{3.5b}$$

$$\frac{\partial u_3}{\partial x} + \frac{\partial v_3}{\partial y} + \frac{\partial w_3}{\partial z} = 0. \tag{3.5c}$$

Homogeneous boundary conditions are enforced on u_3, v_3, w_3, and on $\partial v_3/\partial y$ at the wall and in the free stream.

The mean flow, U_0, and the periodic flow, u_1, appear as coefficients in equations (3.5)(a and b). Since they are both homogeneous in the streamwise direction, the solution is assumed to be a normal mode in x. However, the base flow is periodic in the spanwise coordinate, and Floquet theory must be invoked for the $z-$dependence of the solution.

With regards to the time dimension, there are two possible ways to account for the periodicity in the base flow, and the form assumed for the solution depends on which level of approximation is used. One approach invokes a quasi-steady assumption where the stability analysis is repeated for each phase of the unsteady base streak. In this case, a normal mode assumption is also possible in time. With the other method, the temporal periodicity of the base streaks is retained in the definition of the base flow, and a Floquet

expansion is therefore required in time as well.

The quasi-steady assumption has been invoked in previous stability analyses of streaky base flows, for example, Wu & Choudhari (2003) adopted such an approach. Like Goldstein & Sescu (2008) who also conducted an inviscid stability analysis on frozen streak profiles, Wu & Choudhari (2003) found backward streaks to be the most unstable, but posed the question of how such intermittent instabilities related to the global Floquet type.

The limitations of the quasi-steady assumption were discussed by Kerczek & Davis (2006), who studied the linear stability of oscillatory Stokes layers. They reasoned that the quasi-steady approximation becomes inappropriate around the critical conditions for instability, where the time scale of amplification is very long and unstable base profiles might propagate away before instabilities could grow locally. Therefore, a Floquet expansion in time is required in order to accurately determine the stability of the time-periodic base flow. For example Blennerhassett & Bassom (2006) studied the instability of a Stokes layer with a Floquet expansion in time, and Luo & Wu (2010) compared the results to their direct numerical simulations of the same base flow at different Reynolds numbers. In subcritical conditions, some phases of the base flow were instantaneously unstable, but others were stable. However, the neutral curve calculated from the Floquet analysis correctly predicted the critical conditions calculated by the DNS. Therefore, rigorously accounting for the time variation of the base flow is particularly relevant around the neutral conditions, for example when calculating the critical streak amplitude for instability.

Furthermore, the growth rates calculated for the inner and outer modes in chapter 2, at higher streak amplitudes, are reasonably low on the convective time scale L_B^*/U_∞^*. In fact, figures 2.18 and 2.25 show that the instability amplification rate is of the same order as the frequency of the streaks, which indicates that the periodicity of the base flow should

be included in the analysis. In the following sections the main results employ a Floquet expansion in time, but to gain additional insight into the effects of unsteadiness, quasi-steady analyses for particular phases of the base flow are also conducted.

The secondary instability $\boldsymbol{v}_3$ can be expressed in the general form,

$$\boldsymbol{v}_3(x,y,z,t) = \tilde{\boldsymbol{v}}_3(y,z,t)\mathrm{e}^{i(\alpha x+\gamma_z z)+\sigma t}. \tag{3.6}$$

In the stability problem for temporally growing modes, both α and γ_z are real parameters, and σ is the complex frequency eigenvalue. When the unsteadiness of the base flow is fully accounted for, Floquet theory states that $\tilde{\boldsymbol{v}}_3$ is periodic in both z and t, with the same period as the base flow,

$$\tilde{\boldsymbol{v}}_3(y,z,t) = \tilde{\boldsymbol{v}}_3\left(y,z+2\pi/k_z,t\right) = \tilde{\boldsymbol{v}}_3\left(y,z,t+2\pi/\mathrm{Real}\{\omega\}\right).$$

The perturbation can therefore be replaced by its Fourier expansion in time and z, and $\boldsymbol{v}_3$ has the form,

$$\boldsymbol{v}_3 = e^{(i\alpha x+\sigma_r t)}\sum_{n=-\infty}^{\infty}\sum_{m=-\infty}^{\infty}\boldsymbol{v}_{m,n}(y)e^{i([nk_z+\gamma_z]z+[m\omega+\sigma_i]t)}, \tag{3.7}$$

where γ_z and σ_i have been absorbed in the summation. An eigenvalue problem is formed when equation (3.7) is substituted into the governing equations (3.5). The growth rate of the instability is given by the real part of the eigenvalue, σ_r, and σ_i represents a frequency offset which is added to each component of the frequency expansion.

Since the spanwise periodicity is accounted for with Floquet theory, like in chapter 2, the meaning of γ_z is the same as previously described. Furthermore, similar arguments

apply with respect to the symmetries in the base flow. For example sinuous and varicose solutions can be decoupled, and in the case of subharmonic spanwise expansions, the two spectra collapse in the presence of unsteady streaks.

However, in the streamwise dimension, there is no Floquet expansion and a normal mode is assumed, therefore the streamwise detune factor, γ_x, is not required. Instead, in the expansion for time, σ_i appears like a tuning, and in the present formulation σ_i is part of the eigenvalue which is solved for, as opposed to being a parameter. In the stability solutions presented in the next chapter, σ_i effectively accounts for the discrepancy between the frequency of the base flow and the instability modes. The result is that in spite of the disparity between the frequencies of the base flow and the instability, a large Fourier expansion in time is not necessarily required. Therefore, an offset in the indices of the Floquet expansion, along the lines of 'A_{off}', is no longer required. Instead, the most unstable mode is found by varying the streamwise wavenumber of the normal mode, α.

For the quasi-steady analyses, time is a parameter in the base sate,

$$u_2(y,z) = U_0(y) + u_1(y,z;t_q). \tag{3.8}$$

This leads to a simplification in the general form of the secondary instability. Since the base state for each individual phase is assumed steady, the temporal Fourier expansion in equation (3.7) can be truncated at $m = 0$, which is equivalent to a normal mode in time,

$$\boldsymbol{v}_3 = e^{(i\alpha x+\sigma t)} \sum_{n=-\infty}^{\infty} \boldsymbol{v}_{0,n}(y) e^{i([nk_z+\gamma_z]z)}. \tag{3.9}$$

Depending on whether the global Floquet solutions are sought, or the quasi-steady assumption is invoked, equation (3.7) or (3.9) is substituted into the governing equations

and a computer algorithm forms the matrix eigenvalue problem,

$$\boldsymbol{A}\bar{\boldsymbol{x}} = \sigma \boldsymbol{B}\bar{\boldsymbol{x}}. \tag{2.32}$$

Compared to the previous implementation, described in section 2.2.4, the current algorithm is more complex. For example each component of the base-flow expansion, $\hat{u}_1^{m,n}$ in equation (3.2), is taken into account sequentially when updating the matrices, $\boldsymbol{A}$ and $\boldsymbol{B}$. As before, this involves taking the product of individual components of the solution expansion ($\boldsymbol{v}_{m,n}$ in equation 3.7), with components from the base-flow expansion. For each combination, the resulting frequency-wavenumber vector is different from the original frequency-wavenumber vector of that solution component. Previously, this shift was limited to the fundamental frequency and wavenumber of the base flow. However since higher harmonics of the base-flow are now included, the shift depends on which component of base-flow expansion, is under consideration.

Additional complexity arises from the time dependence of the solution which now includes two parts. Equation (3.7) shows $\boldsymbol{v}_3$ is described by both an exponential dependence on time, with the eigenvalue as the exponent, and a Fourier expansion. The product rule is therefore used to implement terms involving $\frac{\partial \boldsymbol{v_3}}{\partial t}$: the time derivative of the Fourier expansion requires matrix $\boldsymbol{A}$ to be updated, but the time derivative of exponential term affects matrix $\boldsymbol{B}$, since it is multiplied by the eigenvalue.

3.4 Validation

The validation of the numerical implementation of the Floquet solution was reassessed for the case of a time dependent base flow, and a nonlinear base flow. Different aspects of

the algorithm are tested in isolation. Since the streamwise Floquet expansion was effectively replaced by a temporal expansion, the comparison against the data on the secondary instability of TS waves in Herbert (1988) is no longer sufficient. Instead the present implementation is compared to the literature on instabilities of time dependent base flows. Also, the spanwise expansion is re-evaluated in the context of nonlinear steaks, and the current algorithm is tested against two sets of data from the literature.

3.4.1 Validation of the time dependent Floquet algorithm

Blennerhassett & Bassom (2006) studied the linear instability of the oscillatory base flow between two parallel plates oscillating synchronously in their own planes. The base flow was driven by viscosity only i.e. there was no mean pressure gradient. The analytic form for the base flow,

$$\boldsymbol{v}_2 = \big(\text{Real}\{\frac{cosh([1+i]y)}{cosh[1+i]h}\mathrm{e}^{i\omega t}\}, 0, 0\big)^T, \tag{3.10}$$

was implemented in the validation algorithm. Stability calculations were performed at a plate separation of $h^* = 32L^*_{Stokes}$, where $L^*_{Stokes} = \sqrt{2\nu^*/\omega^*}$, and ω^* is the frequency of wall-oscillation. Based on this length scale, three different Reynolds numbers were investigated, $R = \{570, 700, 750\}$. Since the base flow was homogeneous in the streamwise and spanwise directions, Floquet expansions were not required, and two dimensional solutions with a streamwise normal mode assumption were calculated. For the validation tests, a wavenumber of $\alpha = 0.3$ was selected.

Under these conditions the flow was stable, and the growth rate of the least stable mode was compared to the results of Blennerhassett & Bassom (2006) in table 3.1. The agreement was excellent and the maximum relative error was below 1%. In figure 3.7, the normal-velocity eigenfunction for the even mode at $R = 700$ is presented, and the current

mode	R	Blennerhassett & Bassom (2006)	Current results
even	570	-0.06572	-0.06572
odd	570	-0.11620	-0.11620
even	700	-0.06676	-0.06678
odd	750	-0.11951	-0.12045

Table 3.1: The growth rate of the least stable eigenvalue for oscillatory flow between two plates.

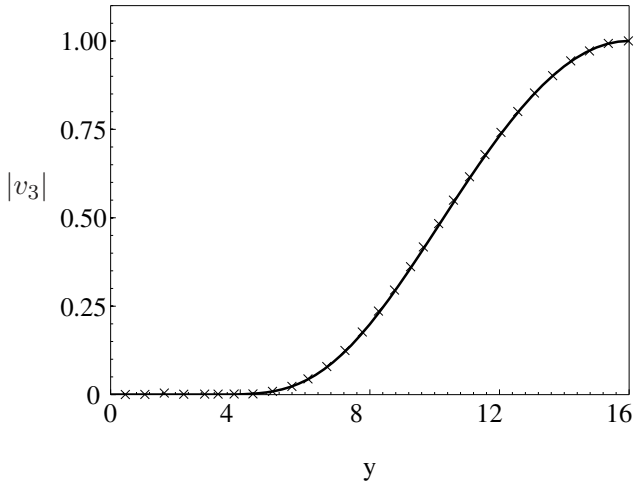

Figure 3.7: The normal velocity eigenfunction for the even mode at $Re = 700$. The wall is at $y = 0$, and the channel centre corresponds to $y = 16$. ——, current results; $\times$, Blennerhassett & Bassom (2006).

results are indiscriminable from those given in Blennerhassett & Bassom (2006). A relatively small number of Floquet modes, $N_A = 4$, was found to be sufficient.

3.4.2 Validation of the nonlinear Floquet algorithm with spanwise periodic streaks

Here the implementation of spanwise-periodic terms in the algorithm is validated against results for steady streaks. The nonlinear base state includes energy in more than one spanwise wavenumber (see equation 3.2), therefore the present algorithm must account for energy in higher harmonics.

Validation was carried out against the results of Andersson *et al.* (2001). They studied the instability of high-amplitude, steady boundary-layer streaks. Their base flow was obtained from the nonlinear evolution of the optimal perturbations and owing to the considerable amplitude required for instability, the transfer of energy from the fundamental wave into the mean flow and higher harmonics was significant. Dr. L. Brandt has kindly provided data for the streaks used in their study, and the base flow used in the current validation had the form,

$$\boldsymbol{v}_2(x', y, z) = \big(U_0(y) + u_{streak}(y, z), 0, 0\big)^T, \tag{3.11}$$

where U_0 is not the Blasius profile, but rather the nonlinearly calculated mean flow, averaged in z and t. Streaks with a large amplitude of 37% were used to test the nonlinear aspect of the code. As a consequence, the number of spanwise harmonics in the Floquet expansion had to be large in order to ensure convergence of the stability results. With ten modes in the spanwise expansion, the growth rate of the most unstable mode, which is a subharmonic sinuous instability, was calculated and the results are presented in table 3.2.

Andersson *et al.* (2001) argued that the instability was inflectional in nature and solved the inviscid stability equations for the spanwise-periodic base flow. However, unlike their inviscid analysis, the present secondary stability equations (3.5)(a and b) include viscous effects. Therefore, in order to validate against the inviscid results, the Reynolds number in the present analysis was gradually increased. Table 3.2 compares the predicted growth rates and phase speeds at different Reynolds numbers to the results from Andersson *et al.* (2001). As the Reynolds number is increased, the present results converge closely towards the inviscid value.

Streamwise velocity eigenfunctions were presented by Andersson *et al.* in their figure

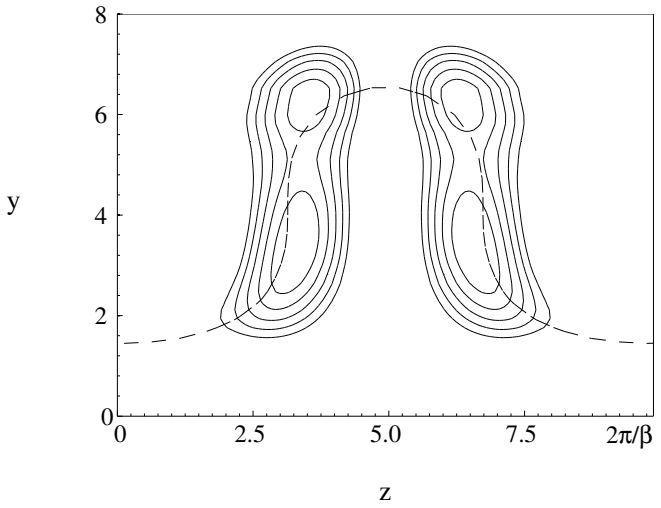

Figure 3.8: Contours of streamwise velocity perturbation in the subharmonic sinuous mode. The mode is normalised by its maximum absolute value, and levels of $|u_3| \in [0.5, 1.0]$ are plotted with a spacing of 0.1. The base flow corresponds to the streak with $A = 37.3\%$ in Andersson *et al.* (2001). The dashed line denotes the distorted critical layer.

R	σ_r	c_r
100	0.01186	0.8693
200	0.01412	0.8633
300	0.01484	0.8619
Inviscid	0.01496	0.8450

Table 3.2: The effect of Reynolds number on the growth rate and wave speed of the subharmonic sinuous instability. The base flow used corresponds to $A = 37.3$ in Andersson *et al.* (2001), and for comparison, the inviscid result comes from that paper.

12(b), and the streamwise disturbance focused on the distorted critical layer, particularly on the flanks of the low-speed streak. A similar plot is shown in figure 3.8 for the instability reported in table 3.2, at $R = 300$. Although the contour levels were not specified by Andersson *et al.* (2001), and the streak amplitude for their results is slightly lower than the value considered for this validation test, there is a strong qualitative agreement in the instability mode shape.

Extra validation is provided by comparison with the results by Cossu & Brandt (2004). They calculated the boundary layer stability in the presence of streaks, and also used a

Floquet expansion in the spanwise direction. As in the case above, their streaks were calculated from the nonlinear evolution of a steady inlet perturbation, with a spanwise wavenumber, k_z. The amplitude was lower than in the preceding validation, but nonlinear effects still lead to a slight distortion of the mean flow from the Blasius solution, and a base flow with energy in the higher harmonics of spanwise wavenumber. Dr. L. Brandt also provided the base flow used for these stability calculations. In the following results: streak A had 0.0 amplitude and represented the undisturbed Blasius flow; streak B had amplitude $0.1396U_\infty$; and streak C had amplitude $0.2017U_\infty$.

The Floquet analysis yielded a fundamental varicose instability which had its origin in the TS wave. Initially, using the Reynolds number given in Cossu & Brandt (2004), the results from the present code and the literature did not match very closely, even for streak A, which was surprising since it was the base case.

By comparing results to the well-known neutral stability curve for Orr-Sommerfeld modes, a new Reynolds number, $R = 3600$, was found which matched the results for streak A. However, for streaks B and C, the results from the Floquet algorithm still did not match the published data, despite using $R = 3600$ and appropriately scaled wavenumbers. A comparison of the results and those of Cossu & Brandt (2004) is presented in figure 3.9. An error was noted in the stability equations used in Cossu & Brandt (2004): their equation (9b) is incorrect and clearly does not follow from their equation (6b). For the purpose of comparison only, the stability equations were changed to the incorrect version found in Cossu & Brandt (2004), and the results are presented in figure 3.10. The streaks have a stabilising effect which increases with streak amplitude, and with the changes above, comparison to data from Cossu & Brandt (2004) shows very good quantitative agreement.

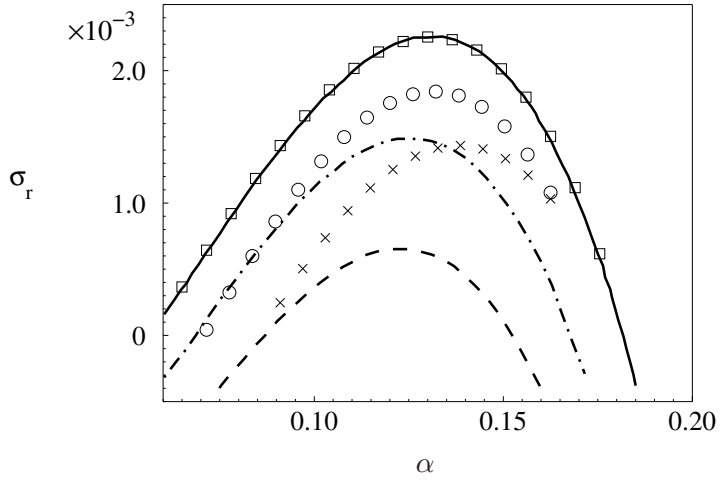

Figure 3.9: Validation against results in the literature for steady streaks at $R = 3600$. Symbols are results from the present algorithm, and lines are obtained from Cossu & Brandt (2004): streak A, (□), ——; streak B, (○), — · —; streak C, (×), - - -. The growth rate of the fundamental secondary instability mode with $\gamma_z = 0$ and varicose symmetry is shown, as a function of the streamwise wave number, α.

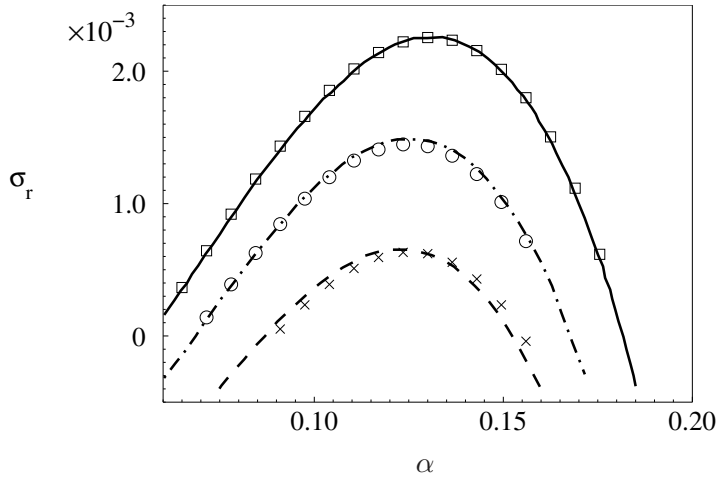

Figure 3.10: Validation against results in the literature for steady streaks at $R = 3600$. As in figure 3.9, the growth rate of the fundamental secondary instability mode with varicose symmetry is shown, and the lines are obtained from Cossu & Brandt (2004). The symbols are results from the present algorithm, with the equations altered to be the same as used by Cossu & Brandt (2004).

With the linear stability method algorithm extended to account for nonlinear and time-periodic base flows, the stability of streaky boundary layers calculated from DNS (section 3.2) was investigated. The results were checked for dependence on the number of modes included in the solution expansions. Similar to the case for unsteady streaks in chapter 2, 50 Chebyshev polynomials were required in the wall-normal expansion to ensure convergence of the numerical solution. In the Floquet expansions for the periodic dimensions, four modes were sufficient. This yielded a system size of 41 million elements. The implicitly restarted Arnoldi iteration method, described by Lehoucq *et al.* (1998), was used for the solution of the eigenvalue problem. The computational cost was reduced by evaluating a subset of the eigen-spectrum, which captured the modes with the largest growth rates, σ_r. Results for the most unstable modes are presented in the following chapter.

Chapter 4

Stability of the boundary layer distorted by nonlinear streaks

4.1 Introduction

In this chapter, the stability of the flat-plate boundary layer distorted by *nonlinear* streaks is evaluated. The base flows, which span a range of streak frequencies and amplitudes, were calculated using DNS (section 3.2). Their secondary instability modes are computed using the Floquet approach introduced in chapter 3.

The parameters of the present analysis were selected to closely reflect the conditions around the initial growth of instabilities leading to breakdown in the simulations of Jacobs & Durbin (2001). The Reynolds number was therefore chosen at the supercritical value $R = 360$, where the TS wave is itself slightly unstable. In contrast to the previous results, where the emphasis was on demonstrating the possible role of unsteady streaks, there is a weak viscous instability in the absence of streaks. However, in the presence of boundary layer streaks, the strong inner and outer mode instabilities exceed the TS wave growth rate and, as previously found, their characteristics depend on the base flow.

The presentation of this chapter is organised as follows. First, the stability of steady,

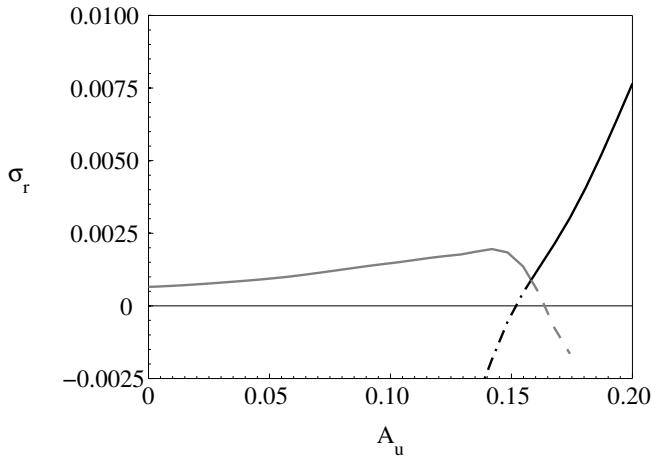

Figure 4.1: The influence of the amplitude of steady streaks ($F = 0$) on growth rate. Two types of modes are plotted. The light line (—— light line) is the growth rate of the inner mode; the dark line (—— dark line) is the outer mode.

non-linear streaks is briefly discussed. This is followed by a detailed discussion of the inner and outer instabilities. For each, the mode structure is examined and the growth rate is reported over a range of streak frequencies and amplitudes. These results are complemented by a discussion of mode competition. Finally, direct numerical simulations of boundary-layer breakdown due to the inner and outer modes are presented. The DNS provide an empirical view of the amplification of the instabilities beyond the linear regime, and transition to turbulence.

4.2 The instability of steady streaks

The most unstable modes of the distorted boundary layer were found, starting with steady streaks, forced by a vortical mode, $\boldsymbol{v}_1$, with frequency Real$\{\omega\} = 0$. Figure 4.1 shows the growth rate of the most unstable mode as a function of streak amplitude, A_u. In the limit $A_u = 0$, this corresponds to the conventional TS wave, which has a marginally positive growth rate. As the intensity of the streaky disturbance is increased, the boundary layer becomes more unstable. This is in line with the overall picture from chapter 2 and, for

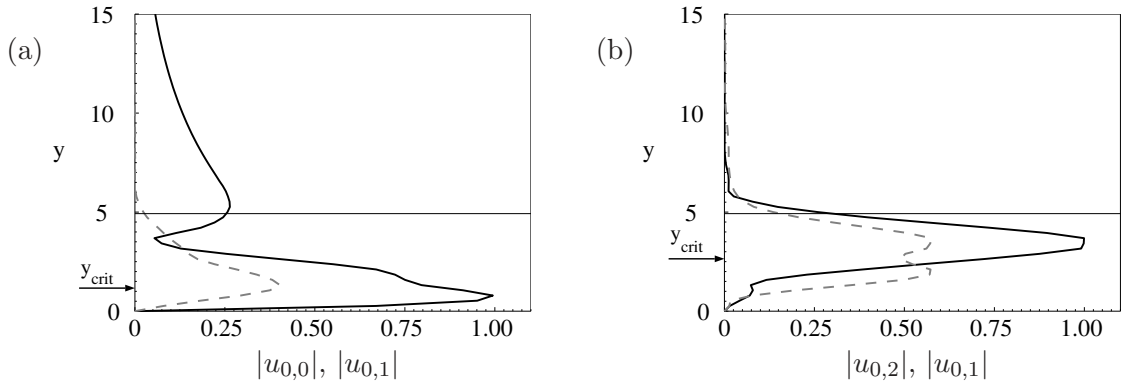

Figure 4.2: Wall-normal profiles of the inner (a) and outer (b) modes. The absolute value of the $u-$disturbance is plotted for (——) the most energetic and (- - -) the second most energetic eigen-components of the Floquet expansion. The location of the critical layer corresponding to the most energetic mode, y_{crit}, is marked by an arrow. The amplitudes are chosen to be unstable for both modes: $A_u = 5\%$ for the inner mode; and $A_u = 20\%$ for the outer mode.

example, the many experiments on boundary layer transition summarised in Abu-Ghannam & Shaw (1980). For low-amplitude streaks, the continuation of TS wave into its fundamental varicose form is the most unstable, and its growth rate initially increases with amplitude. Since the effect is for the streaks to destabilise the TS wave, this instability can be known as the inner mode, though the designation is dubious because the growth rate is increased inappreciably. For the amplitude, $A_u = 5\%$, the wall-normal profile of the inner mode u_3-disturbance is plotted in figure 4.2(a). The critical layer, which is close to the wall, is marked on the figure.

As the streak amplitude is increased further to approximately $A_u \approx 14\%$, the effect of the streak switches, and the inner mode becomes stabilised by the distortion to the base flow. Close to this level of streak amplitude, a separate instability arises which is due to the Klebanoff streaks. The growth rate of this mode quickly increases with streak amplitude, and surpasses the inner mode as the most unstable. It has a subharmonic spanwise expansion with a sinuous symmetry. Note that in the case of steady streaks, the $z = 0$ axis is centred in a low-speed streak, so the subharmonic sinuous mode here

corresponds physically to the subharmonic modes referred to as sinuous in both Andersson *et al.* (2001) and Cossu & Brandt (2004). The streamwise disturbance velocity of this mode is plotted in figure 4.2(b) for a streak with amplitude $A_u = 20\%$. The high critical layer of this instability identifies it as the outer mode. Also, the mode shape closely resembles the averaged data presented in Bakchinov *et al.* (1995) showing the instability of artificially introduced steady streaks.

The results presented in figure 4.1 shed light on the relationship between the instability modes found in previous analyses of steady nonlinear streaks, and the inner and outer modes reported in chapter 2. Generally, the discrepancy between the results in chapter 2 and other theoretical literature using Floquet analysis is reduced when considering steady streaks. For example, Cossu & Brandt (2004) showed that the TS wave is stabilised by high-amplitude streaks, though they did not report results for streaks with an amplitude lower than approximately 14%. A similar conclusion can now be drawn from figure 4.1 for streaks $A_u > 16\%$. Also, the outer mode was shown in chapter 2 to become unstable around an amplitude of $A_u = 7.5\%$ in the presence of unsteady streaks, which is in agreement with much experimental data, but considerably lower than calculated by Andersson *et al.* (2001) for steady streaks. In the present analysis, with $F = 0$, the critical amplitude for the outer mode is still low, yet closer to the value predicted by Andersson *et al.* (2001). This improved comparison between the present results and the literature on optimal streaks is not surprising, since with $F = 0$, the base flow is more similar to the optimal streak insofar as it is steady.

However, the findings in chapter 2, and the subsequent results for unsteady streaks, emphasise that $F = 0$ is not necessarily a typical case , rather it is a special case. Although something similar could be physically realised by the use of spanwise periodic roughness

elements, natural FST will have a different effect. A better model for the bypass process is provided by unsteady streaks. In the following sections, the inner and outer modes are analysed with particular attention paid to the effect of unsteadiness in the Klebanoff distortions.

4.3 Inner mode

4.3.1 Growth rate characteristics

The growth rate of the inner mode calculated in the presence of steady streaks in section 4.2 did not exhibit the strongly unstable nature that was seen in the results of chapter 2. However, this could have been predicted from the trend in the unsteady results presented in figure 2.18, and extrapolating to the steady case. In figure 4.3, that link is made explicit, and the growth rate of the inner mode is presented as a function of streak frequency in the range $F \in [0, 60]$, for different amplitude nonlinear streaks. The same strong dependence of the inner mode's growth rate on the frequency of the base flow is observed, as in the preliminary analysis. The base flow used here accounts fully for nonlinear effects, and the destabilisation of the inner mode can therefore be attributed directly to unsteadiness in the streaks, because it does not occur with $F = 0$.

In order to isolate the effect of streak amplitude, the growth rate of the inner mode is presented in figure 4.4 as a function of A_u for two streak frequencies, $F = \{20, 60\}$. Figure 4.4 complements the results in figure 4.3 and emphasises that the destabilising effect of unsteady streaks does not set in until $A_u > 7.5\%$.

Figures 4.3 and 4.4 exhibit two regimes in which the streaks actually have a small stabilising effect on the inner mode, contrary to the general trend. One of these regimes is for steady streaks, previously mentioned, and explained later in section 4.3.4. The other

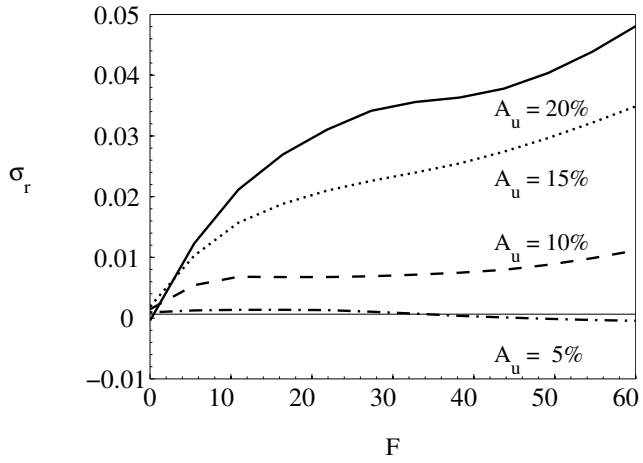

Figure 4.3: The influence of streak amplitude and frequency on the growth rate of the inner mode. The lines represent different amplitude streaks: — · —, $A_u = 5\%$; - - -, $A_u = 10\%$; · · · ·, $A_u = 15\%$; ——, $A_u = 20\%$. The growth rate of the TS wave for the Blasius boundary layer is marked by the horizontal line.

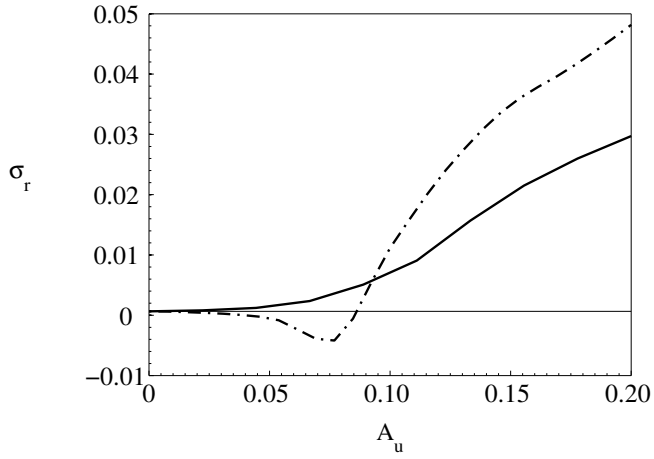

Figure 4.4: The influence of streak amplitude on the growth rate of the inner mode. The two line represent different frequencies of streaks, ——, $F = 20$; — · —, $F = 60$.

regime is for moderate amplitude streaks around the high end of the frequency range. The enhanced stability for high-frequency, low-amplitude streaks can be compared to the work of Grosch & Salwen (1968). They studied the stability of time-dependent plane Poiseuille flow. Their base flow included a steady and an unsteady component – akin to the present mean flow with unsteady streaks. Those authors found that modest amplitudes of the unsteady component of the base flow tended to stabilise the flow, whereas the higher amplitudes made the flow unstable. For example, when the amplitude of the oscillating component was increased to approximately 10% of the steady velocity, the instability had a growth rate approximately one order of magnitude larger than the typical instability of the steady flow. A similar observation can be made in the current context. The stabilisation effect is, however, not significant in comparison to the substantial increase in growth rates due to unsteady streaks with amplitude $A_u > 10\%$

The discussion of the inner instability has thus far overlooked the propensity of lower frequency streaks to reach higher amplitudes, A_u. In particular, for the same level of free-stream forcing, lower-frequency vortical disturbances penetrate deeper into the boundary layer, and cause amplification of the Klebanoff streaks to higher A_u levels (Zaki & Durbin, 2005). This was illustrated in section 2.2.1 with figures 2.2 and 2.6. Instead of constant A_u, it is more appropriate to consider constant values of A_v or A_w of the free-stream vortical mode which causes the generation of streaks. The strength of the streak response, A_u, is frequency dependent, and is determined from the DNS.

The value of A_v was selected such that the induced streaks amplified to $A_u = 15\%$ at $R = 360$ when the frequency was $F = 10$. The dependence of A_u on frequency is shown in figure 4.5(a). In figure 4.5(b), the growth rate of the inner instability is plotted versus streak frequency, here at constant A_v. In the steady streak limit, $F = 0$, the inner mode

is only slightly unstable, despite the high value of A_u. The growth rate increases rapidly as the streaks become unsteady, especially in the lower frequency range where they reach high amplitude. While higher levels of unsteadiness are destabilising, the streak amplitude A_u decreases with frequency and reduces the instability growth rate. Therefore, an optimal range of streak frequencies emerges. Lower frequency streaks do not introduce sufficient unsteadiness, and higher frequency streaks occur at weaker, more stable amplitudes.

In the context of bypass transition, a spectrum of streak amplitudes and frequencies is generated in response to forcing by free-stream turbulence. The low frequency components of this forcing, *not* $F = 0$, play the most significant role with regards to enhancing the inner instability. The high-frequency components are less significant due to their low propensity to generate high-amplitude streaks.

4.3.2 Structure of the inner mode

Having established in the previous section that the inner mode can grow at a significant rate, here the form of the instability is examined in the cross-stream plane. The distribution of energy associated with the three velocity components for a typical inner instability is presented in figure 4.6. The panels contain two spanwise wavelengths of the streak.

For the instability mode, the root-mean-square values in time are presented. The velocities are normalised by the maximum absolute value of a particular component from the Floquet expansion, maximised over all the frequencies, wavenumbers, velocity components and y-locations. To gain insight on how the inner mode derives energy from the base flow, line contours of the total base flow u_2 are also presented on the left side of each panel in 4.6. The illustration of the base flow corresponds to a particular phase of the unsteady base state, like a particular time point in figure 3.4. At a different point in time the low speed

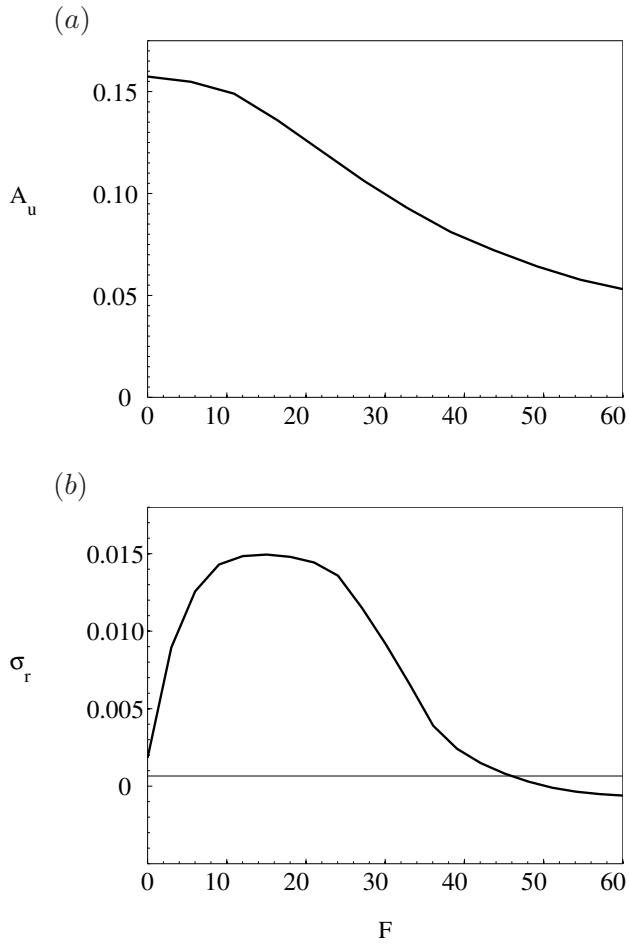

Figure 4.5: (a) The dependence of streak amplitude A_u on F, when $A_v = 4.5 \times 10^{-3}$ is held constant. (b) Growth rate of the inner mode versus the streak frequency at constant A_v. The growth rate of the TS wave for the Blasius boundary layer is marked by the horizontal line.

streaks, indicated by the raised u_2 contours, would be replaced by high speed streaks and vice-versa.

Since the inner mode is driven by high-amplitude streaks with significant unsteadiness, the parameters in figure 4.6 were chosen as $F = 60$, $A_u = 20\%$. The inner instability is a varicose mode with a fundamental spanwise wavenumber expansion, and in the u_3-component a significant two-dimensional disturbance can be seen along with the spanwise dependent component. This component has a spanwise wavelength of $2\pi/k_z$, though it appears that four spanwise wavelengths of the disturbance fit inside the view, and this is due to the time averaging (Andersson *et al.*, 2001). The streamwise component dominates the inner mode, and the distribution of its energy in the span correlates with the centre of the streaks. In these spanwise locations, the streak disturbance is maximum. Although the spanwise shear $\partial u_1/\partial z$ is at a minimum, the disturbance of the wall-normal profile $u_1(y; z, t)$ is the greatest. The energy distribution in 4.6 therefore supports the view that the inner mode is driven by the wall-normal base flow profile, mentioned in chapter 2. This is also in line with observations of varicose instabilities, for example Brandt *et al.* (2004) show, in their figure 12, a varicose instability growing and breaking down on the centre-line of an unsteady streak.

The v_3 component of the inner mode also contains both two- and three- dimensional components, though its amplitude is smaller than u_3. The gradual decay of v_3 in the the wall-normal direction harks back to the inner mode's origin in the TS wave. The spanwise disturbance velocity, w_3, is purely three-dimensional. Due to varicose symmetry, it is located on the flanks of the streak, and is much smaller in amplitude than u_3.

The structure of the inner mode shows that the instability is focused on the streaks, but it poses the question of why only unsteady streaks significantly destabilise the inner mode,

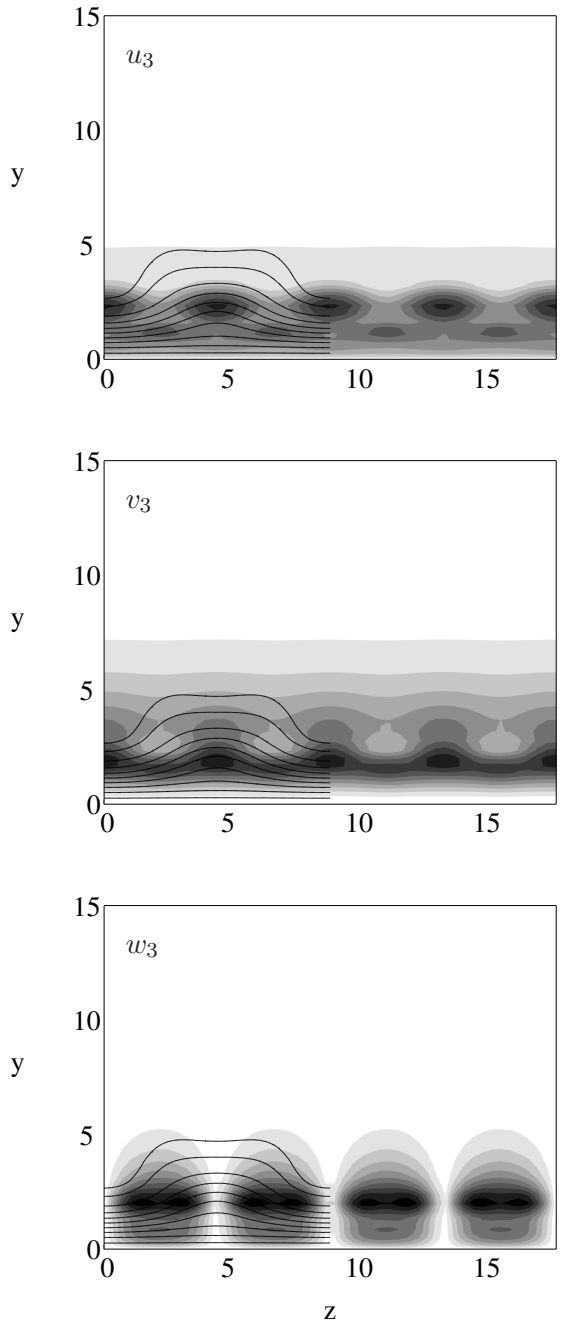

Figure 4.6: Filled contours of the three velocity components of the inner mode, plotted in the cross-stream plane for a streak with $A_u = 20\%$, $F = 60$. Root-mean-square values, with time averaging are presented. The contour levels are: $0 \leq u_3 \leq 1.25$, $0 \leq v_3 \leq 0.5$, $0 \leq w_3 \leq 0.3$. The unfilled contour lines correspond to one phase of the base flow, $u_2 = \{0.1, 0.2, \ldots, 0.9, 0.95\}$.

because steady streaks also disturb the wall-normal base-flow profile. This issue is addressed in the following section by means of quasi-steady analyses which allow the separate effects of unsteadiness to be isolated.

4.3.3 Quasi-steady analysis of the inner mode

In quasi-steady analyses, the unsteady base flow is effectively frozen at a particular time-point in the cycle. The instantaneous base state is used for a stability analysis, which therefore assumes the base flow to be steady. The eigenvalue spectra depend strongly on which phase of the base flow is selected, and this affirms the importance of accounting for all phases. However the inner mode can still be identified in the spectrum for the fundamental varicose expansion, and extra understanding of the instability can be derived from the quasi-steady results.

The growth rate of the inner mode was calculated with quasi-steady analyses as a function of amplitude, and the minimum- and maximum- over all phases of the base flow are presented in figure 4.7. The quasi-steady flows were taken from streaks with $F = 20$, and the results are compared to streaks with steady upstream forcing. The most unstable phase of the unsteady base flow is much more unstable than the actually steady streak, even though in both these cases, the base flow in the stability calculation did not vary with time. This indicates that the shape of streaky perturbation in the cross-stream plane, and how this depends on unsteadiness, plays a very significant role in the inner mode. The growth rate of the inner mode is also plotted for the most stable phase in the quasi-steady analysis. In this case, the inner instability is damped. These results are somewhat in line with the 'intermittent instability' proposed by Wu & Choudhari (2003).

The effect of frequency is explored further in figure 4.8. The growth rate of the inner

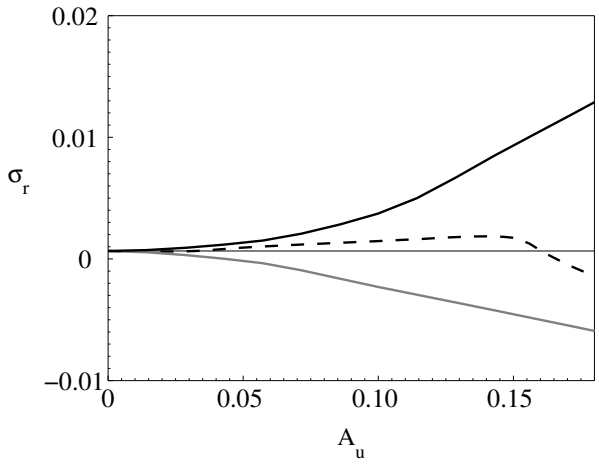

Figure 4.7: The growth rate of the inner mode as a function of streak amplitude for steady streaks (- - -). The growth rates are also shown for the most stabilising (——) and most destabilising (——) phases of the streak with $F = 20$.

mode is plotted versus streak frequency. Quasi-steady calculations with the most unstable phase of the base flow were used. With the quasi-steady approach, the only difference between two cases with a different F is in how the streak disturbance, $u_1(y, z; t_q)$, varies in the y and z dimensions. This gives rise to some discrepancies between the quasi-steady analyses (figure 4.8), and those with a Floquet expansion in time (figure 4.3). For example, a small stabilising phenomenon for high-frequency low-amplitude streaks was discussed in connection with figure 4.3. However, with a quasi-steady assumption, this is not observed. Therefore the phenomenon is due to the oscillation of the base flow in time.

For high-amplitude streaks, although both types of analyses indicate that unsteady forcing leads to instability, and the effect increases with F, the growth rate of the inner mode is higher when the unsteadiness is taken into account. Figure 4.8 therefore demonstrates that some of the effect of high streak frequency is due to changes in the cross-stream shape of the streaks, which can be captured by quasi-steady analyses. However, some of the destabilisation is due to the temporal-oscillation of the base flow, which requires a Floquet

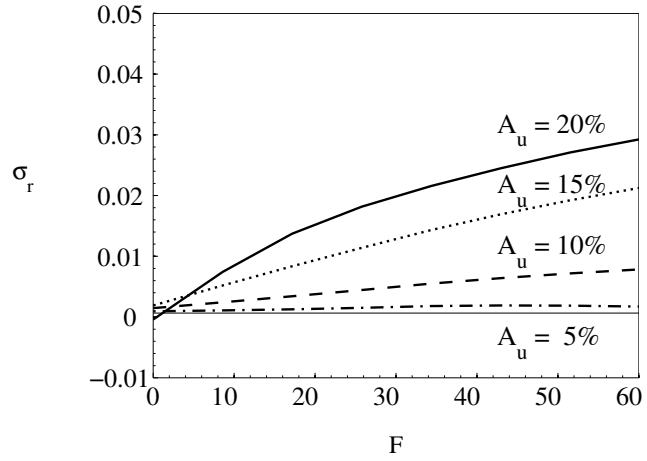

Figure 4.8: The effect of streak amplitude and frequency on the growth rate of the inner mode. The most unstable phase of the unsteady streaks is used in a quasi-steady analysis. The lines correspond to different amplitudes: — · —, $A_u = 5\%$; - - -, $A_u = 10\%$; · · · ·, $A_u = 15\%$; ——, $A_u = 20\%$. The growth rate of the TS wave for the Blasius boundary layer is marked by the horizontal line.

approach.

The base flow used in a particular quasi-steady calculation $u_2(y, z; t_q)$, and the steady $F = 0$ base flow, $u_2(y, z)$, are compared in figure 4.9. This sheds more light on the influence exerted by the wall-normal profile of the base flow. In the top row of the figure, steady streaks with $F = 0$ and $A_u = 10\%$ are presented. At left the streak profile, u_1 is plotted in the wall-normal direction, at various $z-$locations over the whole spanwise wavelength. Both forward and backward streaks are visible. At right, the corresponding wall-normal curvature of the total base flow is shown, $\partial^2 u_2/\partial y^2$. The dominant negative curvature corresponding to the conventional boundary layer flow is evident. It is slightly modified by the streak, but $\partial^2 u_2/\partial y^2$ does not cross the zero-axis. In the bottom row of figure 4.9, the most unstable temporal phase of the unsteady streaks with $F = 60$ and $A_u = 10\%$ is shown, also for different $z-$locations. The streak profile is more complicated in this case. In pane (d) it is clear that an inflection point is introduced close to the wall, due to the streaky disturbance. Even for this moderate streak amplitude, a significant portion of the

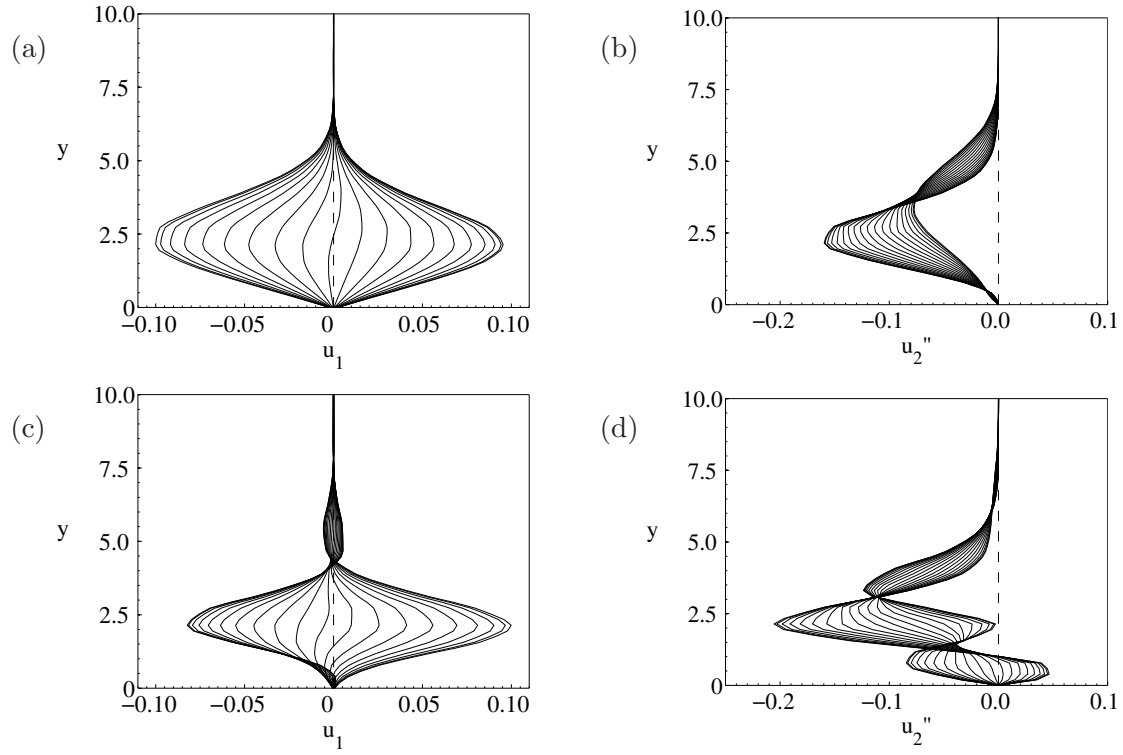

Figure 4.9: A comparison of steady streaks $(a-b)$, and unsteady streaks with $F = 60$ $(c-d)$, in both cases $A_u = 10\%$. The streak disturbance, u_1, is plotted in $(a-c)$ at various $z-$locations spanning one wavelength. In $(b-d)$ the wall-normal curvature of the total flow, u_2, is given. In the unsteady case, the most unstable phase from the quasi-steady analysis is presented.

spanwise wavelength is inflectional. Similar results were found by Wu & Choudhari (2003) and Goldstein & Sescu (2008) who noted the link between unsteadiness in the upstream vorticity perturbations and wall-normal curvature downstream.

The presence of inflection points means that the inviscid Rayleigh instability mechanism could be significant in transforming the viscous TS instability into the strongly amplified inner mode. The fact that the inner mode is only destabilised in the presence of unsteady streaks directly supports this view. Though the inviscid theory is for two-dimensional flows and the base flow in this case also varies in the span, a similar connection between inflectional wall-normal profiles caused by streaks and instabilities associated with bypass transition was made by Goldstein & Sescu (2008). Furthermore, in all cases here, the most

unstable temporal phase of the base flow was inflectional for a significantly larger proportion of the spanwise wavelength than the most stable phase. In addition, as the frequency was increased, the most unstable phase became inflectional for more of the spanwise wavelength. For example, at $F = 20$ and $A_u = 20\%$ approximately 60% of the spanwise wavelength was inflectional for the most unstable phase. This level was increased to approximately 90% for the higher frequency base flow, $F = 60$.

Goldstein & Sescu (2008) noted that the maximum amplitude of the instability tended to occur at the inflection point. Here too, the relevance of the wall-normal inflection points is demonstrated by connecting the spanwise locations where the base flow is inflectional to the cross-stream distribution of energy in the inner instability. Figure 4.10 illustrates the base flow corresponding to the inner mode shown in figure 4.6. In that figure, the inner mode's energy was centred where the streaks were predominantly forward or backward facing, not in between spanwise-neighbouring streaks. Contours of u_2 were also shown for a single phase of the base flow; specifically, the most unstable. Here that base flow is analysed closely, and the streak profile and curvature at three particular z-locations are plotted. Figure 4.10 shows that strong inflection points exist where the inner mode amplitude is large: the forward streak (- - -) exhibits an inflection point close to the wall, whereas the backward streak (— · —) has an inflection point in the middle of the boundary layer. In contrast, at a z-location between streaks (——), where u_1 is small, away from the majority of the inner mode energy, the base flow is not inflectional.

4.3.4 Effect of nonlinearity in the base flow on the inner mode

In addition to the striking effects of unsteadiness discussed in the previous section, nonlinearity in the base flow has a considerable impact on the inner mode. The preliminary

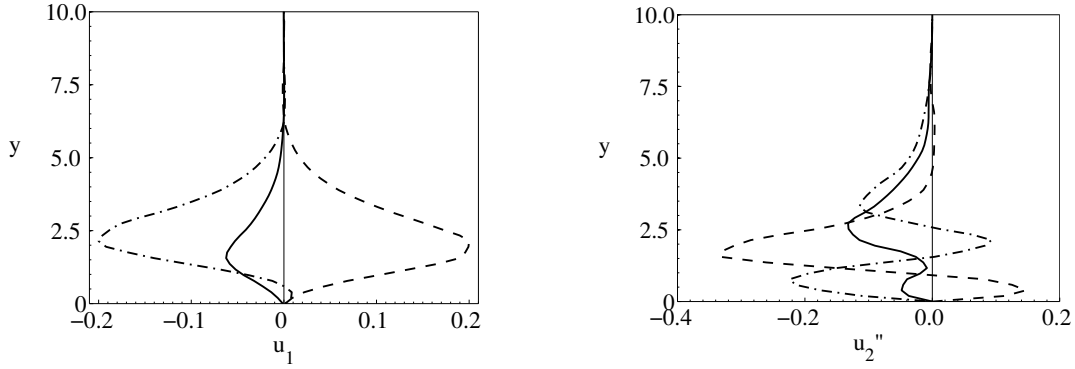

Figure 4.10: The most unstable phase of the streak with $F = 60$ and $A_u = 20\%$, corresponding to base flow in figure 4.6. At left the streak disturbance, u_1, is plotted at three $z-$locations, at right the wall-normal curvature of the total flow, u_2, is given. Each line style links the same z-location in both figures.

results in chapter 2 did not take this into account: the streaky component of the base flow, u_1, was simply scaled by A_u. Here, the nonlinear base flow was recalculated for each streak amplitude, and A_u was not a parameter, rather an outcome of the nonlinear calculation for the streak. For simulations with different streak amplitudes, the nonlinear effects were slightly different, therefore the distribution of streak energy in the cross-stream plane, and amongst the modes of the Fourier expansion for the base flow was altered slightly.

Nonlinearity also affects the base flow through the distortion to the mean boundary layer flow, U_0, which deviates from the Blasius solution due to nonlinear transfer of energy. The distortion was illustrated in figure 3.5 for two streak amplitudes, and in the preceding sections this distortion was implicitly included in the nonlinear base state. Here, the growth rate of the inner mode is recalculated without the distortion, and the mean streamwise flow is therefore given by the Blasius solution, $U_0 = U_{Blasius}$. Figure 4.11 shows the results of this analysis and, comparing to the results in figure 4.3, demonstrates the contribution of the mean flow distortion to the stability results. In general, the growth rate of the inner mode is higher when neglecting the mean flow distortion. The most significant departure is seen in the limit $F = 0$, because the inner mode is not stabilised in this regime if the mean

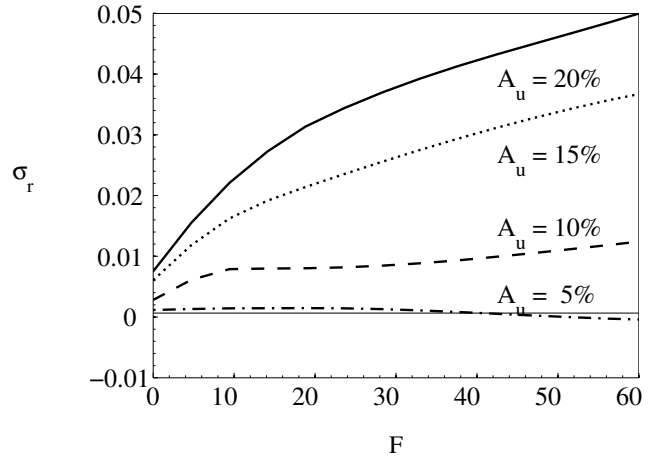

Figure 4.11: The influence of streak amplitude and frequency on the growth rate of the inner mode, neglecting the nonlinear mean flow distortion, $U_0 = U_{Blasius}$. The lines are for different amplitude streaks: — · —, $A_u = 5\%$; - - -, $A_u = 10\%$; · · · ·, $A_u = 15\%$; ——, $A_u = 20\%$. The growth rate of the TS wave for the Blasius boundary layer is marked by the horizontal line. Comparison with figure 4.3 isolates the effect of mean flow distortion.

flow is the Blasius solution.

This finding for steady streaks is in line with the DNS of Cossu & Brandt (2002), in which the stabilising effect of the steady optimal streaks was shown to originate in the mean-flow distortion. That problem is revisited here, where access to the growth rates of the instability modes is provided through the eigenvalue spectra. The aim is to isolate the separate contributions of different aspects of the base flow, and demonstrate how non-linearity affects the inner mode. The total base flow is deconstructed, and the individual components are used as experimental base-flows in the stability problem. Although these base flows are aphysical, and not strictly solutions to the Navier-Stokes equations, they are a useful device to shed light on the effect of nonlinearity.

Firstly, the growth rate of the inner mode is shown in figure 4.12 for a base flow consisting of streaks, u_1, and a Blasius mean-flow, U_0, therefore neglecting the nonlinear mean-flow distortion. These results match those in figure 4.11 at $F = 0$. The growth rate increases steadily with streak amplitude, showing that streaks alone have a destabilising effect. This

is in line with the results of chapter 2, where the base flow was calculated with a linear method which naturally did not include the mean-flow distortion.

Having established the destabilising influence of steady streaks, the effect of nonlinearity in the streaks is investigated. Nonlinear streaks with the same frequency and wavenumbers but different amplitudes have slightly different shapes in the cross-stream plane owing to nonlinear interactions. These differences can bear on the stability of the inner mode, but normally it is difficult to assess the impact of this change in shape, because it is overwhelmed by the effect of changing the amplitude. In order to highlight the effect of nonlinear changes to the streak shape, the second specially constructed base flow neglects the mean flow distortion again, but includes streaks that have been scaled to a particular amplitude. For example in one case, the streak flow, u_1, for a streak with $A_u = 5\%$ is scaled up by a factor of four, and this allows for a comparison with the case for u_1 with a streak amplitude, $A_u = 20\%$. The difference in stability results must be due to alterations in the cross-stream profile of the streak, rather than A_u, since the amplitudes are scaled to match. In figure 4.12, the thin lines represent the growth rate of the inner mode calculated with base flows of this type. The amplitude to which the streaks were scaled is represented on the x-axis, and different lines are for streaks with different original amplitudes. The arrow in the figure indicates the direction of increasing original streak amplitude. The effect is monotonic, as the original streak amplitude increases, the growth rate of the inner mode decreases. Therefore, these results show that nonlinearity in the evolution of the base-flow streaks gives rise to a stabilising influence on the inner mode.

The third special base-flow to be considered consists of the distorted mean flow only, $u_2 = U_0$. The growth rate of the inner mode with this base flow is plotted in figure 4.12, versus the amplitude of the streaks in the calculation from which the distorted mean flow

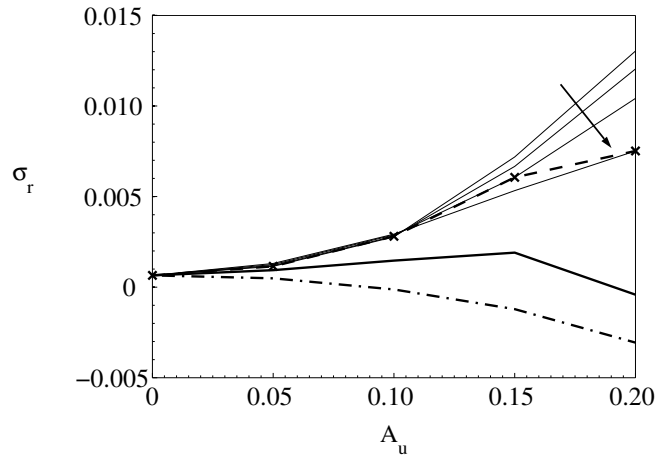

Figure 4.12: The growth rate of the inner mode, demonstrating the effect of amplitude and mean flow distortion with aphysical base flows with $F = 0$: — · —, no streaks, $u_1 = 0$, distorted mean-flow only; - - -, streaks, but no mean-flow distortion, $U_0 = U_{Blasius}$; thin lines ——, $U_0 = U_{Blasius}$ and each line is for a particular nonlinear streak, initially with different amplitudes, rescaled to amplitude A_u, the direction of the arrow indicates an increase in the original amplitude of the streak before rescaling; thick line ——, physical results with full base flow, unscaled u_1, and distorted mean flow.

was extracted. With this base flow, the mode is very stable, and the growth rate is lower with mean flows from calculations with higher amplitude streaks. Therefore as the mean flow distortion increases, its stabilising effect also increases. This is explained in terms of the wall normal curvature of the mean flow, U_0. Blasius flow can be thought of as almost inflectional, because moving toward the wall, the curvature increases from a negative value right up to zero, almost changing sign. Inviscid theory therefore hints at marginal stability, but as is well known, viscous effects lead to the slightly unstable TS wave for some Reynolds numbers. As the streaks are introduced and increased in amplitude, the curvature of U_0 becomes less close to zero at the wall as shown in figure 4.13. Therefore as the streak amplitude is increased, the mean flow becomes further from being inflectional, and the corresponding discrete instability is more damped.

In summary, the original calculations with the full base flow exhibited the net effects of conflating influences from the streaks and the mean flow. The initial increase in the

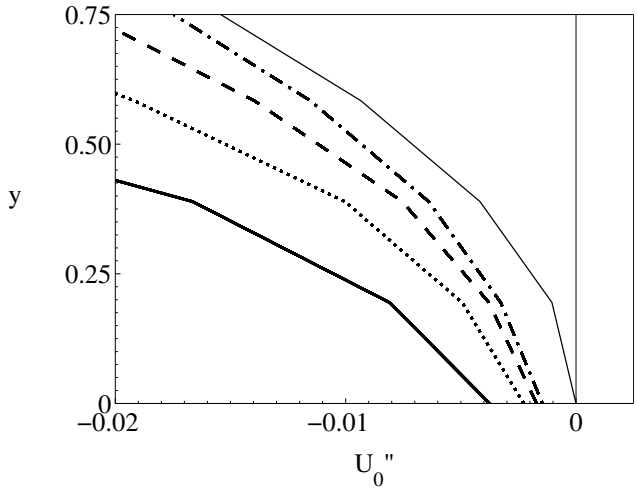

Figure 4.13: The effect of streak amplitude A_u on the near-wall curvature of the mean flow U_0, for steady streaks. The lines represent different amplitude streaks: ——, $A_u = 0$; — · —, $A_u = 5\%$; - - -, $A_u = 10\%$; · · · ·, $A_u = 15\%$; ——, $A_u = 20\%$.

growth rate of the inner mode with A_u, followed by a stabilisation at higher A_u can be explained in light of the preceding investigation using special aphysical base flows. The results in figure 4.12 show that the initial destabilisation is due to the streaks themselves, but the subsequent decrease in the inner mode's growth rate at high A_u is due to two factors: the streaks slightly losing their capability to destabilise the inner instability due to nonlinear changes in their shape; and, the increased damping influence of the mean-flow distortion. For the case of steady streaks presented here, there is a subtle balance between two relatively weak effects on the growth rate of the inner mode. However, for unsteady streaks with strong inflection points discussed in 4.3.3 the destabilisation effect is much greater.

4.4 Outer mode

The outer mode was introduced in chapter 2, and it is also captured here in the analysis of nonlinear streaks, using the subharmonic expansion in the spanwise direction. The difference

between the outer mode and the inner mode is made immediately clear by examining the structure of the former in the cross-stream plane, as shown in figure 4.14. The outer mode is a streak instability, and the contours of u_3, v_3, and w_3 in figure 4.14 show that the two-dimensional component is absent in the outer mode. Comparing figures 4.6 and 4.14 shows that the spanwise wavelength of the outer mode is twice as long as the inner instability. This is due to the subharmonic nature of the outer mode.

Very little of the outer mode's energy is located low down in the boundary layer. Instead it is contained in concentrated packets in the spanwise and wall-normal directions, away from the wall. For the streamwise and wall-normal velocities, the disturbance energy was centred on the flanks of the streaks, where the maximum spanwise shear in the mean flow was located. This is in line with previous studies of streak instabilities, for example by Andersson *et al.* (2001), and the assertion in chapter 2 that the outer mode was driven by spanwise shear (see also figure 2.26).

The w-component of the outer mode is dominated by the $1/2k_z$ wavenumber and, due to the symmetry, it is focused on the streak itself. It has a considerable amplitude compared with the other components. This spanwise disturbance which oscillates in the streamwise direction can be related to observations of streak instability in plan-views from experiments (for example Matsubara & Alfredsson, 2001; Mans *et al.*, 2007). Also, the spanwise oscillations identified as streak instabilities in the DNS of Brandt *et al.* (2004) had a streamwise wavenumber of $\alpha^* L_B^* = \{0.35, 0.75\}$ which compares well with the outer mode, for which the most unstable wavenumber, $\alpha^* L_B^* \sim 0.5$.

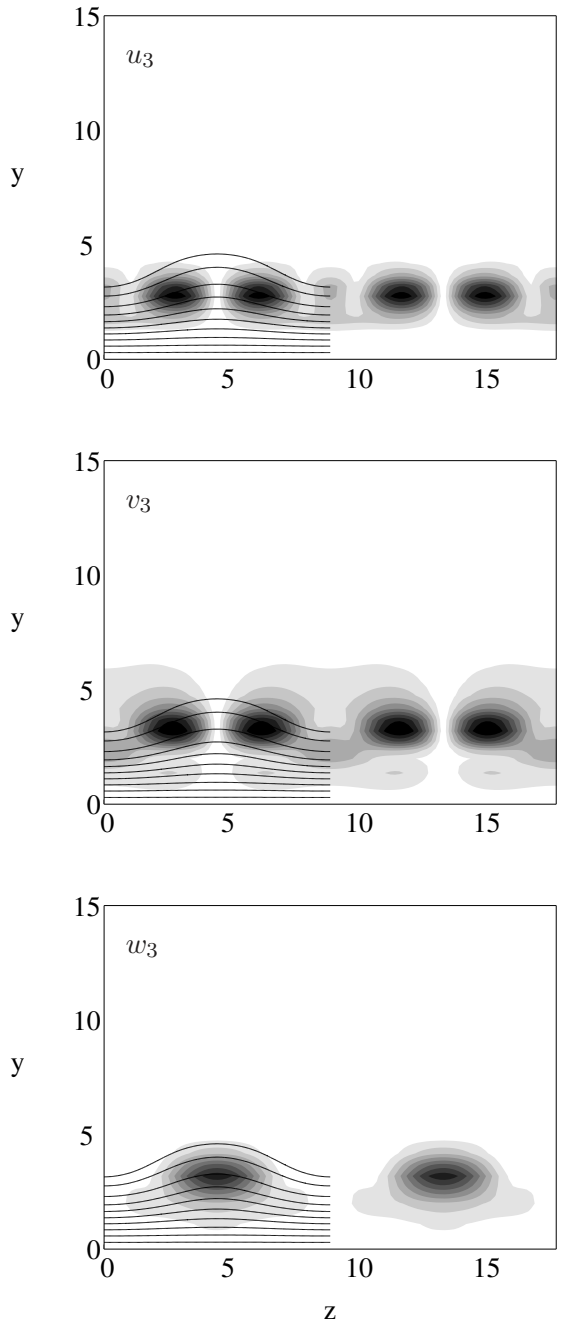

Figure 4.14: Filled contours of the three velocity components of the outer mode, plotted in the cross-stream plane for a streak with $A_u = 10\%$, $F = 30$. Root-mean-square values, with time averaging are presented. The contour levels are: $0 \leq u_3 \leq 1.75$, $0 \leq v_3 \leq 0.5$, $0 \leq w_3 \leq 1.75$. The unfilled contour lines correspond to a particular phase of the base flow, $u_2 = \{0.1, 0.2, \ldots, 0.9, 0.95\}$.

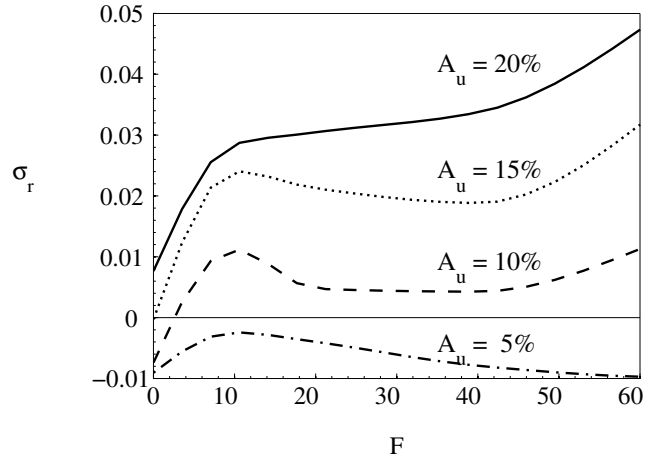

Figure 4.15: The effect of streak frequency and amplitude on the growth rate, σ_r of the outer mode. The lines represent different amplitude streaks: —·—, $A_u = 5\%$; - - -, $A_u = 10\%$; · · · ·, $A_u = 15\%$; ——, $A_u = 20\%$.

4.4.1 Growth rate characteristics of the outer mode

For a given streak frequency, the outer mode becomes unstable as the streak amplitude is increased, and the growth rate continues to increase as A_u is raised higher. This behaviour, and the comparatively modest dependence on the streak frequency are shown in figure 4.15. Low-amplitude streaks with $A_u = 5\%$ are not unstable to the outer mode, and increasing the frequency with this small amplitude modulation shows a small stabilising influence, familiar from the inner mode and the work of Grosch & Salwen (1968). On the whole, the results are similar to the preliminary calculations for linear streaks, but extending down to $F = 0$ shows that the outer mode is significantly more stable for steady streaks.

Along similar lines to the discussion for the inner mode, there are two aspects to the dependence of the outer mode growth rate on the streak frequency. The constant streak amplitude case is set out in figure 4.15, but this neglects the propensity of lower frequency streaks to amplify more strongly. Holding the amplitude of the forcing vortical mode, A_v, constant, the growth rate of the outer mode was re-evaluated at different streak frequencies with $A_u(F; A_v)$, and presented in figure 4.16.

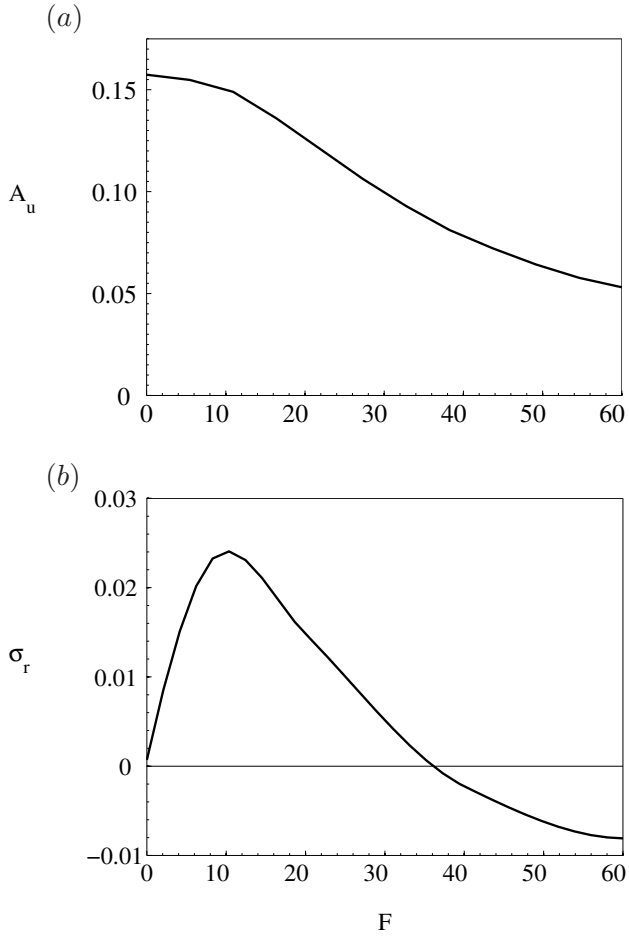

Figure 4.16: (a) The dependence of streak amplitude A_u on F, when $A_v = 4.5 \times 10^{-3}$ is held constant. (b) Growth rate of the outer mode versus the streak frequency at constant A_v.

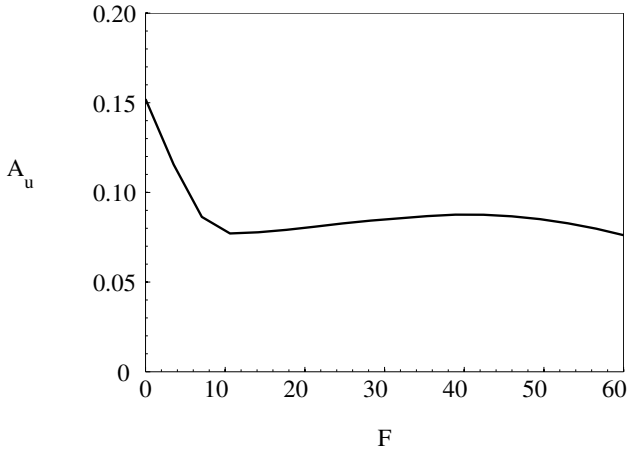

Figure 4.17: Dependence of the critical streak amplitude for the outer instability on streak frequency.

Similar to the inner mode, an optimum streak frequency emerges in the low end of the range. The streaks had an amplitude of $A_u = 15.74\%$ at $F = 0$, so they were barely unstable, but as the frequency was increased from zero, they were rapidly destabilised due to the effect of unsteadiness. However, beyond $F \sim 10$ the growth rate declines sharply due to the reduction in $A_u(F; A_v)$, because the outer mode depends strongly on A_u.

The critical amplitude of the outer mode, first calculated in the preliminary analysis was re-evaluated for the non-linear streaks, and the results are shown in figure 4.17. The critical amplitude for unsteady streaks is $A_u \sim 8\%$ which agrees with the experimental observations cited previously more closely than the threshold 26% calculated by Andersson *et al.* (2001). The critical amplitude computed herein does not depend strongly on frequency beyond $F > 10$, but the results in figure 4.17 include the limit $F = 0$, for which the critical amplitude increases to 15.2%. This is higher than for most of the frequency range of unsteady streaks, yet still lower than Andersson *et al.* (2001) proposed.

4.4.2 Comparison of the results at $F = 0$ to a previous analysis

Since the base flow is steady in the case of streaks with $F = 0$, and accounts for non-linearity, a more accurate comparison can be drawn with the results of Andersson *et al.* (2001) than in the preliminary analysis. Andersson *et al.* (2001) calculated the base flow for their stability analyses with DNS, as is the case here. However, the concept behind the initial perturbations chosen to stimulate the streaks differs between the two approaches. Andersson *et al.* (2001) used the perturbations which were optimised to cause the maximum growth of energy downstream. These perturbations consist of streamwise vortices sitting inside the boundary layer with $k_z = 0.636$. Although these perturbations provide an upper bound of possible non-modal amplification, they cannot be linked to free-stream turbulence. The present base flow is, however, calculated from the evolution of an oblique vortical free-stream mode, modelling one Fourier mode of the FST. The mode was chosen to reflect natural conditions of bypass transition. As pointed out by Leib *et al.* (1999), the evolution of disturbances downstream is rather sensitive to the initial perturbations, and the resulting streaks were quite different from those calculated by Andersson *et al.* (2001).

Contours of the base flow u_2, used in the stability analysis by Andersson *et al.* (2001), are presented in figure 4.18(a), for a streak amplitude of 20.2%. In panel (b), the base flow from the present analysis with $A_u = 20\%$ is illustrated. The shape of the disturbed contour lines is clearly different between the two. Since the spanwise shear of the base flow, $\partial u_2/\partial z$, is decisive for the outer mode, contours of this quantity are illustrated in figure 4.19.

Due to the higher spanwise wavenumber for the streaks considered here, the spanwise shear is significantly higher than for the 'optimal' streaks, even for the same streak amplitude. Though the increased spanwise shear may not be the only influential difference, it is not surprising that the critical amplitude of the streak velocity for the outer mode is lower

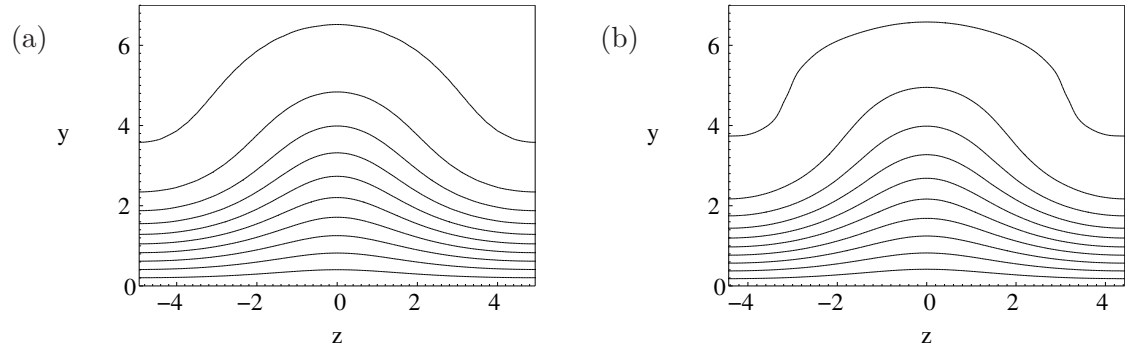

Figure 4.18: Contours of the total streamwise base flow, $u_2(y,z)$ for steady streaks at amplitude $A_u = 20\%$. The contour levels correspond to $0 < u_2 < 1$ with an increment of 0.1. The figure at left shows the base flow profile kindly provided by Dr. L. Brandt. It is obtained from DNS of the linearly-optimal streaks, at the location of maximum streak amplitude (Andersson *et al.*, 2001). The streaks at right are due to free-stream vortical forcing, and are extracted at $R = 360$, $k_y = 0.677$, $k_z = 0.71$, based on the local Blasius length scale.

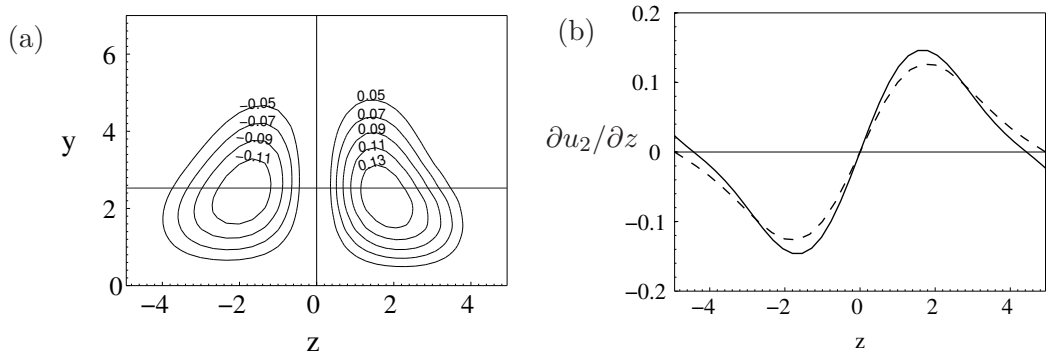

Figure 4.19: (a) Contours of the spanwise shear for the velocity fields in figure 4.18. The left half of the figure corresponds to the streaks by Andersson *et al.* (2001). The right half corresponds to the streaks forced by free-stream vortical modes. (b) The spanwise shear at the $y-$location marked with a line in panel (a). Streaks by Andersson *et al.* (2001), (- - -); streaks forced by free-stream vortical modes (——). The $y-$location selected corresponds to the critical layer of the outer mode.

in the present analysis than the previous estimate by Andersson *et al.* (2001).

4.4.3 Effect of unsteadiness in the base flow and mean-flow distortion on the outer mode

The foregoing analysis of the outer mode has considered all phases of the unsteady base flow with a global Floquet solution. In order to dissect the effect of frequency, quasi-steady analyses were also conducted. Using a subharmonic Floquet expansion in spanwise wavenumbers, the growth rate of the outer mode for the most unstable phase of the base flow is plotted in figure 4.20(a). The growth rate for the most stable phase of the base flow is also shown for streaks with $A_u = 10\%$. It should be noted that a stable phase could always be found for the entire frequency range, which again affirms the importance of accounting for all phases of the base flow. However, by considering quasi-steady base flows, the effect of streak frequency which is exerted through the shape of the streak profile is isolated, as opposed to including the actual undulation of the streaks. The spanwise wavenumber and streak amplitude is held constant for each line in figure 4.20(a). Based on the previous finding that the outer mode depends strongly on the spanwise profile of the base flow, the change in growth rate with F is somewhat surprising. The conclusion is that, in addition to spanwise shear, part of the destabilising effect of the streaks is indeed due to their wall-normal profile.

Furthermore, the influence of the nonlinear mean-flow distortion was investigated by replacing the mean flow with the Blasius solution, $U_0 = U_{Blasius}$, and recalculating the growth rates. The results are plotted in figure 4.20(b), and though there is some difference to figure 4.20(a), the results are not qualitatively changed, which is in line with the identification of the outer mode as a streak instability, rather than one which originates in the

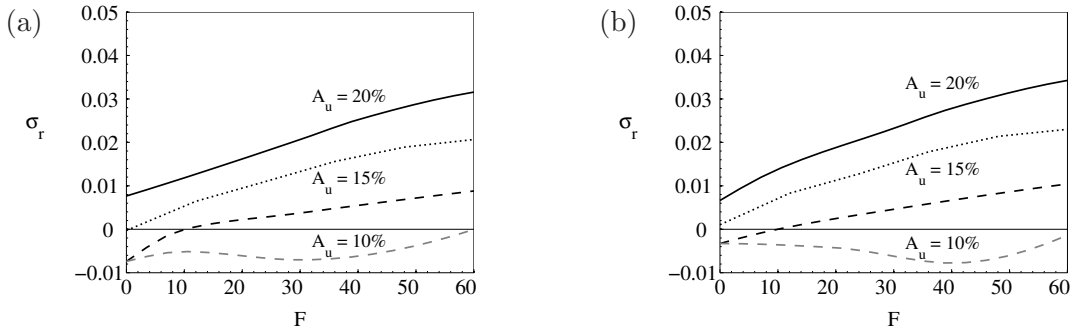

Figure 4.20: The effect of streak amplitude and frequency on the outer mode. The most unstable phase of the unsteady streaks is used in a steady analysis. In (a), the mean flow is modified from Blasius due to nonlinear effects of the streak; in (b) the Blasius profile is used. ——, $A_u = 20\%$; · · · ·, $A_u = 15\%$; - - -, $A_u = 10\%$. The growth rate for the most stabilizing phase of the base streaks is also shown (— · —) for $A_u = 10\%$.

distorted mean flow U_0.

4.5 Mode competition

In the preceding sections, the discussion has focused on the inner and outer modes separately. However, a comparison between the growth rates of the two instabilities could be insightful, such as that presented in figure 4.1 for steady streaks. In that case, for low streak amplitudes, the inner mode was the only instability even though it was inappreciably modified from the TS wave. Above $A_u = 15\%$, the outer instability emerged, and dominated over the inner mode. For unsteady streaks with $F = 10$, a similar switch-over occurs, as the streak amplitude is increased, shown in figure 4.21(a). In this case, the inner instability is not stabilised at high A_u as it was for $F = 0$, because the unsteady streaks' destabilising influence outweighs the effect of the mean flow distortion. However the outer mode is also more unstable than it was for $F = 0$. Its growth rate surpasses that of the inner mode around $A_u = 10\%$, and σ_r continues to increase with A_u. The switch in the dominant mode, which occurs as the amplitude of the streaks is increased, can be linked to bypass

transition: Where the streaks play little role, the dominant instabilities have their origin in TS waves, but as the Klebanoff distortions are intensified, the streak instability takes over.

The growth rate of the most unstable mode is plotted versus F in figure 4.21(b). The boundary layer becomes more unstable as the amplitude and frequency are increased, almost monotonically. However, this overarching trend hides the underlying mode competition: with low-frequency streaks, the outer mode dominates except for small A_u, but as the frequency of the streaks is increased, the growth rate of the inner mode actually exceeds the outer mode for all amplitudes.

Based on the above results, either the inner mode or the outer mode can be the most unstable, and it is decided by the parameters of the streaks. From figure 4.21(b), it would appear that the inner mode dominates over the outer instability for most of the parameter space. However, this is partly an artefact of holding A_u constant while varying F. In figure 4.22, the dependence of streak amplitude on its frequency, $Au(F; A_v)$, is taken into account, and the previous data from figures 4.5 and 4.16 are represented on one set of axes. This reveals that the outer mode has a higher maximum growth rate in the low frequency range, where the instabilities are most rapidly amplified due to the combined effects of streak unsteadiness and high amplitude. However, the inner mode is unstable for a larger range of streak frequencies, $0 < F < 45$. From the linear stability results alone, it is not clear which of the two instabilities is likely to dominate in bypass transition, and both are quite possible.

4.6 Direct numerical simulations

Direct numerical simulations of the inner and outer instabilities are reported in the following sections. Having established in previous DNS that the inner and outer mode can both

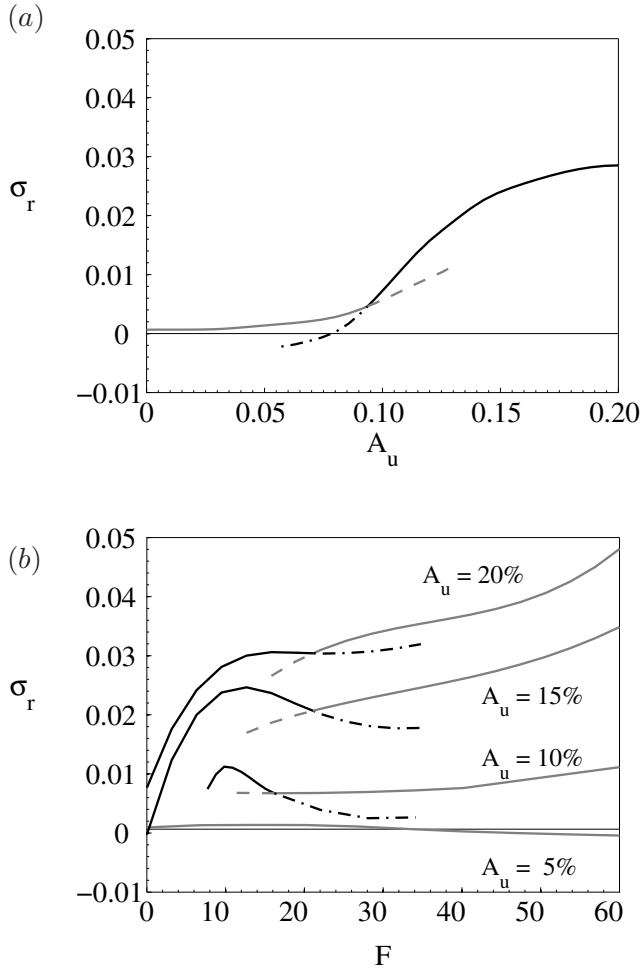

Figure 4.21: The influence of unsteady streaks on the growth rate of the most unstable mode. (a) The growth rate is plotted versus A_u for a base streak with $F = 10$. (—— light line) inner mode; (—— dark line) outer mode. (b) The growth rate is plotted versus streak frequency, at streak amplitudes $A_u = \{0, 5, 10, 15, 20\}\%$. In ($a$), the $\sigma_r = 0$ line is marked by the horizontal line, and in (b), the growth rate of the TS wave for the Blasius boundary layer is marked.

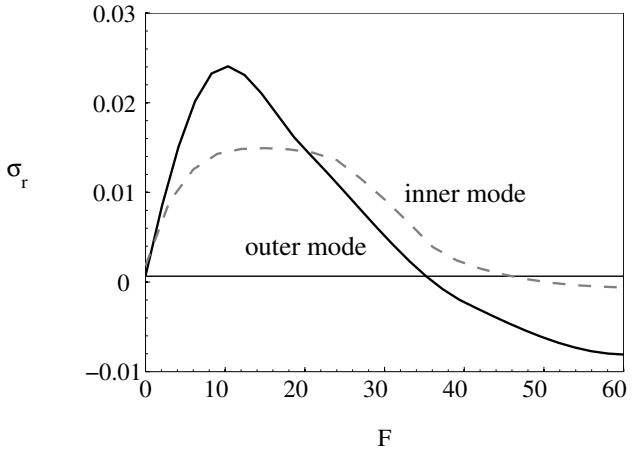

Figure 4.22: The growth rate of the inner (– – –) and outer (——) modes versus frequency, F. The level of upstream forcing for the streak, $A_v = 4.5 \times 10^{-3}$, is held constant, therefore the steak amplitude also varies with F as shown in figure 4.5(a). The growth rate of the TS wave for the Blasius boundary layer is marked by the horizontal line.

grow and cause transition, the emphasis here is on providing a view of the structure of the instabilities, and their nonlinear breakdown to turbulence. The three-dimensional, incompressible Navier–Stokes equations are solved using the numerical algorithm described chapter 2.

In terms of Reynolds number, the computational domain spans $163 \leq R \leq 628$. The inflow plane is therefore at the same location as the simulations in Jacobs & Durbin (2001), and the simulations in chapter 3 used to calculate the base flow for the stability analysis. The critical Reynolds number for the TS instability is contained within this domain, although the exit plane is well upstream of the location where natural transition would be complete. As for the DNS reported in chapter 2, the inlet boundary layer 99% thickness δ_o is used as the characteristic lengthscale, and the size of the computational domain with this scaling is $460 \times 20 \times 24$ in the streamwise, wall-normal, and spanwise directions, respectively. Like the simulations in 2.4 the domain contains six spanwise wavelengths of the streak. The number of grid points in these directions is $2049 \times 129 \times 129$. The grid is uniform in the

streamwise and spanwise coordinates, but is stretched in the wall-normal direction. The resolution is similar to the DNS by Jacobs & Durbin (2001), who performed an extensive grid refinement study. Based on wall units, the maximum grid spacings are $\Delta x^+ = 8.1$, $\Delta y_w^+ = 0.4$ and $\Delta z^+ = 6.8$ where Δy_w^+ is at the wall.

At the inlet to the simulation domain, in addition to the Blasius profile, two perturbations are prescribed. The first is the same disturbance as in chapter 3, i.e. a low-frequency, vortical mode which leads to the generation of a high-amplitude streaks inside the boundary layer. Therefore, the boundary layer streaks in the current simulations are the same as those adopted in the stability analyses. The second disturbance is an inner or outer instability mode obtained from the Floquet analysis in sections 4.3 and 4.4.

The inflow condition is therefore,

$$\begin{aligned} \boldsymbol{v}_0(y,z,t) = \boldsymbol{v}_B(y) \quad &+ \quad A_v \mathrm{Real}\left\{u_1(y,x_o)\cos(k_z z)e^{i(-\omega t)}\right\}\mathbf{e}_x \\ &+ \quad A_v \mathrm{Real}\left\{v_1(y,x_o)\cos(k_z z)e^{i(-\omega t)}\right\}\mathbf{e}_y \\ &- \quad A_v \mathrm{Imag.}\left\{w_1(y,x_o)\sin(k_z z)e^{i(-\omega t)}\right\}\mathbf{e}_z \\ &+ \quad A_s \sum_n \sum_m \mathrm{Real}\left\{\boldsymbol{v}_{m,n}(y)e^{i([nk_z+\gamma]z+[m\omega+\sigma_i]t)}\right\}. \end{aligned} \tag{4.1}$$

Based on the results of linear theory (figures 4.21*a* and *b*), the outer mode dominates for relatively low streak frequencies, and the inner instability is most pronounced at the higher frequencies. Therefore, streaks with frequency $F = 30$ were used in the simulations of the outer mode, and $F = 60$ for the inner mode. The spanwise wavenumber of the streaks remained unchanged, $k_z = 0.71$ based on the Blasius length scale at the target Reynolds number ($k_z = 1.57\delta_o$). The value of A_v was adjusted such that the root mean square streak disturbance was 10% at the target Reynolds number.

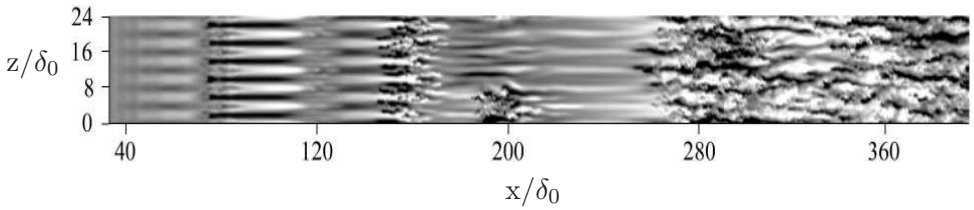

Figure 4.23: Contours of the $u-$perturbation velocity ($-0.10 \leq u \leq 0.10$) inside the boundary layer. The plane is $y/\delta_o = 0.6$, where δ_o is the boundary layer thickness at the inlet plane.

4.6.1 The inner mode

The interaction of the inner instability mode with the streaky boundary layer leads to transition to turbulence in the simulations. Transition onset is observed near $x/\delta_o \approx 150$, which corresponds to $R = 383$, and is therefore slightly downstream of the target Reynolds number for the stability analyses. This suggests that the secondary instability of the streaks took place upstream, near the target Reynolds number, followed by spot inception and breakdown. A top view of the $u-$perturbation field inside the boundary layer is shown in figure 4.23. The top view shows the upstream laminar flow, a turbulent patch in the transition region, and the fully turbulent boundary layer near the exit of the domain. The inner instability is fundamental in the spanwise wavenumber of the streaks $\beta_n = nk_z$ (see equation 3.7). Therefore, the amplification of the secondary instability initially takes on a repeated pattern in the spanwise direction. As a result, breakdown can be repeated across the span, as seen near $x = 160$ in figure 4.23. However, irregular patterns of breakdown are also observed due to the non-linear nature of transition to turbulence, which can disrupt the spanwise homogeneity of the flow as seen near $x = 200$.

The events which precede the flow field in figure 4.23, are presented in figures 4.24 and 4.25. Each sequence spans the time period, $T - 100 < t < T - 20$, where T is the time of the final field in figure 4.23. The top views show contours of the $u-$ and $w-$perturbation velocities, respectively. They capture the amplification of the inner-mode instability and

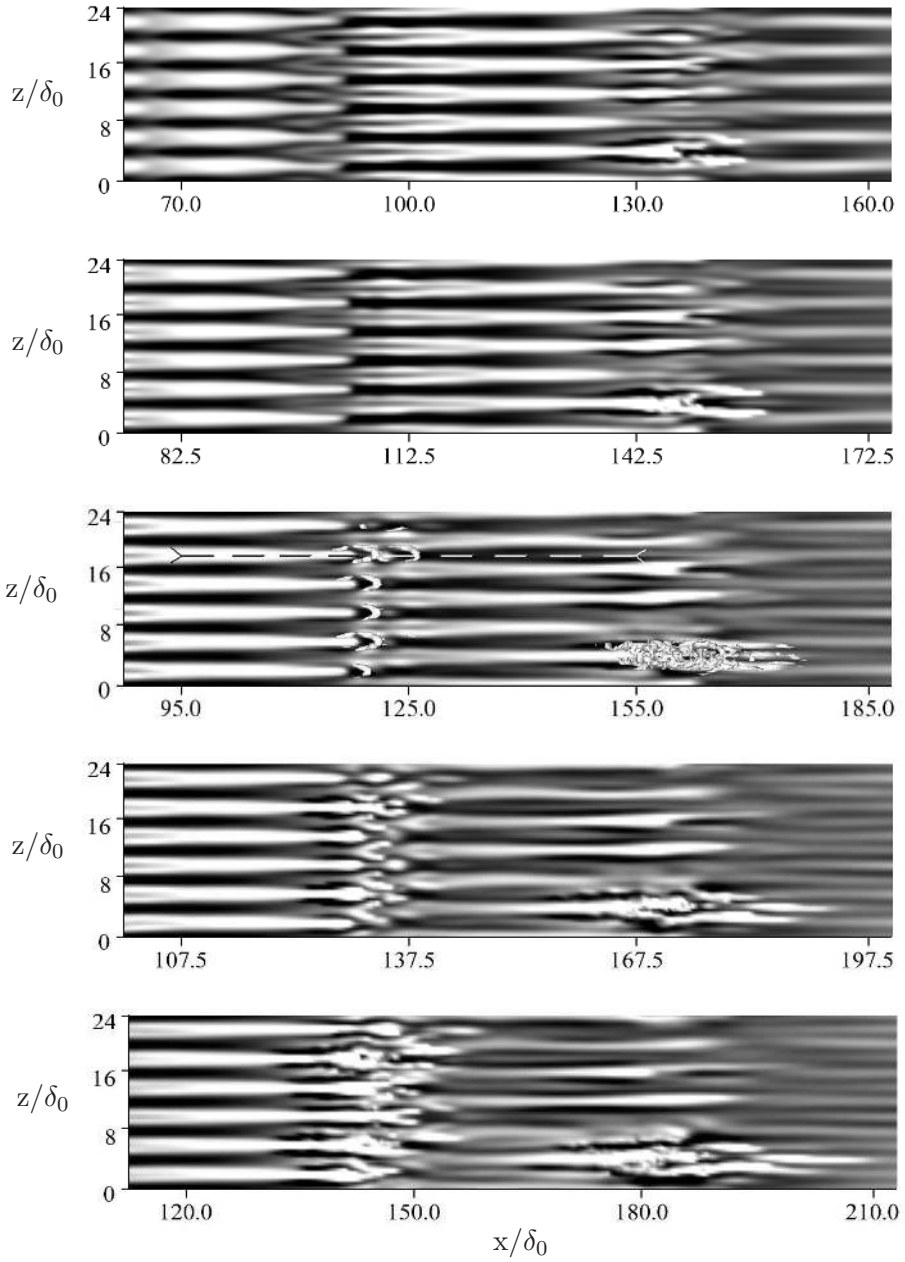

Figure 4.24: The $u-$perturbation velocity for the inner mode at $F = 60$, in the plane $y/\delta_x = 0.25$, where δ_x is the boundary layer thickness at $x = 125$. Contour levels are $-0.10 \leq u \leq 0.10$. The sequence spans the period $T - 100 < t < T - 20$, where T is the time instance in figure 4.23. The viewing window is translated at $0.625U_\infty$ in order to follow the development of the instability. In the middle pane, an iso-surface of $-\lambda_2$ is plotted.

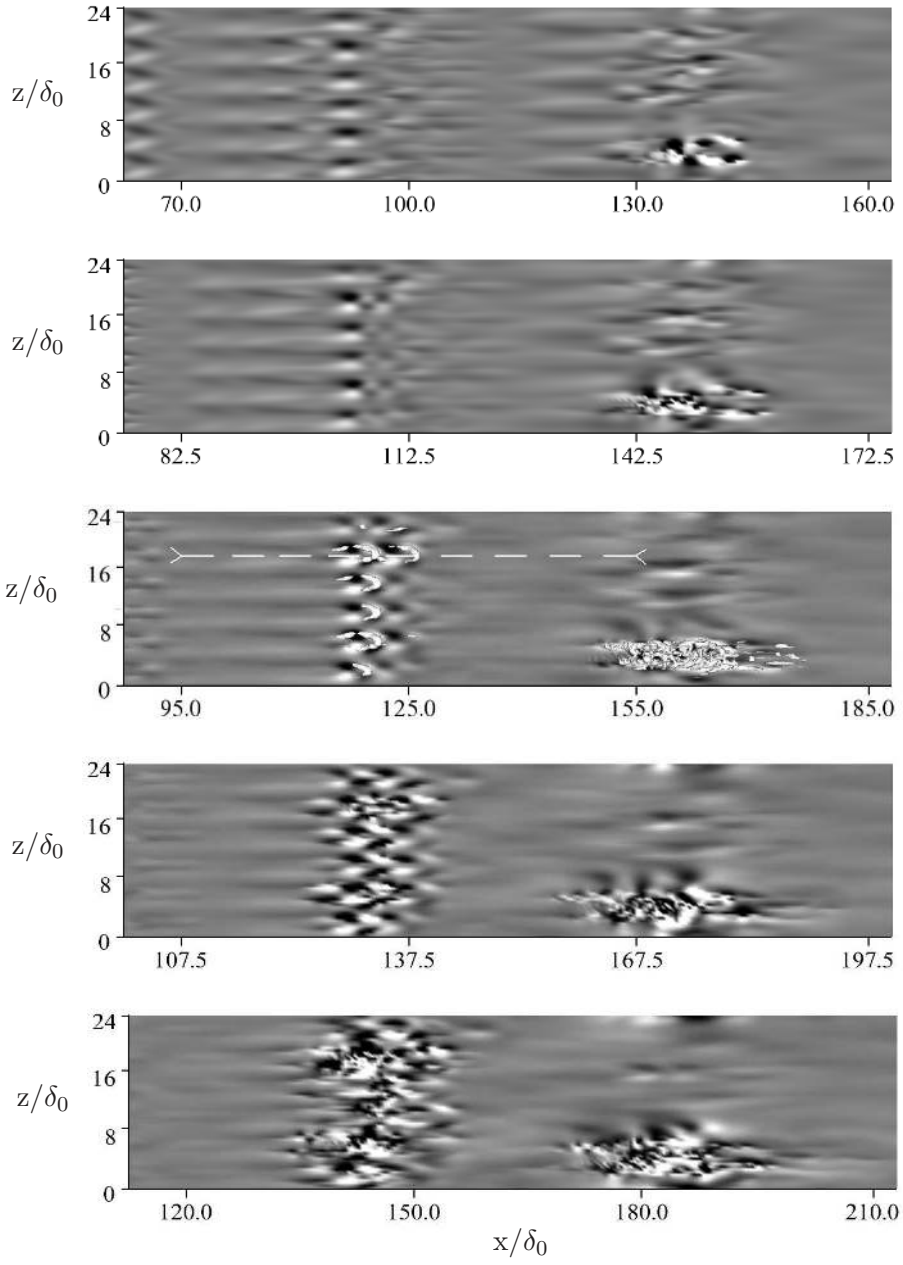

Figure 4.25: The $w-$perturbation velocity in the plane $y/\delta_x = 0.25$, where δ_x is the boundary layer thickness at $x = 125$. Contour levels are $-0.05 \leq w \leq 0.05$. The sequence spans the period $T - 100 < t < T - 20$, where T is the time instance in figure 4.23. The viewing window is translated at $0.625U_\infty$ in order to follow the development of the instability. In the middle pane, an iso-surface of $-\lambda_2$ is plotted.

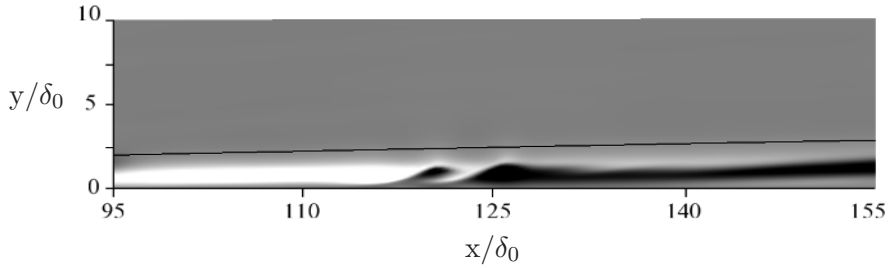

Figure 4.26: Contours of the $u-$perturbation velocity in the (x,y)–plane ($-0.1 \leq u \leq 0.1$). The side view is extracted along the dashed line in figure 4.24 and 4.25.

non-linear breakdown to turbulence. Near the inlet (not shown), the inner instability wave is traversed by many streaks due to their relative phase speeds. However, when the instability reaches high-amplitude, it is seen to amplify in the region near the overlap of the forward and backward streaks. The subdomains plotted in figures 4.24 and 4.25 translate in the downstream direction at $0.625U_\infty$. The inner instability retains the same relative position in the viewing window. Therefore, the phase speed of the inner instability at this stage of breakdown is in reasonable agreement with the Floquet results in section 4.6.1, but slightly exceeds the propagation speed of the wavepackets observed by Nagarajan *et al.* (2007), $c_r = 0.52 - 0.60U_\infty$.

Iso-surfaces of the λ_2 vortex identification criterion are shown at $t = T - 60$, in the middle frames of figures 4.24 and 4.25. Near $x/\delta_0 = 120$, Λ-shaped structures are observed at the intersection of the high- and low-speed streaks. They are narrow in the span and short in the streamwise direction, in comparison to the secondary instability of classical TS waves (Herbert, 1988). The Λ-structures are also distinct from those which emerge when two-dimensional TS waves are modulated by streaks (Liu *et al.*, 2008*a*). It was shown in section 2.3.1 that the inner mode reduces to the TS wave when u_1 vanishes. However, when u_1 is finite and unsteady, the Floquet analysis predicts that the inner eigen-mode deviates significantly from the classical boundary layer instability. It is no longer two-dimensional

and, more importantly, is not monochromatic in time. Instead, it has finite energy over a range of frequencies, $200 < F < 600$. The higher frequencies are similar to the properties of the wavepackets reported by Nagarajan *et al.* (2007) (see their table 6).

A side view of the boundary layer at time $t = T - 60$ is given in figure 4.26. The plane bisects the region where breakdown is initiated, and shows that the origin of the turbulent spot is at the intersection of the low- and high-speed streaks. The importance of this region was suggested by Brandt *et al.* (2004) based on their DNS. However, a formal explanation of the instability mechanism was not provided.

4.6.2 The outer mode

Direct numerical simulations of streaks perturbed by the outer instability were also carried out. An overview of the downstream evolution of the flow, as computed from the DNS, is shown in figure 4.27. Transition to turbulence took place in the DNS at streak amplitudes on the order of $10 - 15\%$. This amplitude is significantly lower than the threshold for instability predicted by the steady analysis of Andersson *et al.* (2001). The $u-$contours in the top pane of figure 4.27 clearly illustrate the streaks upstream of transition to turbulence.

A time sequence of the amplification of the outer mode and breakdown of the streaky boundary layer is shown in figure 4.28. The sequence spans $T-80 < t < T-20$, where T is the time instance in figure 4.27. The region shown translates downstream at $0.75U_\infty$ in order to maintain the instability in the middle of the frame. The plane view of the perturbation field does not clearly demonstrate the outer nature of the instability. Also, using vortex identification criteria, such as λ_2, did not yield any distinctive vortical structures during the breakdown of the streaks.

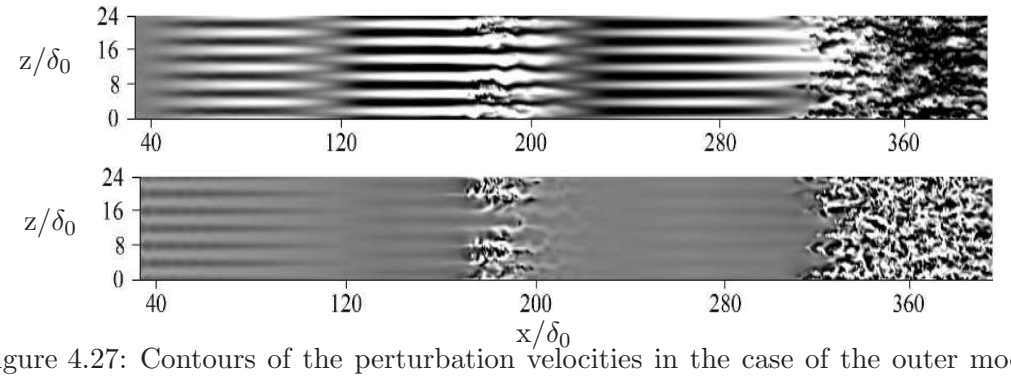

Figure 4.27: Contours of the perturbation velocities in the case of the outer mode: (top) $-0.10 \leq u \leq 0.10$; (bottom) $-0.01 \leq v \leq 0.01$. The plane is $y/\delta_o = 1.0$, where δ_o is the boundary layer thickness at the inlet plane.

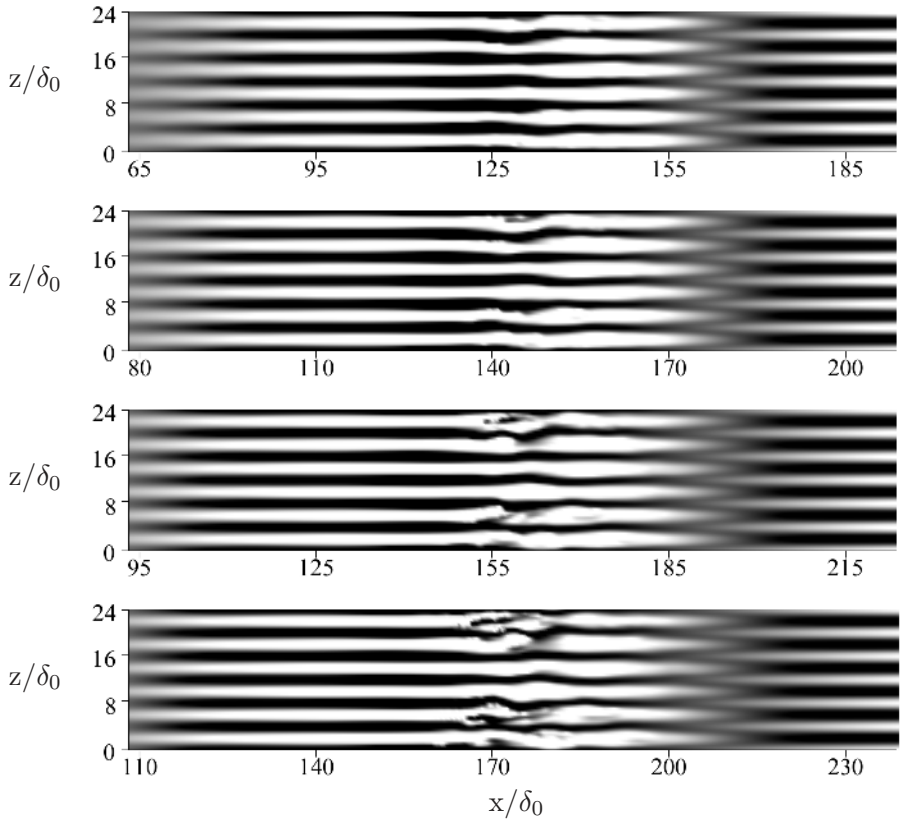

Figure 4.28: The $u-$perturbation velocity of the outer mode at $F = 30$, in the plane $y/\delta_x = 0.38$, where δ_x is the boundary layer thickness at $x = 140$. Contour levels are $-0.10 \leq u \leq 0.10$. The sequence spans the period $T - 80 < t < T - 20$ where T is the time instance in figure 4.27. The viewing window is translated at $0.75U_\infty$ in order to follow the development of the instability.

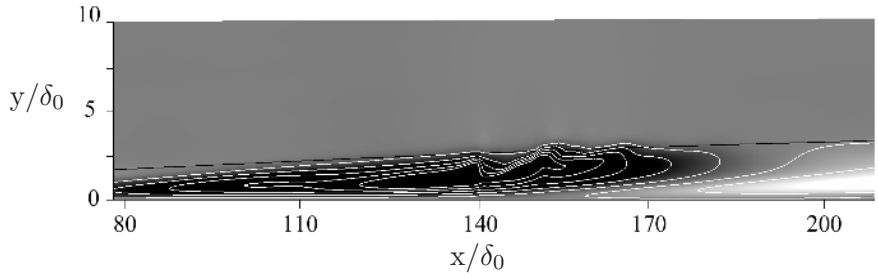

Figure 4.29: Contours of the $u-$perturbation velocity in the (x,y)–plane ($-0.1 \leq u \leq 0.1$). The side view is extracted $z = 8$, and corresponds to time, $t = T - 60$, in figure 4.28. The high frequency wave visible on top of the low speed streak is the outer mode.

Figure 4.29 shows a side view of the disturbance field at $t = T - 60$. The plane corresponds to $z = 8$ in figure 4.28. The contours of $u-$perturbation show that the low-speed streak and the secondary instability near the edge of the boundary layer. The flow pattern bears clear resemblance to the instabilities observed in previous simulations of bypass transition due to free-stream turbulence, in absence of a leading edge (Jacobs & Durbin, 2001; Brandt *et al.*, 2004). It also very closely resembles the instability reported by Zaki & Durbin (2005), where their streak was perturbed by a high-frequency free-stream mode.

Chapter 5

Conclusion

5.1 Discussion

The preceding chapter described two possible modes of instability which occur in a boundary layer perturbed by streaks. The DNS showed that they are each capable of growing to nonlinear amplitudes, and breaking down to turbulent spots which grow and merge into a fully turbulent boundary layer. Although the linear results showed that in a canonical setting the most unstable mode would be decided by the frequency and amplitude of the streak, the growth rates of the two modes were quite similar. In a realistic bypass transition scenario, receptivity could play a decisive role in selecting one of the two modes as the main precursor of turbulent spots.

This view is supported by the simulations of bypass transition with a leading edge conducted by Nagarajan *et al.* (2007). In that work, two distinct precursors to turbulent spots were noted, and the flow conditions decided which prevailed. With a sharp leading edge and the lower value of $Tu = 3.5\%$, transition occurred due to an instability at the edge of the boundary layer. Increasing the turbulence intensity or the bluntness of the leading edge caused a different type of spot precursor to prevail, which was situated closer

to the wall. This type of instability had not been seen in previous simulations for which the inflow plane was downstream of the leading edge, and the dependence on the leading-edge bluntness indicates that receptivity there was of key importance.

Kendall (1991), for example, also found that decreasing the aspect ratio of the leading edge caused an increase in the amplitude of near-wall instabilities, which has been attributed to enhanced receptivity. In that case, the FST was very weak and the instabilities were shown to be conventional TS waves, but the two types of turbulent spot precursors found under more severe turbulent conditions by Nagarajan *et al.* (2007) can now be associated with the inner and outer instabilities. Indeed, the instabilities discussed in chapter 4 closely resemble those leading to breakdown in the bypass simulations with a leading edge.

For instance the 'wavepackets' observed by Nagarajan *et al.* (2007) close to the wall around $y = 0.25\delta_{99}$ have an average phase speed of 0.52, and wavelength $\lambda_x \sim 5\delta_{99}$. The herein computed inner mode has a similar phase speed, and $\lambda_x \sim 3\delta_{99}$. The structure of the disturbances in figure 13 by Nagarajan *et al.* (2007) is also seen in the shape of the inner mode, obtained from the present linear stability calculations. A plan view of the inner mode is shown in figure 5.1 at $y = 0.276\delta_{99}$. A fundamental varicose pattern in the $u_1 + u_3$ contours captures the streamwise thinning and thickening of the low- and high-speed streaks, and their staggered pattern (figure 5.1*a*). The spanwise component of the mode is shown in figure 5.1*c*. An inclined chequered pattern in the streamwise and spanwise directions is a distinctive characteristic of the inner instability – see Nagarajan *et al.* (2007) figure 13*c* for comparison. A similar pattern was also reported in the DNS of the inner mode in chapter 4, particularly the fourth pane of figure 4.25. Note that in figure 5.1 the streamwise direction is normalised by the Blasius length scale, but in figure 4.25, x is nondimensionalised by the 99% thickness of the boundary layer at the inlet of the

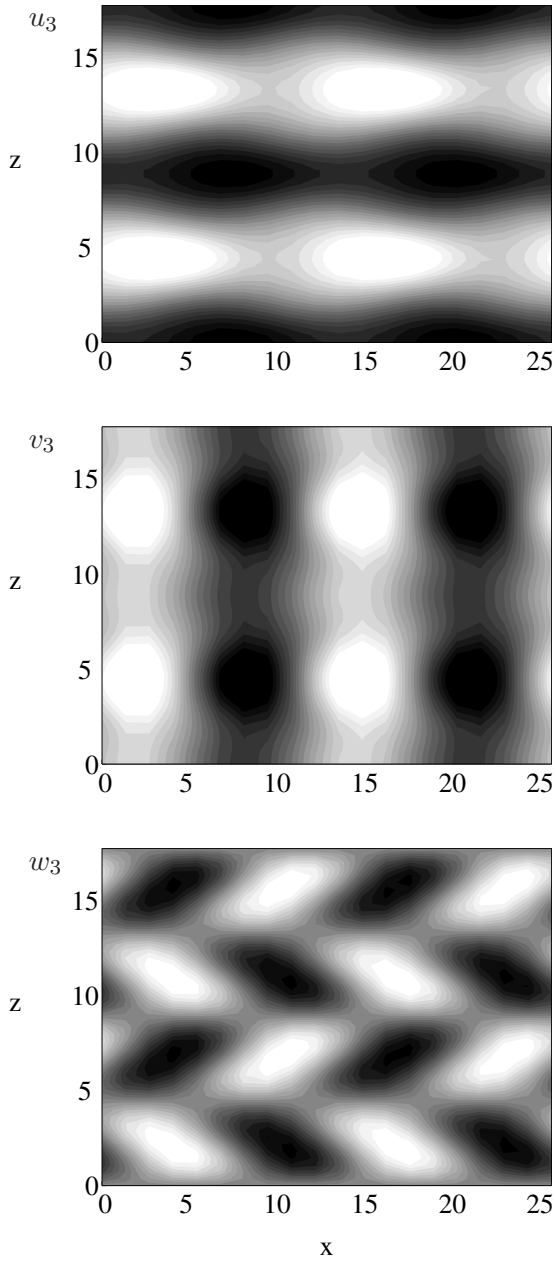

Figure 5.1: The inner mode for streaks with $A_u = 20\%$ and $F = 60$ in plan-view for a particular time point and $y = 1.36 = 0.276/\delta_{99}$, where δ_{99} is the laminar boundary layer 99% thickness: at top contours of $u_1 + u_3$; in the middle, v_3, at the bottom, w_3.

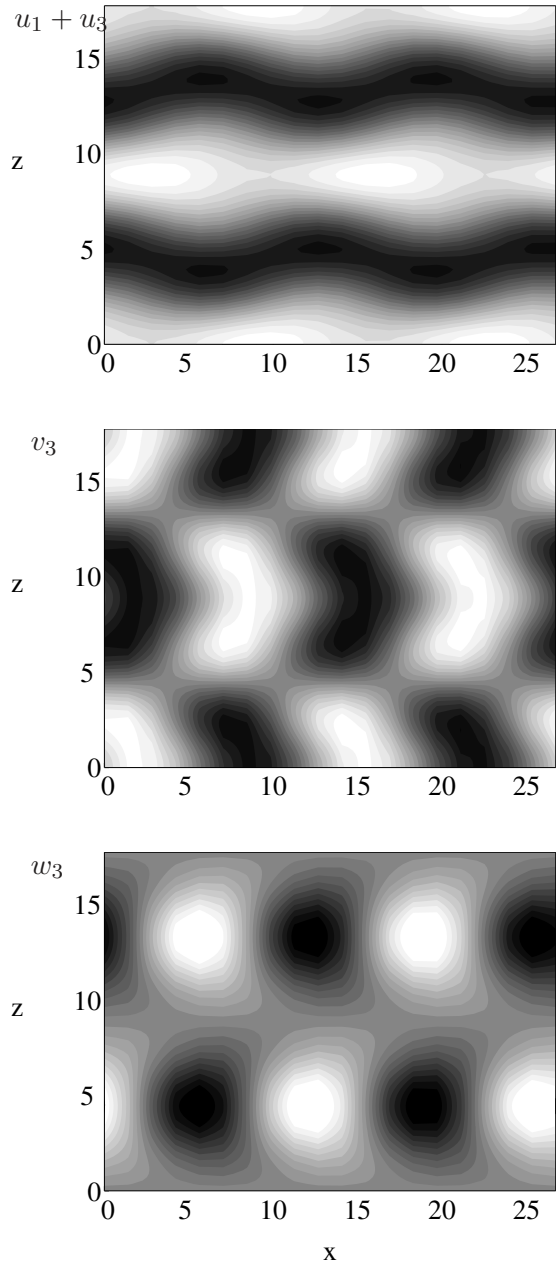

Figure 5.2: The outer mode for streaks with $A_u = 10\%$ and $F = 30$ in plan-view for a particular time point and $y = 2.75 = 0.558\delta_{99}$, where δ_{99} is the laminar boundary layer 99% thickness: at top contours of $u_1 + u_3$; in the middle, v_3, at the bottom, w_3.

simulation. In the DNS, around $x/\delta_0 = 135$, 15 units corresponds to 35 units in figure 5.1.

The simulations of Nagarajan *et al.* (2007) therefore affirm that the inner mode is a possible route to bypass transition in the presence of free-stream turbulence. However they also show that the inner instability only plays an active role if the level of turbulence is high enough to stimulate it, or an effective receptivity mechanism is present, such as a blunt leading edge. The present linear analysis emphasised that unsteadiness in the base flow is vital for the inner instability, due to the formation of inflectional velocity profiles. This is also borne out in observations of the inner mode from experiments and simulations which include turbulent free streams (for example Kendall, 1991; Nagarajan *et al.*, 2007), that naturally stimulate unsteady streaks. In fact the experimental investigation of bypass transition by Mandal *et al.* (2010) using particle image velocimetry showed instantaneously inflectional profiles which they associated with varicose instabilities, such as the inner mode. Although the role of the inner and outer mode in the self-sustainability of turbulent boundary layers is somewhat speculative, on the basis of 4.21, a scenario involving both modes could be imagined: Low frequency FST exciting the outer mode at the edge of the boundary layer could lead to transition but once sufficient unsteadiness was present closer to the wall the inner mode could become significant for sustaining the turbulence via a continual formation and breakdown of unsteady streaks.

It is not surprising that the simulations of Cossu & Brandt (2002) only exhibited the stabilising effect of streaks on TS waves, because their base flow was steady. From the linear stability standpoint Cossu & Brandt (2004) made a similar finding. Goldstein & Sescu (2008) accounted for unsteadiness of the streaks and hence were able to address the inner instability found in the simulations by Nagarajan *et al.* (2007). Their analysis linked the instability to inflection points of the base flow, which they attributed directly to

unsteadiness. However, the linear stability equations in that study were two-dimensional, so spanwise and temporal variations in the base flow were neglected. The validity of this assumption can certainly be questioned given the well known spanwise scale of streaks and their high amplitude. The phase speed calculated by Goldstein & Sescu (2008) was approximately $0.2U_\infty$, which is much lower than in the simulations of Nagarajan *et al.* (2007). The discrepancy was attributed to the two-dimensionality of their result. The DNS in chapter 4.6.1 supports their explanation: the three-dimensionality of the inner instability is evident, for example in figure 4.25, in the contours of w-perturbations. Furthermore the stability analysis by Goldstein & Sescu (2008) was inviscid, which obscured the link between the inner mode and the TS wave. In contrast, the analysis presented herein did account for viscosity, unsteadiness, and spanwise variation in the base flow.

The outer mode, on the other hand, can be compared to the spot precursors found by Jacobs & Durbin (2001), and also reported by Nagarajan *et al.* (2007) when the leading edge was slender. This type of instability occurs close to the edge of the boundary layer, when the lifted low-speed streaks are perturbed by eddies from the free stream. Nagarajan *et al.* (2007) showed that the spanwise disturbance for this breakdown mechanism is maximum near the free stream, and weak close to the wall. This is in line with the current appellation of the 'outer mode': for example figure 4.14 showed that most of the outer mode's energy is high in the boundary layer. As such, this type of instability is most receptive to free-stream forcing. The mode shapes from the present linear theory also reproduce the structure of the instability recorded by Nagarajan *et al.* (2007) in their figure 10. Contours of the outer mode velocity components are shown in a plan view in figure 5.2. Panel (a) shows the subharmonic, sinuous oscillations of the low-speed streaks. The corresponding spanwise disturbance velocity, has the form of patches of high- and low-amplitude w_3 which alternate

in the streamwise direction (figure 5.2*c*).

Despite the similarities between both types of spot precursor identified by Nagarajan *et al.* (2007) and the present findings from linear theory, there is an important difference which can be traced back to the assumptions used in setting up the stability problem. The global Floquet modes reported in chapter 4 imply a periodic velocity disturbance which, within the theoretical framework, extends infinitely in the spanwise direction. Obviously the breakdown scenarios shown by Nagarajan *et al.* (2007) are more localised, which could be due to heterogeneity in the underlying streaky boundary layer, or local peaks in the forcing from the FST (Hernon *et al.*, 2007). However, it is encouraging to note that the theoretical estimations concur relatively well with the observed instability waves, at least within the spatial constraints of the wavepackets.

Another important assumption behind the linear stability method, particularly the choice of Floquet theory to account for the base flow unsteadiness, is that the instabilities remain linear for the duration of a period of the base flow. That is, the instabilities do not grow so much that nonlinear effects take hold before the base flow completes one cycle. The validity of this depends on the initial amplitude of the growing wave, and hence local receptivity (Luo & Wu, 2010). This is however beyond the scope of linear instability theory, and hence the main body of work presented here. Within the linear framework, the only rigorous way to account for a periodic base flow is with Floquet theory, but if nonlinear growth is physically important then it can reasonably be assumed that this growth will occur during the phases of the base flow which are most unstable. The initial linear growth of instabilities would therefore be described by the results from quasi-steady analyses for the inner and outer modes, presented in chapter 4. However, the influence of unsteady streaks on the boundary-layer stability, be it stabilising or destabilising, is not affected by

the quasi-steady assumption, and the main effects are included in the following summary.

5.2 Summary

In this work, the stability of the flat-plate boundary layer, distorted by unsteady streaks, has been studied. A canonical model of the base-flow was developed in order to make the problem tractable for a secondary-stability method. This section presents a summary of the method and findings.

The model base-flow was formulated by forcing the boundary layer with a particular Fourier component of free-stream turbulence. The unsteady three-dimensional perturbations of vorticity in the free stream penetrated into the boundary layer and resulted in distortions of the streamwise velocity which resembled streaks. They were calculated (a) in a linear setting for a preliminary analysis, with the Orr-Sommerfeld - Squire pair; and (b) using DNS, thus taking nonlinear and nonparallel effects into account. In both the linear and nonlinear calculations, the parameters of the base flow were chosen to reflect the conditions around the onset of transition observed in experiments and simulations of bypass transition.

The secondary-stability equations for linear perturbations to the streaky base-flow were derived and solved. Floquet theory was invoked in two dimensions to account for the periodic base-state. A numerical algorithm solved the temporal eigenvalue problem for the complex frequency σ, using a Chebyshev expansion in the wall-normal direction. The real part of σ represented the growth rate of the instabilities.

— The most unstable modes were sought and two modes of instability were identified: the 'inner' mode, which could be linked to the TS wave; and the 'outer' mode which was a streak instability.

— The stabilising effect of streaks on TS waves, familiar from similar work by Cossu & Brandt (2004), was found only in the case of steady streaks. The phenomenon was shown to be caused by the nonlinear effects in the base flow. In the presence of unsteady streaks however, the wall-normal profile of the base flow became inflectional, and the growth rate of the inner instability increased rapidly with the frequency and amplitude of the streaks.

— Since the inner mode exists close to the wall, it is expected to be dependent on receptivity mechanisms. The inner mode can be compared to the near wall instabilities found in the simulations of Nagarajan *et al.* (2007) which included a leading edge.

— The outer mode, in contrast, resides closer to the edge of the boundary layer and is driven by the spanwise shear between the streaks. It can be related to the instabilities observed in experiments by Hernon *et al.* (2007) and simulations by Jacobs & Durbin (2001), as well as the second class of instability found by Nagarajan *et al.* (2007).

— The critical streak amplitude for the outer instability was calculated for different frequency streaks, and was approximately 8% of U_∞ for unsteady streaks. Compared to previous stability analyses for steady streaks (Andersson *et al.*, 2001), this value is more closely commensurate to the averaged disturbance levels inside boundary layers at the beginning of transition, from experiments and simulations.

— Direct numerical simulations provided an empirical view of the evolution of the instabilities in a streaky boundary layer. They showed that both the inner and outer mode are capable of growth to nonlinear amplitudes and causing the boundary-layer flow to break down to turbulence.

The growth rates of both the inner and outer instabilities were similar, but each can become the most unstable for certain parameters of the base flow. In general, the base flow became

more unstable as the frequency or the amplitude of the base streaks was increased. From an experimental standpoint, utilising spanwise- and temporally- periodic disturbances to trigger streaks, such as suction and blowing or modulating roughness elements, the frequency and amplitude of the streaks should be maximised to trigger transition sooner. However, if the streaks are generated by free-stream vortical disturbances, their amplitudes is inversely related to the forcing frequency, therefore an optimal range of the base flow frequency emerges for which the inner and outer modes are most unstable. Streaks with higher frequencies do not amplify considerably and are therefore benign; streaks with lower frequencies can reach high amplitudes, but do not introduce sufficient unsteadiness to promote instability. The current results show that streaks, which are triggered by free-stream vortical disturbances, are prone to secondary instability particularly due to their unsteady nature. Steady streaks, both here and in the previous literature (Andersson *et al.*, 2001), are more stable. Despite their higher potential for amplification, these streaks may not play an important role in bypass transition.

Appendix A

Extended stability results with linear streaks

In chapter 4, linear stability results were reported which showed how the growth rate of the inner and outer modes varied with streak frequency. The data was reported in two ways: with a constant streak amplitude, A_u, or with a constant forcing amplitude A_v. The second approach is used in this appendix, in the context of linear streaks. When the amplitude of the forcing is held constant, varying the streak wavenumber affects the linear stability problem in two ways: directly, and by altering the streak amplitude.

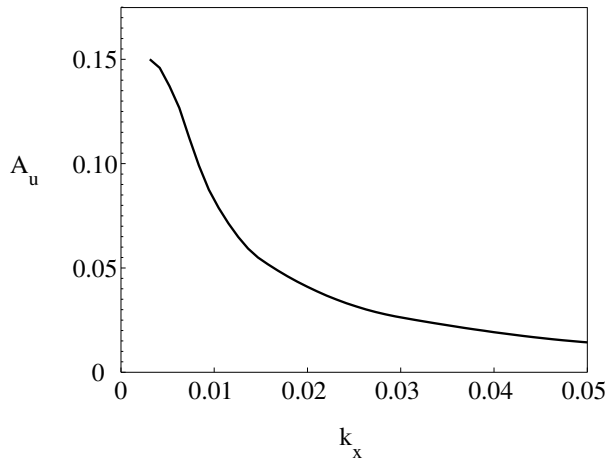

Figure A.1: The dependence of streak amplitude A_u on k_x, when the forcing continuous mode amplitude was held constant, $R = 200$, $k_y = k_z = 0.6379$.

Figure A.1 shows the effect of k_x on streak amplitude, A_u, whilst holding the forcing amplitude constant. The results were calculated with the linear streak formulation, described in section 2.2.1, and the amplitude of the streaks was normalised to be 15% at $k_x = 0.0031$. The parameters of the streak match those used in chapter 2, and the results also resemble those for nonlinear streaks, presented in figure 4.5(a).

Having established the influence of k_x on the amplification of linear streaks, it was possible to investigate the combined effects of k_x on the secondary instabilities. The growth rate of the inner and outer mode were recalculated by solving equations 2.28, for different values of k_x, and using the streak amplitudes shown in figure A.1. The effect of increasing the wavenumber of the continuous-mode forcing is to reduce the growth rate of both the inner and outer modes, as shown in figures A.2 and A.3. Despite the fact that, at a constant streak-amplitude, streaks with a higher wavenumber are more unstable, the shear sheltering effect dominates and reduces the growth rate by decreasing the streak amplitude. This is in line with the results in chapter 4 where the effect of frequency was also investigated at a constant forcing amplitude, though in that case the streaks were nonlinear.

Like the rest of the results for linear streaks, the data here does not include steady streaks with $k_x = 0$, rather the lowest value of k_x is 0.0031. As such, they do not exhibit the low growth rate observed in the data for nonlinear streaks around $F = 0$, in figures 4.5(b) and 4.16(b). However, in both figures A.2 and A.3 the growth rate as a function of k_x has a negative curvature and tends to level off for the lowest k_x.

The present results for unsteady streaks also shed light on the findings of Jonáš *et al.* (2000). They conducted experiments on bypass transition and varied the length scale of the free-stream turbulence by using different grids. They asserted that, at a fixed turbulent intensity, increasing the length scale of the turbulent disturbances lead to transition further

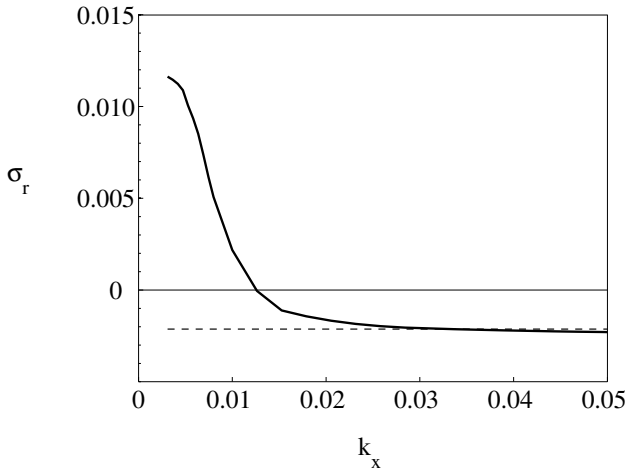

Figure A.2: Growth rate of the inner mode, σ_r versus the streak wavenumber, k_x with a constant amplitude continuous mode. The growth rate of the TS wave for the Blasius boundary layer is marked by the dashed line. Base-flow parameters: $R = 200$, $k_y = k_z = 0.6379$.

upstream. This could be explained in the same way as the present results: low-wavenumber disturbances in the free stream have a higher propensity than high-wavenumber perturbations to enter the shear region and generate streaks leading to secondary instability.

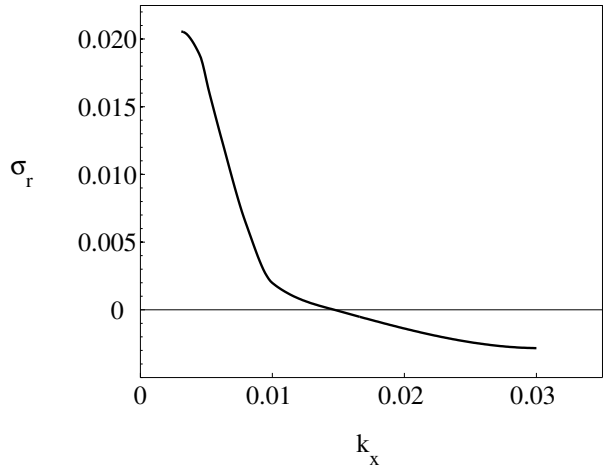

Figure A.3: Growth rate of the outer mode, σ_r versus the streak wavenumber, k_x with a constant amplitude continuous mode. Base-flow parameters: $R = 200$, $k_y = k_z = 0.6379$.

Bibliography

Abu-Ghannam, B. & Shaw, R. 1980 Natural transition of boundary layers-the effects of turbulence, pressure gradient, and flow history. *J. Mech. Eng. Sci.* **22**, 213–228.

Andersson, P., Berggren, M. & Henningson, D. S. 1999 Optimal disturbances and bypass transition in boundary layers. *Phys. Fluids* **11**, 134–150.

Andersson, P., Brandt, L., Bottaro, A. & Henningson, D. S. 2001 On the breakdown of boundary layer streaks. *J. Fluid Mech.* **428**, 29–60.

Arnal, D. & Juillen, J. C. 1978 Contribution experimentalealé de la receptivite d'une couche limite laminaire, a la turbulence de l'ecoulement general. *Technical report, ONERA Rap. Tech.* 1/5018 AYD.

Asai, M., Minagawa, M. & Nishioka, M. 2002 The instability and breakdown of a near-wall low-speed streak. *J. Fluid Mech.* **455**, 289–314.

Bakchinov, A. A., Grek, G. R., Klingmann, B. G. B. & Kozlov, V. V. 1995 Transition experiments in a boundary layer with embedded streamwise vortices. *Phys. Fluids* **7**, 820–832.

Bertolotti, F. 1997 Response of the Blasius boundary layer to free-stream vorticity. *Phys. Fluids* **9**, 2286–2299.

Blennerhassett, P. & Bassom, A. 2006 The linear stability of high-frequency oscillatory flow in a channel. *J. Fluid Mech.* **556**, 1–25.

Boiko, A. V., Westin, K. J. A., Klingmann, B. G. B., Kozlov, V. V. & Alfredsson, P. H. 1994 Experiments in a boundary layer subjected to free stream turbulence. Part 2. The role of TS-waves in the transition process. *J. Fluid Mech.* **281**, 219–245.

Brandt, L. & de Lange, H. C. 2008 Streak interactions and breakdown in boundary layer flows. *Phys. Fluids* **20**, 024107.

Brandt, L., Schlatter, P. & Henningson, D. S. 2004 Transition in boundary layers subject to free-stream turbulence. *J. Fluid Mech.* **517**, 167–198.

Butler, K. M. & Farrell, B. F. 1992 Three-dimensional optimal perturbations in viscous shear flow. *Phys. Fluids* **4**, 1637–1650.

Cossu, C. & Brandt, L. 2002 Stabilization of Tollmien-Schlichting waves by finite amplitude optimal streaks in the Blasius boundary layer. *Phys. fluids* **14**, 57–60.

Cossu, C. & Brandt, L. 2004 On Tollmien-Schlichting-like waves in streaky boundary layers. *Eur. J. Mech. - B/Fluids* **23**, 815–833.

Cossu, C., Pujals, G. & Depardon, S. 2008 Optimal transient growth and very large–scale structures in turbulent boundary layers. *J. Fluid Mech.* **619**, 79–94.

Craik, A. 1971 Non-linear resonant instability in boundary layers. *J. Fluid Mech* **50**, 393–413.

Durbin, P. & Wu, X. 2006 Transition beneath vortical disturbances. *Annu. Rev. Fluid Mech.* **30**, 107–128.

Durst, F. & Ünsal, B. 2006 Forced laminar-to-turbulent transition of pipe flows. *J. Fluid Mech.* **560**, 449–464.

Emmons, H. 1951 The laminar-turbulent transition in a boundary layer. Part 1. 1951. *J. Aeronaut. Sci* **18**, 490–498.

Gaster, M. 1962 A note on the relation between temporally-increasing and spatially-increasing disturbances in hydrodynamic stability. *J. Fluid Mech.* **14**, 222–224.

Gaster, M. 1974 On the effects of boundary-layer growth on flow stability. *J. Fluid Mech.* **66**, 465–480.

Goldstein, M., Leib, S. & Cowley, S. 1992 Distortion of a flat-plate boundary layer by free-stream vorticity normal to the plate. *J. Fluid Mech.* **237**, 231–260.

Goldstein, M. & Sescu, A. 2008 Boundary-layer transition at high free-stream disturbance levels–beyond Klebanoff modes. *J. Fluid Mech.* **613**, 95–124.

Grek, G., Kozlov, V. & Ramazanov, M. 1990 Investigation of boundary layer stability in a gradient flow with a high degree of free-stream turbulence. *Fluid Dyn.* **25** (2), 207–213.

Grosch, C. & Salwen, H. 1968 The stability of steady and time-dependent plane Poiseuille flow. *J. Fluid Mech.* **34**, 177–205.

Grosch, C. & Salwen, H. 1978 The continuous spectrum of the Orr-Sommerfeld equation. I- The spectrum and the eigenfunctions (shear flow stability calculations). *J. Fluid Mech.* **87**, 33–54.

Herbert, T. 1983 Secondary instability of plane channel flow to subharmonic three-dimensional disturbances. *Phys. Fluids* **26**, 871–874.

Herbert, T. 1988 Secondary instability of boundary layers. *Ann. Rev. Fluid Mech.* **20**, 487–526.

Herbert, T. 1997 Parabolized stability equations. *Ann. Rev. Fluid Mech.* **29**, 245–283.

Herbert, T. & Morkovin, M. 1980 Dialogue on bridging some gaps in stability and transition research. In *Laminar-turbulent transition; Proceedings of the Symposium, Stuttgart, West Germany, September 16-22, 1979.*, pp. 47–72.

Hernon, D., Walsh, E. J. & McEligot, D. M. 2007 Experimental investigation into the routes to bypass transition and the shear-sheltering phenomenon. *J. Fluid Mech.* **591**, 461–479.

Hunt, J. C. R. & Carruthers, D. J. 1990 Rapid distortion theory and the of turbulence. *J. Fluid Mech.* **212**, 497–532.

Hunt, J. C. R. & Durbin, P. A. 1999 Perturbed vortical layers and shear sheltering. *Fluid Dyn. Res* **24**, 375–404.

Jacobs, R. & Durbin, P. 1998 Shear sheltering and the continuous spectrum of the Orr–Sommerfeld equation. *Phys. Fluids* **10**, 2006–2011.

Jacobs, R. G. & Durbin, P. A. 2001 Simulations of bypass transition. *J. Fluid Mech.* **428**, 185–212.

Jonáš, P., Mazur, O. & Uruba, V. 2000 On the receptivity of the by-pass transition to the length scale of the outer stream turbulence. *Eur. J. Mech. B/Fluids* **19**, 707–722.

Kachanov, Y. S. 1994 Physical mechanisms of laminar-boundary-layer transition. *Ann. Rev. Fluid Mech.* **26**, 411–482.

KENDALL, J. 1985 Experimental study of disturbances produced in a pre-transitional laminar boundary layer by weak freestream turbulence. In *American Institute of Aeronautics and Astronautics, Fluid Dynamics and Plasmadynamics and Lasers Conference, 18th, Cincinnati, OH, July 16-18, 1985*.

KENDALL, J. M. 1990 Boundary layer receptivity to free stream turbulence. *AIAA Paper* **90**, 1504.

KENDALL, J. M. 1991 Studies on laminar boundary-layer receptivity to freestream turbulence near a leading edge. In *Boundary layer stability and transition to turbulence* (ed. D. C. Reda, H. L. Reed & R. Kobayashi), *ASME FED*, vol. 114, pp. 23–30.

KENDALL, J. M. 1998 Experiments on boundary-layer receptivity to freestream turbulence. *AIAA Paper* **98**, 0530.

KERCZEK, C. & DAVIS, S. 2006 Linear stability theory of oscillatory Stokes layers. *J. Fluid Mech.* **62**, 753–773.

KLEBANOFF, P. S. 1971 Effect of freestream turbulence on the laminar boundary layer. *Bull. Am. Phys. Soc* **10**, 1323.

KLEBANOFF, P. S., TIDSTROM, K. D. & SARGENT, L. M. 1962 The three-dimensional nature of boundary-layer instability. *J. Fluid Mech.* **12**, 1–34.

KLEISER, L. & ZANG, T. A. 1991 Numerical Simulation of Transition in Wall-Bounded Shear Flows. *Ann. Rev. Fluid Mech.* **23**, 495–537.

KNAPP, C. F. & ROACHE, P. J. 1968 A combined visual and hot-wire anemometer investigation of boundary-layer transition. *AIAA Paper* **6**, 29–36.

Kosorygin, V. S., R. R. H. & Saric, W. S. 1995 Laminar boundary-layer, sound receptivity and control. *Laminar-turbulent transition* pp. 517–524.

Kozlov, L. & Babenko, V. 1978 Experimental Studies of the Boundary Layer. *[In Russian] Kiev: Naukova DumkaPub* .

Lehoucq, R., Sorensen, D. & Yang, C. 1998 *ARPACK users' guide*. SIAM Philadelphia.

Leib, S., Wundrow, D. & Goldstein, M. 1999 Effect of free-stream turbulence and other vortical disturbances on a laminar boundary layer. *J. Fluid Mech.* **380**, 169–203.

Lin, C. 1955 *The Theory of Hydrodynamic Stability*. Cambridge Univ. Press.

Liu, Y., Zaki, T. A. & Durbin, P. A. 2008*a* Boundary-layer transition by interaction of discrete and continuous modes. *J. Fluid Mech.* **604**, 199–233.

Liu, Y., Zaki, T. A. & Durbin, P. A. 2008*b* Floquet analysis of secondary instability of boundary layers distorted by Klebanoff streaks and Tollmien–Schlichting waves. *Phys. Fluids* **20**, 124102.

Luchini, P. 2000 Reynolds-number-independent instability of the boundary layer over a flat surface: optimal perturbations. *J. Fluid Mech.* **404**, 289–309.

Luo, J. & Wu, X. 2010 On the linear instability of a finite Stokes layer: Instantaneous versus Floquet modes. *Phys. Fluids* **22**, 054106.

Mack, L. 1977 Transition prediction and linear stability theory. In *AGARD Conference proceedings, NATO, Paris (unpublished)*.

Mandal, A. C., Venkatakrishnan, L. & DEY, J. 2010 A study of boundary layer transition induced by freestream turbulence. *J. Fluid Mech.* (In Press).

Mans, J., Kadijk, E. C., Lange, H. C. & Steenhoven, A. A. 2005 Breakdown in a boundary layer exposed to free-stream turbulence. *Exp. Fluids* **39**, 1071–1083.

Mans, J., de Lange, H. C. & van Steenhoven, A. A. 2007 Sinuous breakdown in a flat plate boundary layer exposed to free-stream turbulence. *Phys. Fluids* **19**, 088101.

Maseev, L. 1968 Secondary instability of boundary layers. *[In Russian] Tr. Mosk. Inst. Inzh. Zheleznodorozhn Transp.* (222).

Matsubara, M. & Alfredsson, P. 2001 Disturbance growth in boundary layers subjected to free-stream turbulence. *J. Fluid Mech.* **430**, 149–168.

Moffatt, H. 1967 The interaction of turbulence with strong wind shear. *Proc. URSI–IUGG Colloq. on Atoms. Turbulence and Radio Wave Propag., Nauka, Moscow* pp. 139–154.

Morkovin, M. V. 1969 On the many faces of transition. *Viscous Drag Reduction* pp. 1–31.

Nagarajan, S., Lele, S. K. & Ferziger, J. H. 2007 Leading-edge effects in bypass transition. *J. Fluid Mech.* **572**, 471–504.

Orr, W. 1907 The stability or instability of steady motions of a liquid. Part II: A viscous liquid. In *Proc. Royal Irish Acad.*, , vol. 27, pp. 69–138.

Orszag, S. & Patera, A. 1983 Secondary instability of wall-bounded shear flows. *J. Fluid Mech.* **128**, 347–385.

Ovchinnikov, V., Choudhari, M. & Piomelli, U. 2008 Numerical simulations of boundary-layer bypass transition due to high-amplitude free-stream turbulence. *J. Fluid Mech.* **613**, 135–169.

Phillips, O. M. 1969 Shear-flow turbulence. *Ann. Rev. Fluid Mech.* **1**, 245–264.

Rayleigh, L. 1879 On the stability, or instability, of certain fluid motions. *Proceedings of the London Mathematical Society* **1**, 57.

Roach, P. & Brierley, D. 1992 The Influence of a Turbulent Free-Stream on Zero Pressure Gradient Transitional Boundary Layer Development Part I: Test Cases T3A and T3B. In *Numerical simulation of unsteady flows and transition to turbulence: proceedings of the ERCOFTAC Workshop held at EPFL, 26-28 March 1990, Lausanne, Switzerland*, pp. 319–347. Cambridge Univ. Press.

Rosenfeld, M., Kwak, D. & Vinokur, M. 1991 A fractional step solution method for the unsteady incompressible Navier-Stokes equations in generalized coordinate systems. *J. Comput. Phys.* **94**, 102–137.

Ross, J., Barnes, F., Burns, J. & Ross, M. 1970 The flat plate boundary layer. Part 3. Comparison of theory with experiment. *J. Fluid Mech.* **43**, 819–832.

Salwen, H. & Grosch, C. 1981 The continuous spectrum of the Orr-Sommerfeld equation. Part 2. Eigenfunction expansions. *J. Fluid Mech.* **104**, 445–465.

Saric, W. 1998 Influence of high-amplitude noise on boundary-layer transition to turbulence. *NASA Report* (19990025274).

Saric, W., Reed, H. & Kerschen, E. 2002 Boundary-layer receptivity to freestream disturbances. *Ann. Rev. Fluid Mech.* **34**, 291–319.

Saric, W. S. 1994 Gortler vortices. *Ann. Rev. Fluid Mech.* **26**, 379–409.

Saric, W. S., White, E. B. & Reed, H. L. 1999 Boundary-layer receptivity to freestream disturbances and its role in transition. In *AIAA Fluid Dynamics Conference, 30 th, Norfolk, VA; United States*.

Schubauer, G. & Skramstad, H. 1947 Laminar boundary-layer oscillations and transition on a flat plate. *Journal. Res. Nat. Bur. Standards* **38**, 251–292.

Sommerfeld, A. 1908 Ein Beitrag zur Hydrodynamischen Erklärung der Turbulenten Flüssigkeitsbewegungen. *Proceedings 4th international congress of mathematicians, Rome* **3**, 116–124.

Strazisar, A., Reshotko, E. & Prahl, J. 1977 Experimental study of the stability of heated laminar boundary layers in water. *J. Fluid Mech.* **83**, 225–247.

Suder, K., Obrien, J. & Reshotko, E. 1988 Experimental study of bypass transition in a boundary layer. *NASA Report* (100913).

Swearingen, J. D. & Blackwelder, R. F. 1987 The growth and breakdown of streamwise vortices in the presence of a wall. *J. Fluid Mech.* **182**, 255–290.

Taylor, G. 1936 Effect of turbulence on boundary layers. *Collected Papers of GI Taylor (ed. G. Batchelor)* .

Tollmien, W. 1929 Über die Entstehung der Turbulenz. *Nachr. Ges. Wiss. Göttingen* pp. 21–44.

Trefethen, L., Trefethen, A., Reddy, S. & Driscoll, T. 1993 Hydrodynamic stability without eigenvalues. *Science* **261** (5121), 578–584.

Westin, K. J. A., Boiko, A. V., Klingmann, B. G. B., Kozlov, V. V. & Alfredsson, P. H. 1994 Experiments in a boundary layer subjected to free stream turbulence. Part 1. Boundary layer structure and receptivity. *J. Fluid Mech.* **281**, 193–218.

Wu, X. & Choudhari, M. 2003 Linear and nonlinear instabilities of a Blasius boundary layer perturbed by streamwise vortices. Part 2. Intermittent instability induced by long-wavelength Klebanoff modes. *J. Fluid Mech.* **483**, 249–286.

Zaki, T. A. & Durbin, P. A. 2005 Mode interaction and the bypass route to transition. *J. Fluid Mech.* **531**, 85–111.

Zaki, T. A. & Durbin, P. A. 2006 Continuous mode transition and the effects of pressure gradient. *J. Fluid Mech.* **563**, 357–388.

Zaki, T. A., Liu, Y. & Durbin, P. A. 2010 Boundary layer transition by interaction of streaks and Tollmien–Schlichting waves. In *Seventh IUTAM Symposium on Laminar-Turbulent Transition*, pp. 439–444. Springer.

Zaki, T. A. & Saha, S. 2009 On shear sheltering and the structure of vortical modes in single- and two-fluid boundary layers. *J. Fluid Mech.* **626**, 111–147.